Temperature Dependent Operation of Vertical Cavity Surface Emitting Lasers (VCSELs)

by

C. J. Hepburn

A thesis submitted for the degree of Master of Science (by Dissertation) in Physics.

University of Essex, October, 2001.

Acknowledgements

I would like to express my gratitude to my supervisor Dr. Naci Balkan, for his advice and contribution throughout the duration of my MSD. I would also like to thank Mr. Russell Sceats for his helpful advice on the experimental set-up and Mr. Adrian Boland-Thoms for aiding the smooth running of the experiments by providing the invaluable benefit of his many years of experience and technical expertise with semiconductor devices and fabrication. Many thanks also to the growers at DERA, (Philippa Parmiter) , Sheffield (Jon Woodhead) and BT (Paul Cannard) as well as everyone else that contributed to produce this work, namely, Desi Ramoo, Prof. Mike Adams. Finally, I extend my thanks to the members of the Optoelectronics Research group who helped in keeping up my morale when things were not always running smoothly.

1. Introduction

Vertical Cavity Surface-Emitting Lasers (VCSELs) are semiconductor lasers with a short cavity length, and laser emission perpendicular to the top or bottom surface. Modern VCSELs frequently have top and bottom mirrors formed by periodic layers of semiconductor material with contrasting refractive indices, to enhance the quality of the cavity.

The earliest VCSEL was reported in 1965 by Melngailis [1,2]. It consisted of a n^+pp^+ junction of InSb. When cooled to 10 K and subjected to a magnetic field to confine the carriers, the device emitted coherent radiation at a wavelength of around 5.2 μm. Later, other groups reported on the grating surface emission[3,4] Near infra-red emission close to telecommunications wavelengths of 1.5 μm was achieved by Iga, Soda, *et al.* in 1979 [5] at the Tokyo Institute of Technology. These early VCSEL devices had metallic mirrors with resulting high threshold current densities (44 $kAcm^{-2}$) and were cooled using liquid Nitrogen. Epitaxial mirrors for GaAs/AlGaAs VCSELs were pioneered in 1983[6], with the pulsed room temperatures VCSELs being produced in the laboratory one year later[7]. Reduction in the threshold current density was connected with reduction in the active volume of the cavity. Today, GaAs/AlGaAs VCSELs with oxide apertures for enhanced current confinement have threshold currents as low as 40 μA.[8]

Despite the early fabrication of VCSELs, research concentrated on Fabry-Perot lasers until techniques for growing distributed Bragg reflectors became established. Even with the difficulties associated with the growth of the reflectors required for efficient VCSELs

there are many advantages over Fabry-Perot lasers which have ensured that VCSELs have become an important laser technology. Most important, is the small volume of the active region. This is a feature that is inherent in the geometry of VCSELs and by scaling down the size of the device lower threshold currents can be achieved. Cavity designs that have improved the performance of Fabry-Perot cavity lasers, such as quantum wells, multi-quantum wells and strained quantum well active regions can be adapted for use in VCSELs. In the transverse directions, current confinement limits ultimately the active volume and can be implemented in the form of oxide apertures [9, 10, 11], ion implanted regions [12] or current blocking layers. [13, 14, 15]

A resonance or mode occurs within the cavity when the light has nodes at both ends of the cavity. In longitudinal cavity lasers, the wavelength of light is much smaller than the length of the cavity, therefore many lasing modes are supported with in the cavity. At threshold, the dominant laser mode will be one of a number of possible closely space-frequencies and this dominant mode is susceptible to 'mode hopping'. In VCSELs however, typical cavity lengths are between 1-3 wavelengths of the output wavelength. Therefore a single longitudinal lasing mode can be achieved. The relatively extended lateral dimensions of VCSELs can lead to higher order transverse modes being excited at power levels greater than 1 mW. However, this can be suppressed by reducing the lateral dimensions of the device.

The application of lasers in the telecommunications industry, for transmitting signals along optical fibres, requires efficient coupling of the light into a fibre. Fabry-Perot lasers, have a thin active region, 1 μm in the transverse dimension with a lateral dimension of around 10 μm. Furthermore, the near field emission is diffracted as it leaves

the cavity and diverges rapidly, producing an astigmatic beam that is difficult to couple efficiently into fibres without expensive optical engineering. The emission produced by a VCSEL can be tailored easily to emit light in a circular based cone with more of the light being launched into the fibre. A considerable part of the cost in the production of Fabry-Perot lasers comes from the fabrication and connection of faulty devices. This stems from the difficulty in testing edge-emitting lasers while still on the semiconductor wafer, since the mirrored facets that create the cavity are not formed until the device has been cleaved from the wafer; typically a labour intensive and hence expensive process. In contrast, VCSELs can be probed and tested before being mounted and packaged.

Surface emission allows for individually addressable arrays of VCSELs to be fabricated, which may find applications as parallel optical interconnects [16], laser printing or multi-frequency arrays of VCSELs[17] with each device emitting light at a different wavelength. The temperature dependence of VCSELs has been an important issue in their development. Unlike Fabry-Perot lasers, the reflectors are strongly wavelength dependent, leading to a sharp cavity resonance at the designed emission wavelength. Joule heating and poor dissipation of heat increase the temperature of the device. With increasing temperature, the cavity resonance and the gain spectrum, shift to longer wavelengths at different rates, resulting in an increase in the threshold current and a roll-off in emitted power. The experiments within this dissertation, aim to show the relationship between the mechanisms governing the temperature dependence of the cavity and the active region of VCSELs. We examine two material systems, GaAs and InGaAsP VCSELs, using computer modelling of theoretical ideas in an attempt to explain the nature of the temperature dependence. The dissertation concludes with a brief review of

the methods employed to reduce the effect of the temperature dependence on the operation of VCSELs.

2. Background

2.1 Radiative Recombination

In this chapter we look at the fundamental physics involved in the operation of lasers, starting with radiative recombination and Einstein equations then non-radiative recombination. Semiconductor lasers are introduced with the p-n junction before explaining double-heterostructure lasers, mode structure and semiconductor material systems. Having established the basis of edge-emission laser diodes, VCSELs are introduced and compared with edge-emission laser diodes.

Essentially, semiconductor laser diodes operate by recombination of non-equilibrium electron-hole pairs injected across a heavily doped p-n junction. The radiation interacts with other electrons in higher excited energy states by the process of stimulated emission. This radiation is amplified by mirrors within a resonant cavity. Stimulated emission is coherent, intense and has a narrow linewidth.

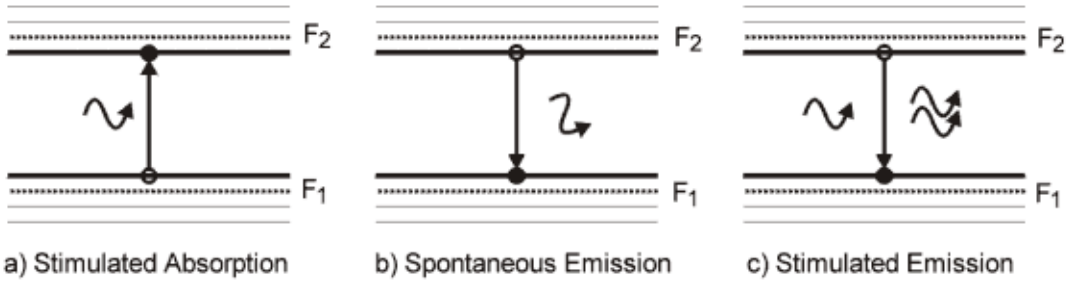

Figure 1. The optical processes of stimulated absorption, spontaneous emission and stimulated emission within a semiconductor material. F_1 and F_2 represent the quasi-Fermi level energies.

In 1916 [18], Einstein, envisaged the statistical process by which lasers operate, when he deduced the relative rates of the optical transitions. His analysis concentrated on atoms at two separate energy levels within a two level system, but the principle can be extended to electrons in the conduction-band and valence-band of a semiconductor. Electrons can interact with light in three ways. An electron can absorb a photon gaining enough energy to join the conduction band. The rate of absorption depends on the probability of electrons in the valence band at level 1, (f_1), the probability of vacancies for electrons in the conduction band at level 2, (1-f_2) and the photon density $\rho(\hbar\omega)$ at the energy $\hbar\omega$. All of these factors are multiplied by the stimulated absorption coefficient B_{12}. In mathematical terms,

$$r_{12} = B_{12} f_1 (1 - f_2) \rho(\hbar\omega) \quad \textbf{(1)}$$

When an electron is in the conduction band, it can simply fall back to the valence band, emitting a photon in the process. The rate at which this occurs is proportional to the number of electrons in the conduction band, the number of unoccupied states in the valence band and the spontaneous emission probability coefficient A_{21}. This process does not depend on the photon density and hence has the name spontaneous emission.

$$r_{21} = f_2 (1 - f_1) A_{21} \quad \textbf{(2)}$$

Alternatively, the electron in the conduction band can interact with a photon, returning it to the valence band, emitting a second photon with the same energy as the initial photon, in a process known as stimulated emission. The rate at which this will occur, is given by

the probability of electrons in the conduction band at level 2, (f_2), the probability of unoccupied states in the valence band at level 1, (1-f_1) and the photon density multiplied by the stimulated emission probability B_{21}.

$$r_{21(stim)} = B_{21} f_2 (1 - f_1) \rho(\hbar\omega) \quad \textbf{(3)}$$

In equations (1) to (3), the probabilities f_1 and f_2 are described by the Fermi-Dirac distribution functions (4), where j is a dummy variable, either 1 or 2 depending on whether the Fermi probability is for the valence band or conduction band respectively.

$$f_j = \left\{ \exp\left[(E_j - F_j) / kT \right] + 1 \right\}^{-1} \qquad j = 1,2 \quad \textbf{(4)}$$

It is this last mechanism that is responsible for laser emission. In thermal equilibrium, the number of electrons being promoted from the valence band to the conduction band, by the principle of detailed balance, is equal to the number falling from the conduction band to the valence band. Therefore,

$$r_{12} = r_{21} + r_{21(stim)} \quad \textbf{(5)}$$

Substituting equations (1), (2) and (3) into (5) and making $\rho(\hbar\omega)$ the subject.

$$\rho(\hbar\omega) = \frac{A_{21}}{B_{12} \dfrac{f_1(1 - f_2)}{f_2(1 - f_1)} - B_{21}} \quad \textbf{(6)}$$

The term $\dfrac{f_1(1 - f_2)}{f_2(1 - f_1)}$ gives the relative occupation probability between the conduction and valence bands and can be replaced by the Boltzmann equation.

The blackbody radiation which gives the equilibrium spectral emission per unit energy.

$$\rho(\hbar\omega) = \frac{\hbar\omega^3}{\pi^2 c^2 \left(\exp\left(\hbar\omega / k_B T\right) - 1\right)} \quad \textbf{(7)}$$

Equating (6) and (7) noting that E_2-E_1=E_{21} gives

$$\frac{\hbar\omega^3}{\pi^2 c^2 \left(\exp\left(\hbar\omega / k_B T\right) - 1\right)} = \frac{A_{21}}{B_{12} \exp\left(E_{21} / kT\right) - B_{21}} \quad \textbf{(8)}$$

Multiplying out equation (8) into temperature dependent and temperature independent terms, we can deduce that B_{12}= B_{21} or the rate of stimulated absorption is equal to the rate stimulated emission and that the ratio of spontaneous emission to stimulated emission is $\frac{\hbar\omega^3}{\pi^2 c^2}$. If we know any one of the coefficients it enables any of the others to be calculated.

2.2 Non-Radiative Recombination

An electron-hole pair can combine without the emission of a photon. The mechanisms by which this may occur are known as non-radiative recombination. The study of non-radiative recombination is inherently difficult, as one is looking for processes that result in the absence of photons. Experimentally, the parameters that can be measured are emission efficiency, carrier lifetime and the kinetics of the recombination process. In lasers, non-radiative recombination results in a loss of excited carriers, making population inversion more difficult to achieve. Some of the mechanisms leading to non-radiative recombination are listed below.

2.2.1 Impurities and Defects

Impurities and inclusions in the crystal structure introduce discrete levels into the energy gap. Interstitial atoms or voids affect the local distribution of the electrons for covalent bonding. The resulting interactions can cause additional discrete energy levels to appear in the energy gap. Electrons can then preferentially, decay to one of these levels before decaying to the ground state non-radiatively. The rate of impurity recombination is written as

$$R_d = A_{nr} n \quad \textbf{(9)}$$

where

$$A_{nr} = \sigma \nu N_t \quad \textbf{(10)}$$

In equation 10, σ is the cross-section of the trap, N_t is the trap density and ν is the velocity of the electrons or holes. A_{nr} is the inverse of the non-radiative lifetime in the presence of a trap.

The defect or impurity recombination follows a linear dependence with carrier density. In the regime of low injection current the defect recombination rate can also be shown to be linearly proportional to the carrier density *n*.

2.2.2 Auger Recombination

In the Auger recombination, the energy released by a recombining electron is immediately absorbed by another electron which then dissipates the energy by emitting phonons. Thus this is a three body collision, involving two electrons and a hole, results in no net phonon emission. There are many different types of Auger recombination

including, i) band-to-band, ii) phonon-assisted Auger processes and iii) trap assisted Auger processes. The three most important types of Auger process for III-V semiconductor materials belong to the first category and are shown in Figure 2. In the CCCH process, two electrons in the conduction band collide. The collision knocks one electron into the valence band while the other gains energy and rises further into the conduction band. The high energy electron loses its excess energy and falls to the bottom of the conduction band releasing its excess energy as phonons. A similar collision process can occur with holes in the heavy hole valence band resulting in one hole be knocked into the Split-Off band (CHHS process) or the Light-Hole band (CHHL process). For quantum well material, additional types can be defined but they still fall into these three general categories.

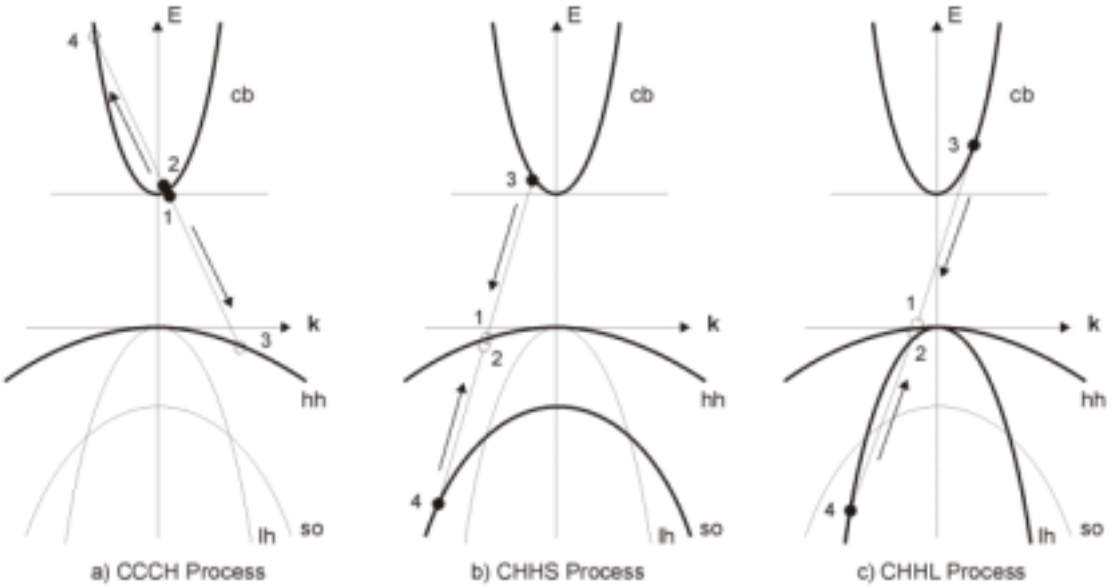

Figure 2. Three Auger recombination processes. In the CCCH process (a), two electrons collide sending one to a higher energy level within the conduction band and the second into the heavy-hole valence band. In the CHHS process (b), two holes collide within the heavy-hole valence band. One hole is filled from the conduction band while the other appears deep within the split-off valence

band. The CHHL process (c) is similar to the CHHS process with the hole appearing deep within the light-hole valence band.

Since Auger recombination relies on collisions, we would expect this loss mechanism to become important as the carrier density increases. In lasers, the injected electron and hole densities are very high and also equal implying that all three Auger processes are potentially important. The Auger process are dependent on the probability of finding the necessary states occupied or empty. For the CCCH, CHHS, CHHL processes [19] respectively, the Fermi factors are: [20]

$$P_{1\to 3} = f_{c1} f_{c2} (1 - f_{v3})(1 - f_{c4}) \quad \textbf{(11)}$$

$$P_{3\to 1} = (1 - f_{v1})(1 - f_{v2}) f_{c3} f_{v4} \quad \textbf{(12)}$$

The subscript on the probability, P, indicates the significant electron recombination path. The additional c and v subscripts on the Fermi functions identify the quasi-Fermi level to be used in each case. For undoped semiconductors, such as in the active region of a laser, the Auger rate at a carrier density n is [21]

$$R = Cn^3 \quad \textbf{(13)}$$

Where C is the Auger coefficient. Typical values for selected materials are shown in Table 1.

Material	**Auger Coefficient 10^{-29} $cm^6 s^{-1}$**
GaAs (bulk)	0.4-0.5 [22]
InGaAsP (1.3 μm bulk)	2-3 [23]
InGaAsP (1.55 μm bulk)	7-9 [24]

Table 1. Auger coefficients for various semiconductors.

The Auger recombination rate is strongly dependent on the bandgap of the material due to energy and momentum conservation. With Auger transitions, as with radiative transitions, the initial energy and momentum of the system must be conserved. This constrains Auger transitions to specific regions of the bands. As the energy gap of the semiconductor decreases, the necessary energy and momentum conditions become satisfied at other locations of the bandstructure and Auger recombination becomes a more likely. Auger recombination is a significant cause of loss for devices operating in the 1.3-1.5 μm region but can be diminished by the use of quantum well structures and the addition of strain to the material.

2.2.3 Surface Recombination

Free bonds in the surface of a semiconductor allow impurities to be absorbed and a high concentration of deep and shallow level impurities can occur. These can act as recombination centres. When electrons are within a diffusion length of the surface , they will recombine and a transition through a continuum of states is readily non-radiative. The rate of recombination is expressed in terms of the surface recombination velocity *S*, surface area *A* and the threshold carrier density n_{th}.

$$R_s = SAn_{th} \quad \textbf{(14)}$$

2.2.4 Intervalence Band Absorption (IVBA)

Intervalence Band Absorption (IVBA) is absorption of electrons in the spin-split off band to the valence band or acceptor level. This mechanism is particularly important at telecommunications wavelengths effecting material such as InGaAsP. IVBA is an

important consideration in devices that have high concentrations of holes such as lasers. IVBA decreases hole population making population inversion more difficult to achieve. and increases with wavelength.[25,26,27] and temperature. Three different IVBA processes are shown in Figure 3.

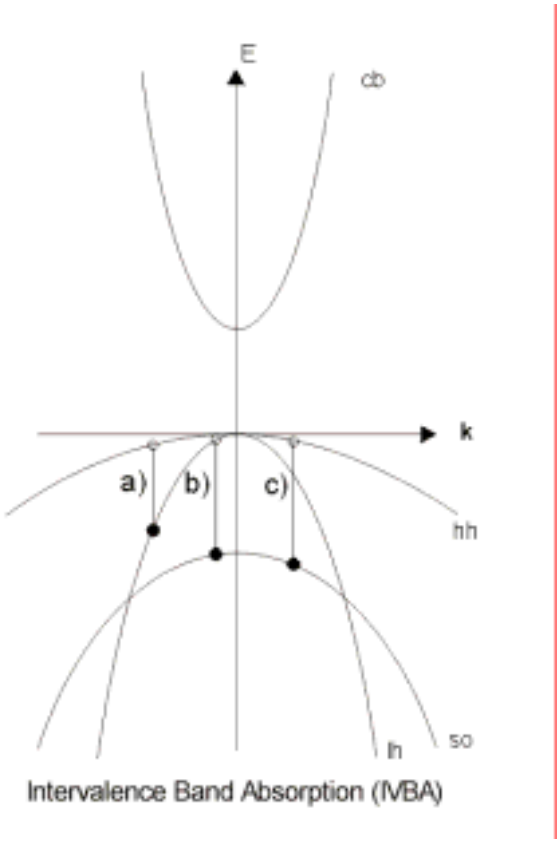

Figure 3. Intervalence band absorption. a). light-hole to heavy-hole band transition, b) spin-orbit band to light-hole band and c) spin-orbit to heavy hole band.

2.3 Fundamentals of Laser Diodes

2.3.1 Material Systems for Semiconductor Lasers

Semiconductor lasers are extremely versatile and are favoured in many applications for their small size, low power requirements and low cost. Today, these lasers have found

their way into the home with the uptake of CD and DVD players and have become the basis of the modern telecommunications industry. Lasers act as transmitters and repeaters in long-haul optical networks. Attenuation losses and dispersion over long distances in optical-fibres require that repeaters are placed at a distance of every 100 km. [28] Maximising the distance between repeaters, the lasers operate at wavelengths close to, or on the minimum, of the dispersion curve for silica. shown in Figure 4.

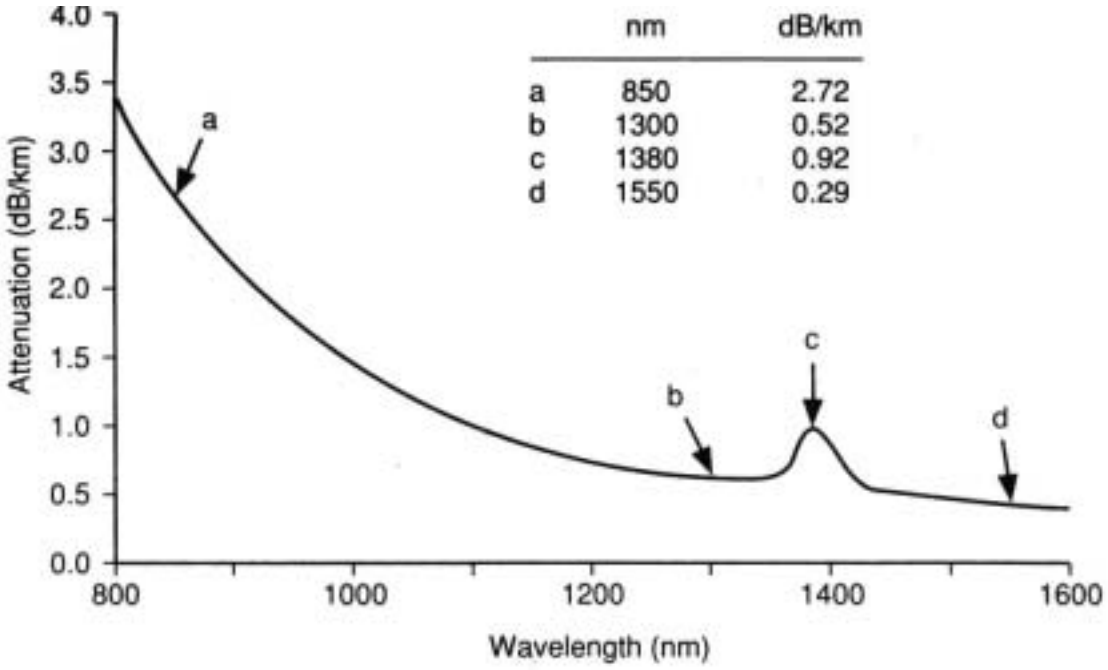

Figure 4. Attenuation of silica fibre with wavelength. The most favourable wavelengths for telecommunications data transmission are 1.3μm and 1.55μm. [29]

The dominant form of loss is from Rayleigh scattering. At wavelengths greater than 1.55 μm, infra-red band-edge absorption increases sharply. Other forms of loss occur from OH^- radicals and Mie [30] scattering. The ideal wavelength for telecommunications applications are 1.3 μm where dispersion is minimised and 1.55 μm, where the attenuation is minimised. It is worth noting that optical fibre processing is improving all

the time and at the time of writing, Corning *Allwave* fibre eliminates the OH^- loss and has an attenuation of 0.15 dB/km.

Table **2** lists some of the material systems used for various applications.

Material	Wavelength	Application
AlGaAs/GaAs	680-870 nm	Solid state lasers pumps, optical data storage. General purposes infra-red source.
InGaAs/GaAs	950-1100 nm	Optical fibre applications. Erbium fibre laser pump.
InGaAsP/InP	1.0-1.7 μm	Optical fibre applications in transmission windows at 1.3μm and 1.55μm
AlGaInP/ GaAs	600-700 nm	Visible applications. Polymer short haul fibres. High temperature operations.
ZnCdSSe	450-550 nm	Potential use in colour displays. Reliability in current devices is poor.
GaN	365 nm	TV Screens, Computer monitors, solid-state lightning, optical reading .
GaInNAs	1.3-1.55 μm	Telecommunications applications.
AlGaInN	200-640 nm	Stimulated emission as short as 402nm has been demonstrated. Has the potential to span the visible and UV spectrum.

Table 2. Semiconductor material systems, wavelength range and possible applications.

2.3.2 p-n Junctions

The p-n junction is crucial part of many semiconductor devices, such as diodes and transistors. The very first semiconductor laser diodes were created from simple p-n junctions in GaAs. Although such devices are now extinct, the p-n junction can be used to illustrate the operation of the most simple form of semiconductor laser. The oldest method of making a p-n junction is by diffusion. The dopant diffuses in under heating, so the surface acceptor concentration exceeds the donor concentration. A junction appears when $N_d=N_a$.

Consider a p-n junction in the absence of an external bias, so that it is in thermodynamic equilibrium. The Fermi-level E_f must be constant across the junction. Since E_f is near the valence band edge in a p-type region and near the conduction band in an n-type region, the bands must bend through the junction as shown below:

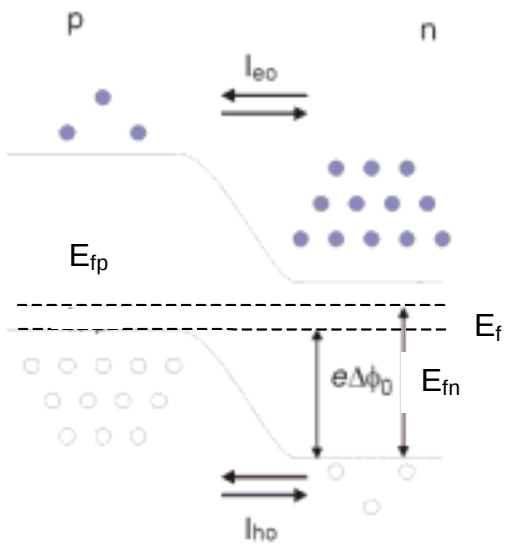

Figure 5. Band-edge diagram of p-n junction at equilibrium. The Fermi level is constant across the junction leading to band bending, to maintain charge neutrality.

In the region where the bands are bending, E_f is near the middle of the gap and therefore $n<n_0$, $p<p_0$, where n_0 and p_0 are the concentrations deep inside the n and p-type regions. This is therefore called the depletion region. If we assume the junction is sharp, with N_a and N_d changing abruptly at the junction, and if we further assume $N_d=N_a$, $p_0=N_a$, thus we see that within the depletion region $p<<N_a$ on the left and $n<<N_d$ and $n_0=N_d$ on the right. Since N_a and N_d are the densities of ionised acceptor and donor ions, this means that there is a net negative charge on the p-type side of the junction, and a net positive charge on the n-type side. These separated charges generate an electric field, which is the physical cause of the band bending. The overall picture is summarised below.

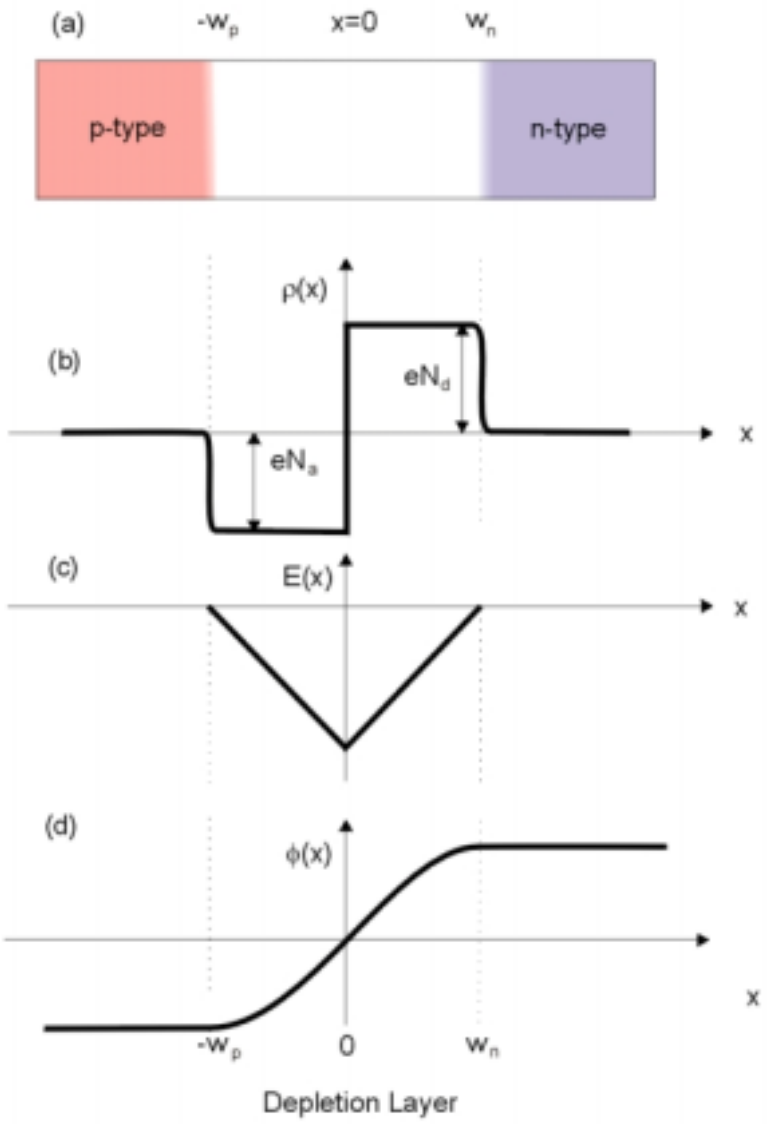

Figure 6. The difference in the Fermi-levels of the p-n material used to form the p-n junction (fig. a), ionisation donor and acceptor atoms leading to a build-up of charge (fig. b) that create an electric field (fig. c) and potential profile (fig. d).

The application of p-n junctions as light-emitters depends on having an applied voltage so that a current flows through the junction. With a voltage V applied in a forward direction, a difference eV appears between the Fermi level values of on the p and n side.

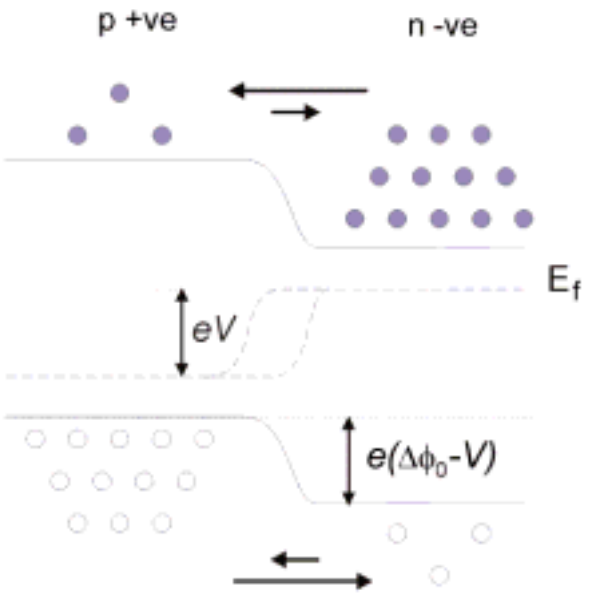

Figure 7. The application of a voltage V creates a difference of *eV* in the Fermi-levels of the p and n-type. The potential difference causes the electrons to flow from the n-type to the p-type and holes to flow from the p-type to the n-type material. If the two regions are heavily doped this can be used to create population in version.

Population inversion can be achieved by using a heavily doped p-n junction. Electrons flow from the n-side to the p-side and holes flow from the p-side to the n-side. The high doping insures that there are plenty of electrons in the conduction band and sufficient unoccupied states in the valence band for strong radiative recombination to occur.

Although the simple p-n junction is fine for the purpose of illustrating how semiconductor lasers operate, they are not at all efficient. There is no well defined region for the carriers to recombine (lack of carrier confinement). Electrons and holes are free to flow through the junction before radiative-recombination occurs. Heterojunctions provide the solution for better confinement of carriers and hence more efficient recombination.

2.4 Double Heterojunctions

As the word suggests, a heterojunction is a junction formed by two different semiconductor materials with different band-gap energies. A notation often used, defines the larger band-gap material type with an uppercase letter and the smaller band-gap material with a lower case n or p. Single heterostructure lasers are slightly more efficient, since they confine some of the carriers and light, however, two heterojunctions or double-heterostructure is more efficient. The example in Figure 8 shows the band edge diagram for a AlGaAs/GaAs, NpP double heterostructure.[31]

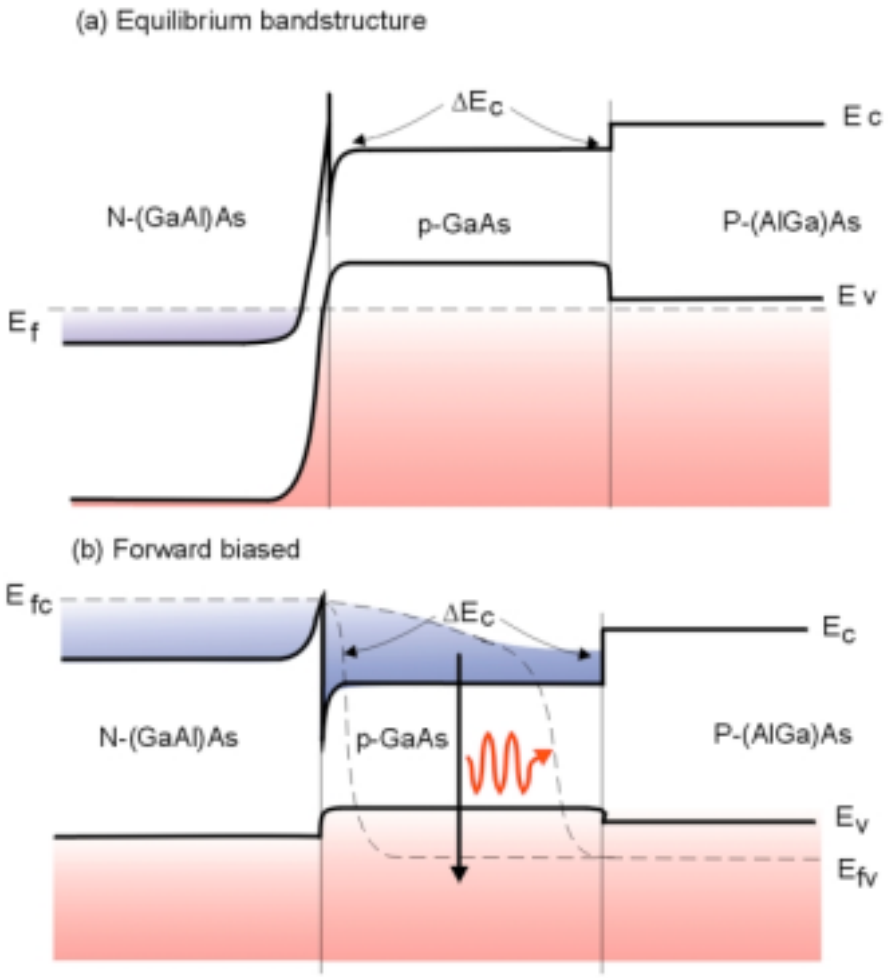

Figure 8. a) Band Structure of a N-p-P GaAs/AlGaAs double heterostructure under equilibrium. b) Forward bias creates a flow of electrons and holes into the p-GaAs region where recombination occurs. [31]

Electrons and holes injected into the active region are prevented from escaping into the cladding layers by potential barriers resulting from the band gap energy offsets. The active region has another unexpected benefit. In the regions where the carrier concentration is high, the refractive index is increased causing the light to be guided along the active region. This is known as gain guiding and occurs in the plane of the semiconductor active region. Various methods are available to confine the current to a

small region of the laser to achieve this effect including, ion implantation and stripe geometry. In the transverse direction, the active region is flanked by semiconductor material with a wider bandgap and lower refractive index that confines the light by index guiding. This method is further refined in the many designs of edge emitter laser by surrounding the active region surrounded by semiconductor material with a lower refractive index semiconductor, such as in the various types of buried heterostructure laser [32,33,34,35,36,37,38] and ridge guide laser. [39,40,41]

2.4.1 Fabry-Perot Lasers

Population inversion alone, is not sufficient to make a laser. There must be a mechanism for interaction between the emitted photons and the electrons in within the active-region. This is achieved by a resonant cavity. Essentially, this is just a box with mirrors to reflect the light back into the cavity.

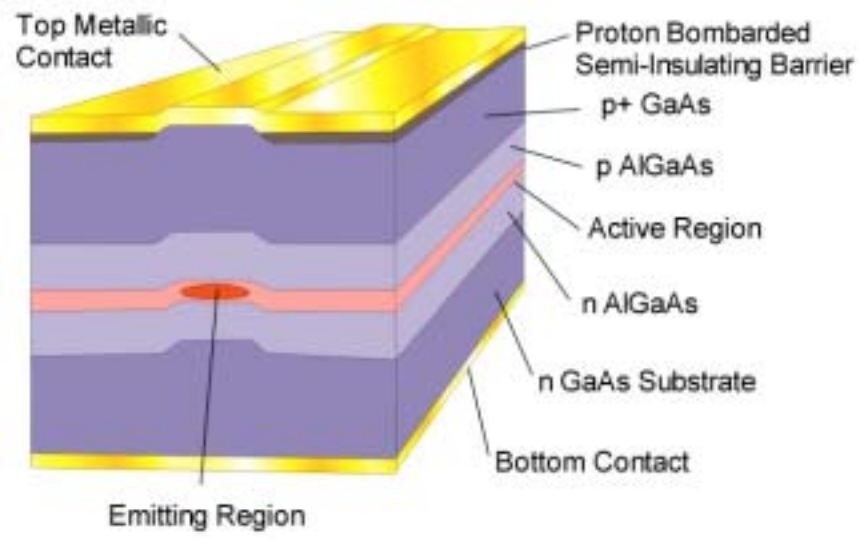

Figure 9. Schematic diagram of a Fabry-Perot laser.

Typical Fabry-Perot cavity dimensions are 200 μm in length, 2-10 μm transverse length and 0.1 μm in lateral width. (Figure 9). The design of the cavity structures for modern heterostructure lasers can be much more complicated incorporating more than one set of cladding layers to confine the carriers (Separate Confinement Heterostructure SCH) or GRaded-INdex Separate Confinement Heterostructures (GRINSCH) . Quantum well and Multiple Quantum Well (MQW) active regions have superseded bulk active-regions because of the advantages that they offer. A quantum well is formed when the width of the active region of the laser becomes comparable with the De-Broglie wavelength, (approx. 100 Å). In this situation, the electron states are no longer quasi-continuous but become separated until only a few states lie within the well. The width of the well determines the number and separation of the energy levels within the well, thus the allowed energy transitions. Radiative recombination in the quantum well is predominantly from the first energy level in the conduction band to the first energy level in the heavy-hole valence band. Therefore, the separation of the energy levels can be tailored by careful design of the well width. Another advantage of quantum well lasers is that the temperature dependence of the intrinsic threshold current (i.e. only including properties that are intrinsic to the gain medium.) is linear with temperature.[42] Well designed quantum well lasers have low threshold currents and are very reliable with estimated lifetimes of greater than 10^6 hours.[48]

The mirrors of the cavity are formed by the cleaving the semiconductor along a {100} plane. The other sides of the laser are rough cut to suppresses transverse modes and add additional protection to the device. The reflectivity of a mirror facet is given by:

$$R = \left| \frac{n_2 - n_1}{n_2 + n_1} \right|^2 \quad \textbf{(15)}$$

Using refractive index values of 1 for air and 3.16 for InP [43] at an energy of 0.8 eV, gives a reflectivity of about 27%.

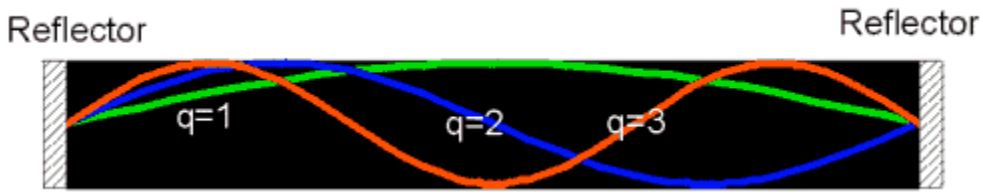

Figure 10. Within the laser cavity, the resonant modes occur when the nodes of the wave are coincident with the ends of the cavity. Therefore, allowed modes occur when *N* half-wavelengths can fit into the cavity.

A resonant mode in the cavity will occur when the nodes of the end of the wave are coincident with the ends cavity. Equivalently, this is expressed as:

$$L = m\lambda / 2n \quad \textbf{(16)}$$

Where L is the length of the cavity, m is an integer, n is the refractive index of the cavity material and λ is the wavelength. The cavity will resonate when the an integer number of half-wavelengths fit into the cavity. For example, a GaAs Fabry-Perot laser with a cavity-length of 200 μm and emission wavelength of 850 nm and refractive index of 3.6 will have 1694 resonant modes. Laser oscillations occur when the round trip gain in the active region equal the total losses. Principle loss mechanisms are scattering from inhomogenuities in the semiconductor, absorption and mirror losses.

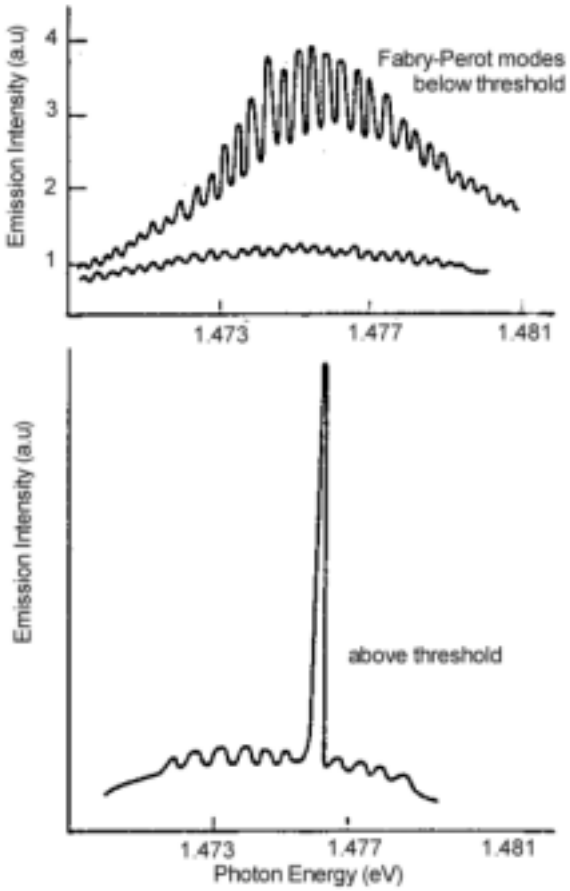

Figure 11. A laser spectrum below threshold (top) and above threshold (below). [44]

Below threshold, all of the resonant modes are superposed on the spontaneous emission spectrum. As the injection current increases, all the modes increase in intensity until threshold is reached. At threshold, the gain equals the loss in device. The intensity of the modes is a random process, but somewhere near the peak of the spontaneous emission one of the emission modes will dominate. A further increase in the injection current causes this mode to lase. The closeness of the lasing modes in frequency means the lasing mode is uncertain and even when established can 'mode-hop'. Such behaviour is not

desirable in lasers used in telecommunications applications where the many closely spaced wavelengths may be used in separate lasers to transmit multiple data streams along a single optical fibre. The DFB laser is one solution. It has a grating etched into the waveguide section of the optical cavity. Below threshold, the pitch of the grating has the effect of enhancing just one of the modes while suppressing the other modes. At threshold, the dominant mode is the mode selected by the grating and this is the mode which will produce laser emission. VCSELs use a wavelength selective cavity but with a different geometry to DFB lasers. The cavity of a VCSEL is typically a half-wavelength, up to 3 wavelengths of the design wavelength. The separation between adjacent modes such that only a single mode is usually present within the emission spectrum.

2.4.2 VCSELs

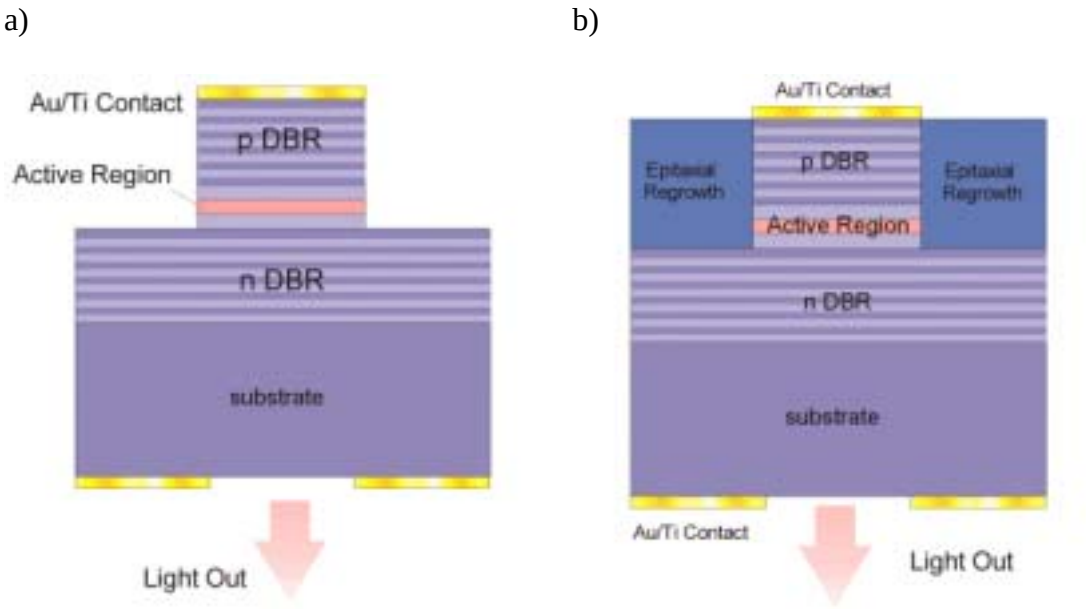

Figure 12. Typical structures of VCSEL lasers. a) shows an air post VCSEL b) is the buried re-growth VCSEL structure.

The principle of operation of a VCSELs is essentially the same as for Fabry-Perot lasers. However, there are some important differences. The cavity is formed in a direction perpendicular to the cavity of Fabry-Perot lasers, with emission from the top or bottom surface of the laser. The short cavity length reduces the number of modes that are permitted within the cavity, allowing for single mode operation but increasing the need to have highly efficient reflective surfaces. Therefore, mirrors, with a reflection coefficient greater than 99%, are necessary to ensure that light reflected back into the cavity many times before being emitted are required. Metallic mirrors, such as gold coatings, have a high absorption coefficient limiting the reflection coefficient to 98-98.5% in the range of wavelengths of 1-1.5 μm. Highly reflective mirrors can be achieved of greater than 99.9% can be achieved, using Distributed Bragg Reflectors (DBRs). These are formed by creating a multi-layered, periodic structure with contrasting layers of material differing in refractive index. At the boundaries of the two materials, the light is partially transmitted and partially reflected. The greater the difference in the refractive index of the two materials, the greater the light reflected back from the boundaries. If several periods are combined, a fraction of the light is reflected back from each interface. For a single layer of semiconductor material and air, about 30% of the light is reflected. If the thickness of the layers is such that the reflected light from the boundaries returns in phase, then by the principle of superposition, the amplitude of the electromagnetic waves is summed. The condition for the waves returning in phase in a single layer is: [45]

$$l = \frac{\lambda}{4n} \qquad \textbf{(17)}$$

Where l is the thickness of the layer, λ is the wavelength of light the layer is designed to reflect and n is the refractive index of the layer. InGaAsP/InP DBRs have at least 45-periods to provide sufficient reflectivity and this is a major drawback in the production of reliable VCSELs operating at long-wavelengths. 100 % reflective mirrors are not possible as the some of the light is inevitably absorbed but 99.7 % reflectivity can be achieved with DBR mirrors.[51]

Dielectric materials, can also be used to create DBRs for VCSELs. These can provide a high contrast ratio and only a few layers may be necessary. By definition, they do not conduct electricity making electrical contact with the active region an issue.

Another important detail in the design of VCSELs, is the placement of the quantum well (or wells) within the cavity. The position of the quantum well controls the longitudinal confinement factor. When the wells are placed at an anti-node of the electromagnetic wave standing wave within the cavity, a factor of two gain in the longitudinal confinement factor can be achieved compared to if the quantum wells were situated at a node of the standing wave. In a MQW cavity, the wells are separated by barrier layers, therefore there is a limit to the number of quantum wells that can effectively be placed within the cavity layer. The number of quantum wells is optimal when the increase in gain length is balanced with the reduction in confinement factor, introduced with increasing number of quantum wells. A comparison of typical GaAs/AlGaAs Fabry-Perot lasers and VCSELs is outlined in Table 3:

Characteristic	Laser Diode	VCSEL
Threshold Current (mA)	25 [47]	3.5 [46]
Threshold Current Density (A/cm^2)	400-800	1100 [46]
Operating Current (mA)	30 [47]	5 [46]
Slope Efficiency (mW/mA)	0.3 [47]	0.25 [47]
Output Power (mW)	1-10	1.5
FWHM	2-3 nm	<5 Å
Beam Divergence	40 ° [47]	12 ° [46]
Temperature Dependence $d\lambda/dT$ (nm/K)	0.3 [47]	0.06 [47]
Astigmatism (μm)	3 [47]	0 [47]
Modulation Bandwidth (GHz)	2 [47]	>10 [47]
Device Size (μm)	50-300 (length)	<5-200 (diameter)
Yield across wafer	Low	~99.8 %
Lifetime (hours)	10^3-10^6	$>10^6$ [48]

Table 3: A comparison of VCSELs and Fabry-Perot lasers.

2.5 Theoretical Background

2.5.1 Transmission Matrix Theory.

The theory for the reflection coefficient is presented from Hecht [49] and generalised to give the reflection coefficient as a function of wavelength. This forms the basis of the program written in *Mathematica* to calculate the reflectivity spectra. The transmission

matrix theory used for calculation of the reflectivity spectra are done at normal incidence, but presented here for light at an arbitrary angle, for completeness.

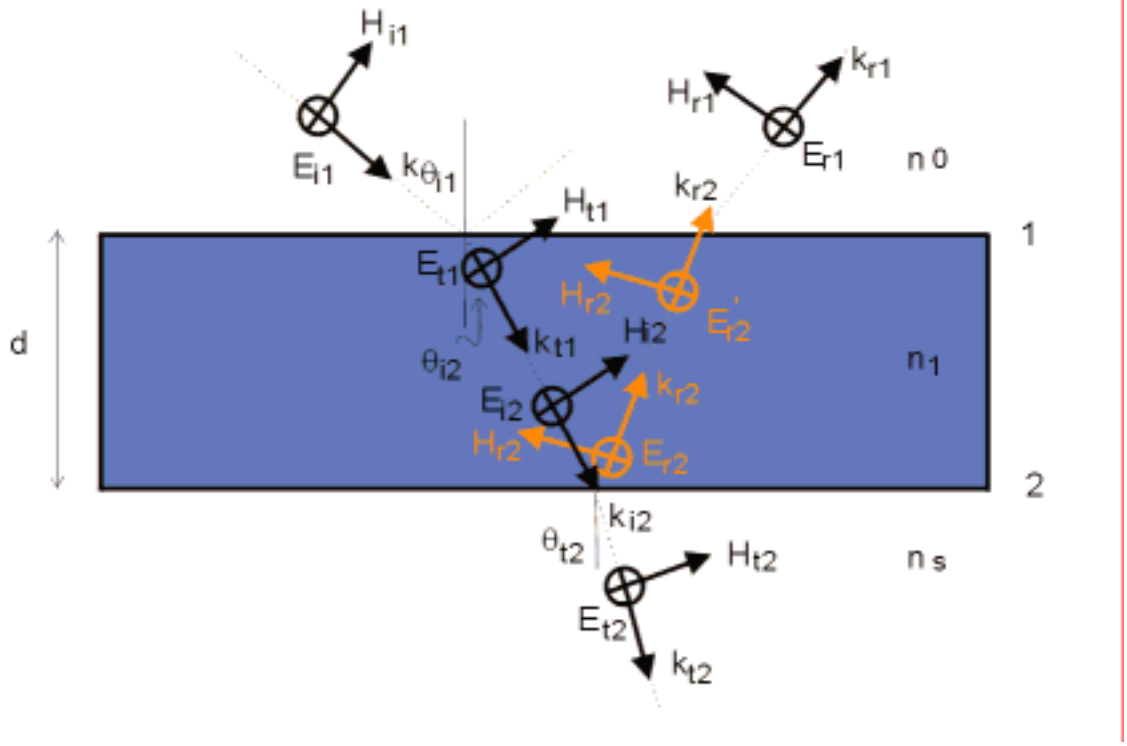

Figure 13 The reflected and transmitted components of light through a single layer of semiconductor material. The first subscript refers to whether wave is incident, reflected or transmitted, while the second either 1 or 2 refers to the upper or lower interface respectively.

E_{r1}, E_{r2},,E_{t2} are the sum of all possible waves travelling in that direction. The boundary conditions require that the tangential components of both the electric and magnetic fields be continuous across the boundaries. At boundary 1 we have:

$$E_1 = E_{i1} + E_{r1}^{'} = E_{t1} + E_{r2}^{'} \qquad \textbf{(18)}$$

The magnetic field intensity can be obtain using the following relationship for a non-magnetic materials.

$$\mathbf{H} = \sqrt{\frac{\varepsilon_0}{\mu_0}} n\hat{\mathbf{k}} \times \mathbf{E} \qquad \textbf{(19)}$$

Therefore, from the diagram, the magnetic intensity over the interface 1 is:

$$H_1 = \sqrt{\frac{\varepsilon_0}{\mu_0}}\left(E_{i1} - E_{r1}^{'}\right) n_0 \cos\theta_{i1} = \sqrt{\frac{\varepsilon_0}{\mu_0}}\left(E_{t1} - E_{r2}^{'}\right) n_1 \cos\theta_{i2} \qquad \textbf{(20)}$$

At boundary 2

$$E_2 = E_{i2} + E_{r2} = E_{t2} \qquad \textbf{(21)}$$

and

$$H_2 = \sqrt{\frac{\varepsilon_0}{\mu_0}}\left(E_{i2} - E_{r2}\right) n_1 \cos\theta_{i2} = \sqrt{\frac{\varepsilon_0}{\mu_0}} E_{t2}\, n_s \cos\theta_{t2} \qquad \textbf{(22)}$$

where n_s is the refractive index of the substrate.

As the wave traverses the film, it will undergo a phase-shift of $k_0\left(2n_1 d_1 \cos\theta_{i2}\right)/2$, which we will denote $k_0 h$ so that,

$$E_{i2} = E_{t1} \exp\left(-ik_0 h\right) \qquad \textbf{(23)}$$

$$E_{r2} = E_{r2}^{'} \exp\left(ik_0 h\right) \qquad \textbf{(24)}$$

Equations (21) and (22) can now be rewritten as

$$E_2 = \left(E_{t1} \exp\left(-ik_0 h\right) + E_{r2}^{'} \exp\left(ik_0 h\right)\right) \qquad \textbf{(25)}$$

and

$$H_2 = \sqrt{\frac{\varepsilon_0}{\mu_0}} n_1 \cos\theta_{i2}\left[E_{t1} \exp\left(-ik_0 h\right) - E_{r2}^{'} \exp\left(ik_0 h\right)\right] \qquad \textbf{(26)}$$

These last two equations can be solved for E_{t1} and E'_{r2} which is substituted in Equations (18) and (20) to yield

$$E_1 = E_2 \cos(k_0 h) + H_2 (i \sin(k_0 h))/Y_1 \quad \textbf{(27)}$$

and

$$H_1 = E_2 Y_I i \sin(k_0 h) + H_2 \cos(k_0 h) \quad \textbf{(28)}$$

where

$$Y_1 = \sqrt{\frac{\varepsilon_0}{\mu_0}} n_1 \cos\theta_{i2} \quad \textbf{(29)}$$

So far, this derivation has been for TE polarisation, if **E** is in the plane of incidence (TM polarisation), the above calculations return similar equations provided that now,

$$Y_1 = \sqrt{\frac{\varepsilon_0}{\mu_0}} n_1 / \cos\theta_{i2} \quad \textbf{(30)}$$

In matrix notation, equations (27) and (28) take the form:

$$\begin{pmatrix} E_1 \\ H_1 \end{pmatrix} = \begin{pmatrix} \cos(k_0 h) & i \sin(k_0 h)/Y_1 \\ Y_1 i \sin(k_0 h) & \cos(k_0 h) \end{pmatrix} \begin{pmatrix} E_2 \\ H_2 \end{pmatrix} \quad \textbf{(31)}$$

or

$$\begin{pmatrix} E_1 \\ H_1 \end{pmatrix} = \mathbf{M}_1 \begin{pmatrix} E_2 \\ H_2 \end{pmatrix} \quad \textbf{(32)}$$

where $\mathbf{M}_1$ is the known as the *characteristic matrix*. The method can be extended to calculate the fields of a arbitrary system of dielectric layers. The equation simply becomes,

$$\begin{pmatrix} E_1 \\ H_1 \end{pmatrix} = \prod_i^p \mathbf{M}_i \begin{pmatrix} E_{p+1} \\ H_{p+1} \end{pmatrix} \quad \textbf{(33)}$$

where p is the number of layers

$$M = \prod_{i=1}^{p} \mathbf{M}_i = \begin{pmatrix} m_{11} & m_{12} \\ m_{21} & m_{22} \end{pmatrix} \quad \textbf{(34)}$$

Reformulating (32) in terms of (18),(20) and (22) and using the admittance of the initial layer and substrate layer. We obtain

$$\begin{bmatrix} (E_{i1} + E_{r1}) \\ (E_{i1} - E_{r1})Y_0 \end{bmatrix} = M_1 \begin{pmatrix} E_{t2} \\ E_{t2}Y_s \end{pmatrix} \quad \textbf{(35)}$$

When the matrices are expanded, the last relation becomes

$$1 + r = m_{11}t + m_{12}Y_s t \quad \textbf{(36)}$$

and

$$(1 - r)Y_0 = m_{21}t + m_{22}Y_s t \quad \textbf{(37)}$$

where we have used,

$$\begin{aligned} r &= E_{r1} / E_{i1} \\ t &= E_{t2} / E_{i1} \end{aligned} \quad \textbf{(38)}$$

Re-arranging for *r* and *t* gives equations for the amplitude *r* reflection coefficient and transmission coefficient respectively.

$$r = \frac{Y_0 m_{11} + Y_0 Y_s m_{12} - m_{21} - Y_s m_{22}}{Y_0 m_{11} + Y_0 Y_s m_{12} + m_{21} + Y_s m_{22}} \quad \textbf{(39)}$$

$$t = \frac{2Y_0}{Y_0 m_{11} + Y_0 Y_s m_{12} + m_{21} + Y_s m_{22}} \quad \textbf{(40)}$$

Where Y_0 and Y_s are the admittance of the initial layer and the substrate respectively. The power reflection coefficient, is

$$R = |r|^2 \quad \textbf{(41)}$$

The phase of the wave is given by taking the argument of the amplitude reflection coefficient. [50]

$$\Phi = \arg(r) \quad \textbf{(42)}$$

As an example, the diagram below shows the calculated reflectivity spectrum for a 20 period GaAs/AlAs DBR mirror. The refractive index used in these calculations based on the single oscillator Sellmeier [51] equation having both composition and wavelength dependent. It has the form:

$$n(x,\lambda) = \sqrt{A(x) + \frac{B}{\lambda^2 - C(x)} - D(x)\lambda^2} \quad \textbf{(43)}$$

where $A(x)$, B,$C(x)$, $D(x)$ are constants with the values given in Table 4 and x is the alloy fraction of Aluminium.

$A(x)$	$10.9060-2.92x$
B	0.97501
$C(x)$	$(0.52868-0.735x)^2$ $x \leq 0.36$
	$(0.30386-0.105x)^2$ $x > 0.36$
$D(x)$	$0.002467(1+1.41x)$

Table 4 Internal functions used within the GaAs composition and wavelength dependent refractive index formula.

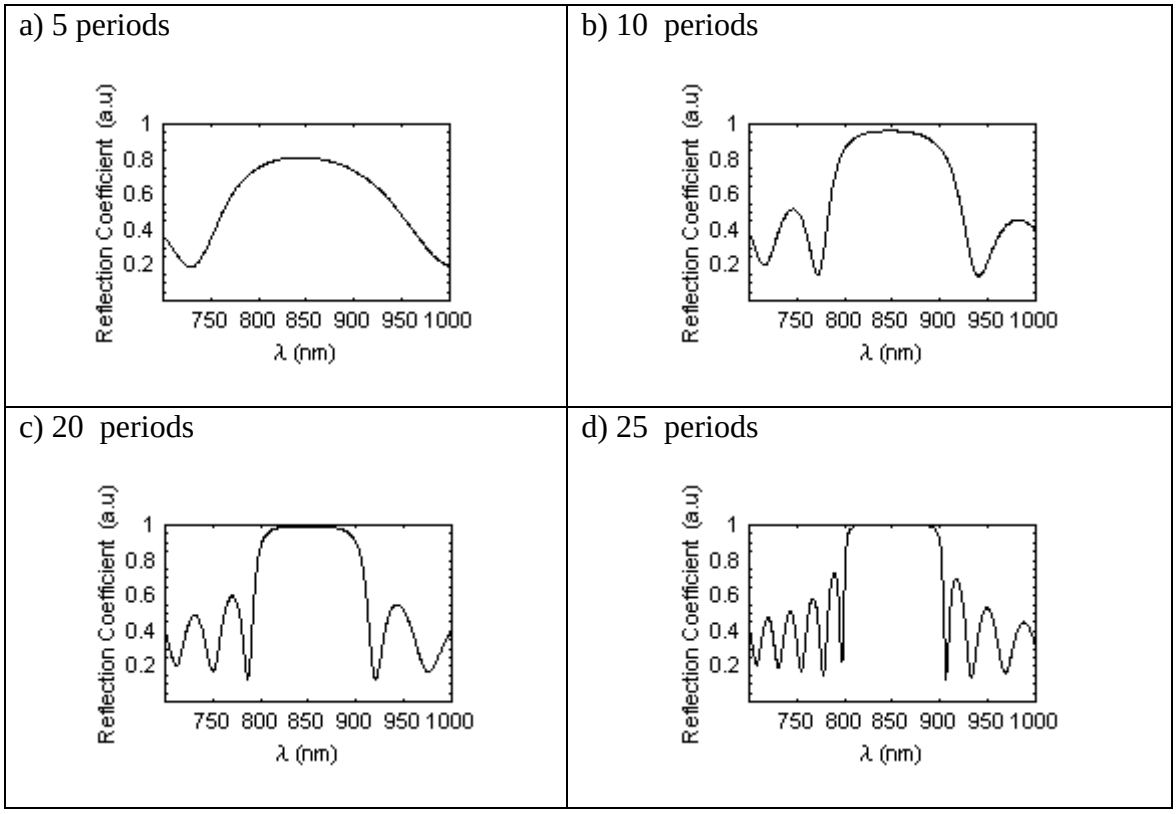

Figure 14. Reflectivity plots of GaAs/AlAs DBR with increasing number of periods.

The effect of adding more periods to a DBR stack is shown in Figure 14. As more layers are added, the region of high-reflectivity known as the stop-band develops. The stop-band is limited in extent and falls abruptly on either side to a low oscillatory value. The addition of extra periods does not alter the width of the stop band significantly but increases the value of the reflectivity.

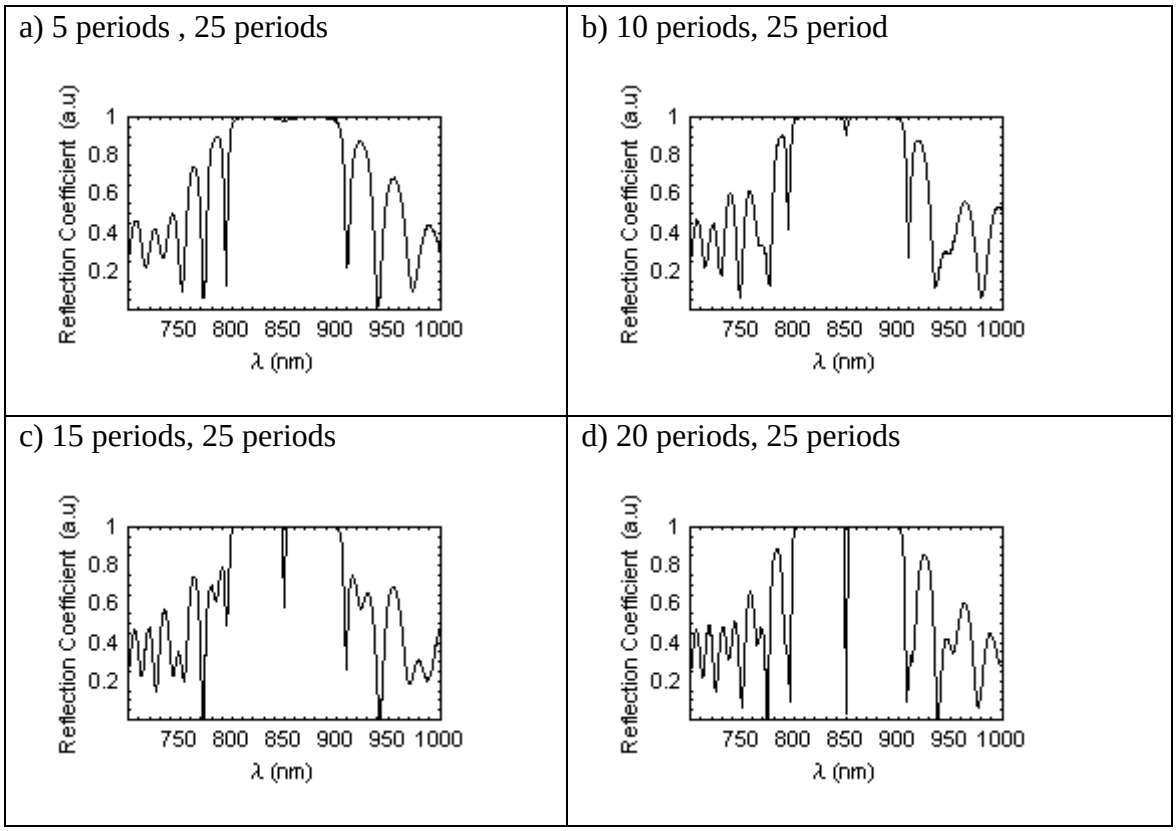

Figure 15. Calculated reflectivity spectrum of a simple GaAs/AlAs VCSEL structure showing the effect of increasing the number periods in the top DBR. The cavity mode becomes more pronounced with increasing number of periods in the top DBR.

The addition of a second DBR, separated from the first DBR by a single layer of half of the design wavelength, creates a resonant cavity. Figure 15 shows the reflectivity spectrum for a simple VCSEL structure consisting of a constant number of periods in the bottom DBR on a GaAs substrate and $\lambda/2$ cavity layer of GaAs cavity layer. The top DBR has a variable number of periods to illustrate the development of the cavity resonance within the device.

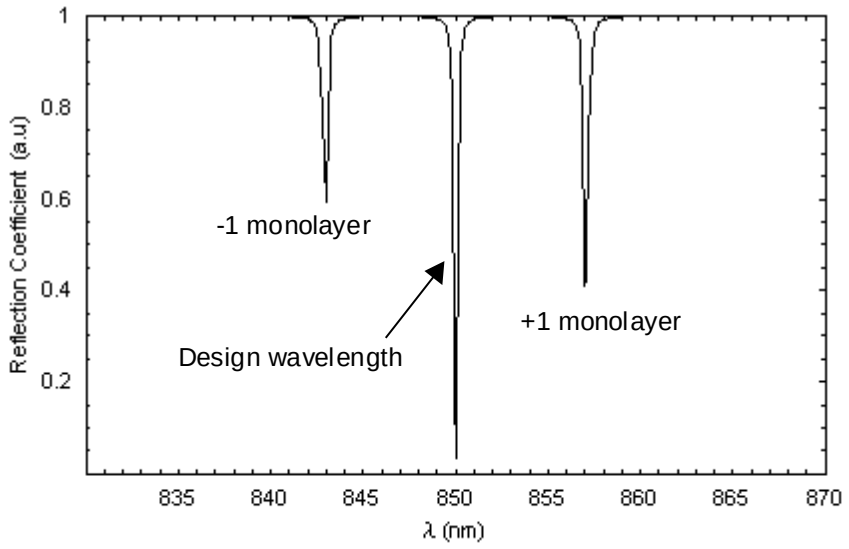

Figure 16. Errors in growth of ± 1 monolayer in whole device structure lead to a walk-off in the whole reflectivity profile.

With so many layers making up the structure, the correct thickness of each layer is critical. Figure 16 shows an enlarged portion of the reflectivity spectrum for the same simple VCSEL structure as in Figure 15 and shows the effect of both overgrowth and undergrowth of a single monolayer applied to each layer of the entire structure. A monolayer of growth corresponds to an extra 5.65 Å in GaAs[52]. The accumulation of error with each layer causes the whole reflectivity spectrum is shifted by 7 nm above or below the design wavelength with overgrowth or undergrowth respectively.

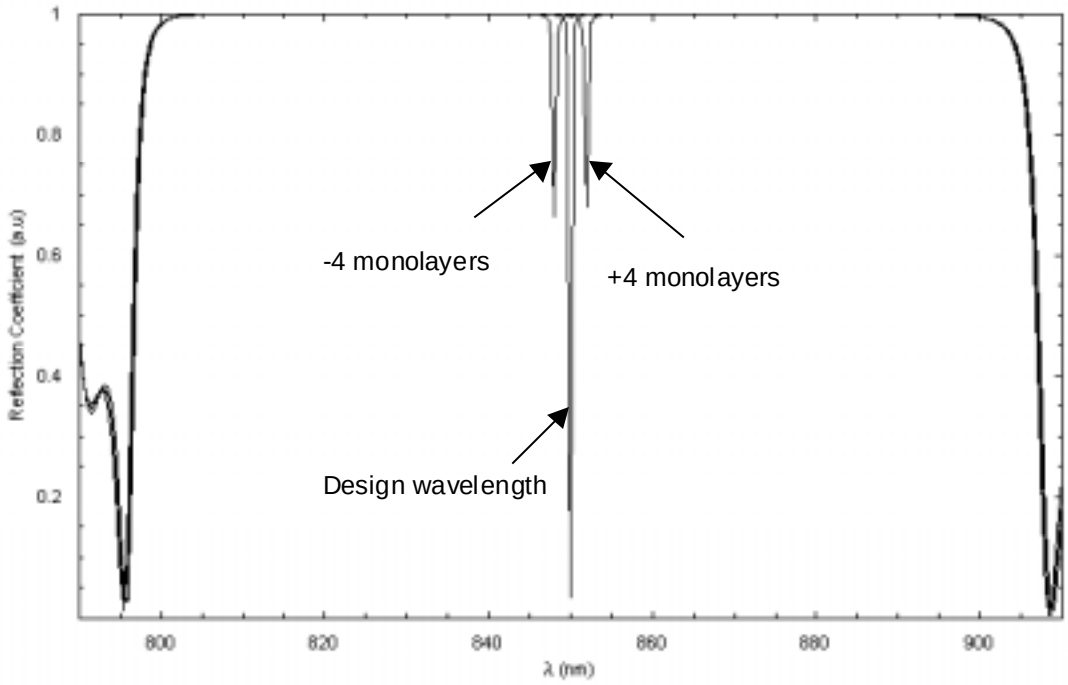

Figure 17. Monolayer changes in just the cavity region cause small shifts in the cavity resonance from the design wavelength.

Errors in the growth of the cavity alone are less critical as shown by Figure 17. An increase of 4 monolayers in the cavity creates very little movement in the stop band and cause the cavity resonance to shift by ± 4 nm from the design wavelength for an overgrowth or undergrowth of 4 monolayers respectively.

2.5.2 Temperature Dependent Operation of Edge-Emitting Lasers and VCSELs.

The temperature dependence of edge-emitting lasers comes from Joule heating of the cavity. As the temperature increases, the atoms gain kinetic energy and their average atomic separation increases the physical length of the cavity and its refractive index. To

accommodate this increase in the optical path length of the cavity, the resonant mode must also move to longer wavelengths. The cavity length is much greater than the emission wavelength for a Fabry-Perot laser, therefore a large number of closely-spaced modes are present. Only a small temperature increase is required to causes an adjacent mode to become the lasing mode. This shift in the lasing mode with temperature is known as mode hopping. The change in temperature also cause a change in the threshold current. An empirical result describing the temperature dependence with threshold current density of Fabry-Perot lasers is:

$$J_{th} = J_0 Exp\left(T / T_o\right) \qquad \textbf{(44)}$$

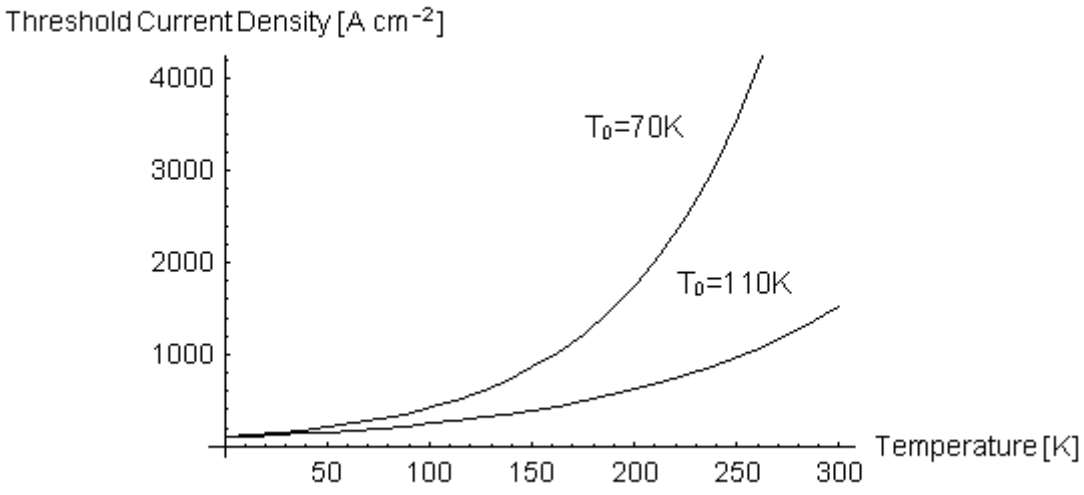

Figure 18. Threshold current density against temperature for two Fabry-Perot lasers. The top curve is for an InGaAsP laser diode while the lower curve is typical of a GaAs laser. As can seen, higher T_0 values are less temperature sensitive.

Higher values of T_0 are favourable, since for a given temperature the threshold current density is reduced. Typical values of T_0 for GaAs are 110 K while InGaAsP have values of T_0 between 40-80 K. The rapid increase in threshold current with temperature in InGaAsP lasers is due to carrier leakage over the heterobarriers, [53] Auger recombination[54,55,56] and intervalence band absorption of the light. [57] Even for good GaAs edge emitting lasers, the threshold current increases steadily with temperature. There is a decrease in the degeneracy of the electron and hole population as the temperature is increased. At higher temperatures, the carrier populations are distributed over larger energy ranges, giving larger amounts of spontaneous emission and therefore a higher current, for the same degree of population inversion.

The short cavity length of VCSELs usually allow for only a single mode within the gain spectrum, therefore mode hoping does not occur. The cavity mode of the VCSEL shifts with temperature, with gain occurring only if the cavity resonance is within the gain spectrum.

The dominant temperature dependent mechanism is the temperature dependence of the energy gap in the semiconductor. This has a temperature dependence given by [58],

$$E_g(T) = E_0 - \frac{\alpha T^2}{\beta + T} \qquad \textbf{(45)}$$

Where E_0 is the energy gap at T=0K, α and β are empirical fitting parameters for a given semiconductor where β is close to the Debye temperature. The variation in the refractive index within each layer of the DBR is linear with temperature. [59]

$$n(T) = n_0 + \Delta n T \qquad \textbf{(46)}$$

where n_0 is the refractive index at T=0 K and Δn is the change in refractive index per unit temperature. Modifying the refractive index in this way de-tunes the cavity wavelength. In addition, there is a small effect due to the actual physical expansion of the layers, however, the effect of this is an order of magnitude smaller than the change in refractive index so for most purposes can be neglected.

2.6 Laser Gain Calculations

2.6.1 Density of States

For a laser to reach a state, where stimulated emission is the dominant mode of emission, a microscopic description demands that there are free states in the conduction and valence band. For this to occur we need to look at the mathematical description of how the number of states are distributed with energy and their availability for occupancy. In addition, the emission is regulated by the quantum mechanical interaction between photons and electrons. The important concepts for gain calculations are the density of states, energy levels in a 1-D potential well and the distribution functions, all of which we summarise below. Equation (47) is the density of states per unit energy per unit volume at an energy E in the conduction band for a bulk material while equation (48) is the density of states in a quantum well,

$$\rho_e(E) = \frac{1}{2\pi^2}\left(\frac{2m^*}{\hbar^2}\right)^{3/2}(E)^{1/2} \qquad \textbf{(47)}$$

$$\rho_e(E) = \frac{m^*}{\pi\hbar^2 L_z}\sum_n H(E - E_n) \qquad \textbf{(48)}$$

Where L_z is the width of the quantum well and H is the Heaviside function which has the following form:

$$H(x-a)=\begin{cases}1 & x \geq a \\ 0 & x<0\end{cases} \quad \textbf{(49)}$$

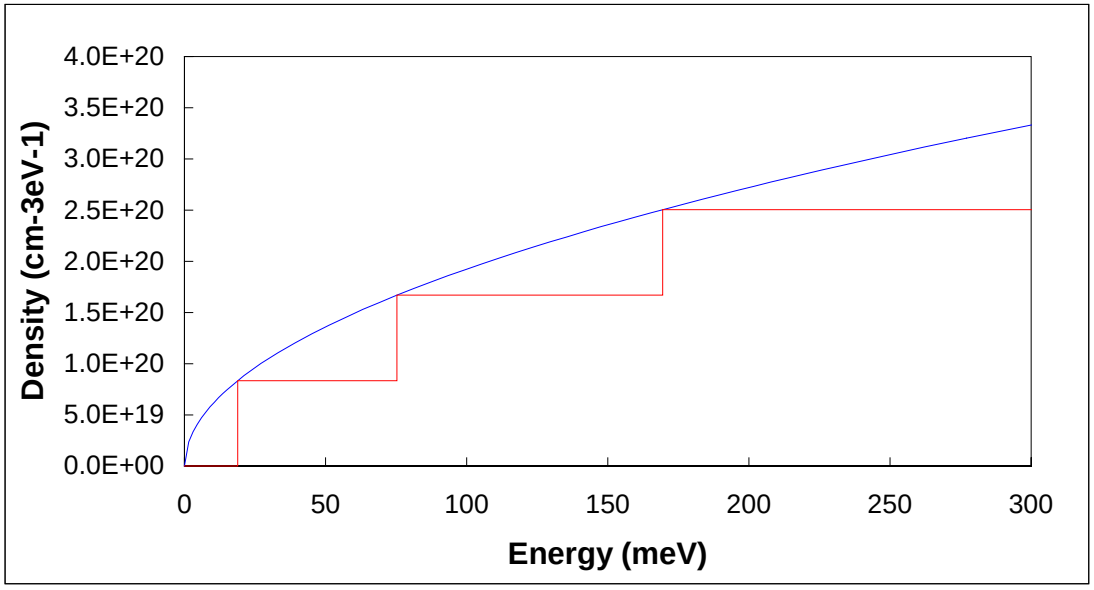

Figure 19. Density of states for bulk material and quantum well structures. The effect of confining the k values in one direction is to separate the energy levels with the other two k-directions following the bulk form, producing a staircase like density of states.

2.6.2 Fermi Distribution

The occupation probability of the energy levels as defined above by the electrons is described by the Fermi-Dirac distribution function.

$$f(E)=\frac{1}{1+Exp\left(\frac{E-E_f}{k_BT}\right)} \quad \textbf{(50)}$$

Where E_f is the Fermi level. This the energy at which there is a fifty percent probability of finding an electron.

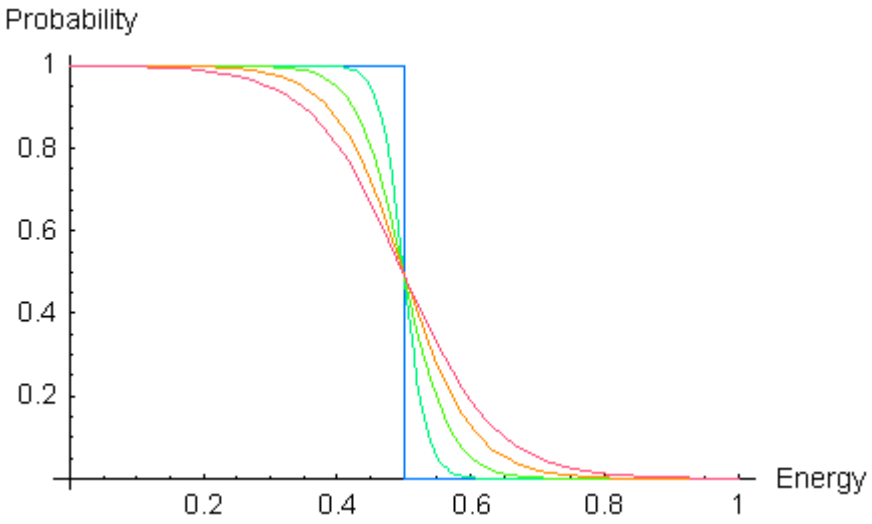

Figure 20. Fermi-Dirac distribution function with increasing temperature (from blue through to red). At T=0 K all the electrons are in the valence band. As the temperature increases, there is a greater probability of finding an electron in the conduction band.

Together with the density of states function, the Fermi distribution gives the number of states and their distribution of occupied states. The Fermi-level is only really meaningful under equilibrium conditions. In a semiconductor laser, the carriers are being introduced into the active region. Conditions are far from equilibrium, however, the concept of the Fermi-level need not be abandoned. Instead, a Fermi-level is defined for electrons in the conduction band and the holes in the valence band. These are not in equilibrium with the transitions between the conduction band and valence band but are in equilibrium with themselves. Together they give the energy where the occupation probability is 50% within each band. The carrier density is defined in terms of the integral of the density of states multiplied by the Fermi distribution function. However, it is often more useful to

know the Fermi-level for a given carrier concentration. Another method such as the Joyce Dixon[60] (Equation (51)) or Nilsson[61] (Equation (52)) approximation is more useful.

$$\frac{E_f}{k_B T} = \log r + \frac{1}{\sqrt{8}} r - \left(\frac{3}{16} - \frac{\sqrt{3}}{9} \right) r^2 + \ldots \quad \textbf{(51)}$$

$$\frac{E_f}{k_B T} = \frac{\log r}{1-r} + \left(\frac{3\sqrt{\pi} r}{4} \right)^{2/3} + \frac{8\sqrt{\pi} r}{3\left(4 + \sqrt{\pi} r\right)^2} \quad \textbf{(52)}$$

where in each case

$$r = n / N_{c,v} = \frac{n}{2\left(\frac{m_{c,v} kT}{2\pi\hbar^2} \right)^{3/2}} \quad (n = p) \quad \textbf{(53)}$$

$N_{c,v}$ is the effective density of states and the subscripts refer to the conduction and valence bands.

2.6.3 Momentum Matrix Element

The momentum matrix element for quantum well active regions is highly dependent on direction of the emission and has been explained in depth by Sale.[51] The momentum matrix element is more simple for bulk material.

$$\left| M_{ij} \right|^2 = O_{ij} \sum_{v\pm} \sum_{c\pm} \left| \langle u_v \left| \hat{\mathbf{e}}.\mathbf{p} \right| u_c \rangle \right|^2 \quad \textbf{(54)}$$

where **e** is the unit vector in the direction of the electric field of polarisation and **p** is the momentum operator, u_v and u_c are periodic wavefunctions known as Bloch functions, O_{ij} is the overlap integral of the initial electron and final hole states. The matrix element is found from the initial and finial spin states. The result for bulk material is given in terms

of the momentum matrix element calculated by Kane. The average momentum matrix element is M_0^2 where M_0 is

$$M_0^2 = \frac{1}{6}\left(\frac{m_0}{m_e} - 1\right)\frac{E_g + \Delta}{E_g + \frac{2}{3}\Delta} m_0 E_g \quad \textbf{(55)}$$

Where E_g is the energy gap, m_e is the effective mass in the conduction band and Δ is the spin-orbit splitting energy. In practice, an energy parameter E_p is defined such that

$$M_0^2 = \frac{m_0}{6} E_p \quad \textbf{(56)}$$

Material	GaAs	AlAs	InAs	InP	GaP
E_p **(eV)**	25.7 (25.0) [62]	21.1	22.2	20.7 (16.7) [62]	22.2

Table 5. Values of E_p used to calculate the bulk momentum matrix element for some common binary semiconductors. [43]

2.6.4 The Absorption Coefficient

In Section 2.1, we looked at the radiative recombination process. For stimulated emission to occur, the downward transition must exceed the rate of transitions to the conduction band.

$$B_{21} f_2 (1 - f_1)\rho(E_{21}) > B_{12} f_1 (1 - f_2)\rho(E_{21}) \quad \textbf{(57)}$$

where $\rho(E_{21})$ is the density of photons at energy E_{21}. With B_{21}=B_{12}, this equation becomes

$$f_2 (1 - f_1) > f_1 (1 - f_2) \quad \textbf{(58)}$$

f_1 and f_2 are given by the Fermi distribution which can be shown to reduce to

$$F_2 - F_1 > E_2 - E_1 \quad \textbf{(59)}$$

The last equation gives the famous Bernard-Duraffourg condition,[63] which states that for population inversion to occur, the separation of the quasi-Fermi levels must be greater than the energy of the emitted light. The combination of the density of states in the conduction band and valence band, momentum matrix element and difference in the quasi Fermi levels gives the absorption coefficient. [64]

$$\alpha(E) = \frac{\pi q^2 \hbar}{\varepsilon_0 m^2 cnE} \int_{-\infty}^{\infty} \rho_c(E')\rho_v(E'')\left|M(E', E'')\right|^2 \left[f_c(E'') - f_v(E')\right] dE' \quad \textbf{(60)}$$

Where $E = \hbar\omega$ is the photon energy and E' becomes the variable of integration. $E'' = E' - \hbar\omega$. When several valence bands are present, as in III-V semiconductors, the absorption coefficient is the sum of the terms similar to Equation (60) for each valence band. In the last equation, *M(E',E'')* is the matrix element for transitions between the conduction band and valence band. However, since most of the transitions occur to and from the heavy-hole band, this is a good first approximation.

Equation (60) uses no k-selection for transitions from the conduction band to the valence band. The assumption of no-k selection was used by Lasher and Stern [64], who assumed that the impurities had formed a band which merged with the valence band. In edge-emitting lasers, the impurity concentration can be considerable (of the order 10^{18}-10^{19} per cm^3 [65]). The effect of no k-selection is to add a low energy tail to the gain spectrum. However, the details of this calculation are beyond the scope of this thesis. The

calculation of the gain spectra shown in Figure 21, used k-selection which is more simple to implement and gives a first approximation to the gain spectrum but without the low energy band tails.

The absorption coefficient is usually positive, however, under the condition of population inversion, it becomes negative indicating gain or amplification. Figure 21 shows how the gain spectra varies with increasing carrier concentration.

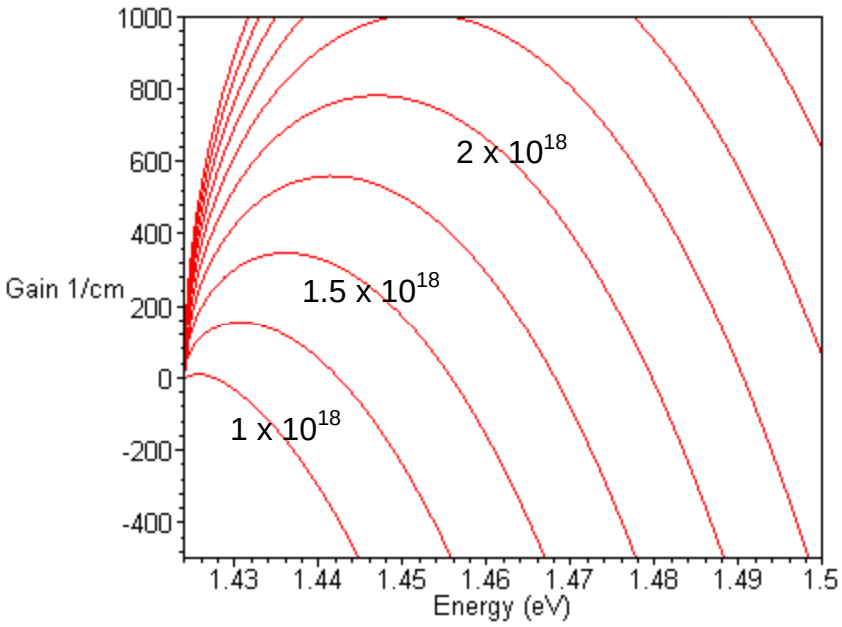

Figure 21. Calculated gain spectrum for GaAs based semiconductor laser with carrier concentration using simple model of gain assuming fixed momentum matrix element and k selection. Greater carrier concentration increases the gain as the quasi Fermi-levels are more widely separated.

2.6.5 The Marinelli Approximation

A better approximation, compared to the no k-selection model, for the absorption coefficient in bulk active region of a laser cavity has been developed by Marinelli.[66] tails

By approximating the integral in Equation (60), this produces a more realistically shaped gain curve with low energy band tails.

$$\alpha = \frac{Bc^2}{4n^2\pi}\left(\frac{4\pi^2 m_c m_v}{h^2}\right)^{3/2}\left(\frac{\Delta E}{E}\right)^2 \frac{\sinh\left[\left(F_c + F_v - \Delta E\right)/2k_B T\right]}{\cosh\left[\left(F_c + F_v - \Delta E\right)/2k_b T\right] + \cosh\left[\left(F_c - F_v\right)/2k_B T\right]} \quad \textbf{(61)}$$

When the absorption coefficient is known, the spontaneous emission coefficient can be obtained. F_c and F_v are the electron and hole quasi-Fermi levels, respectively, measured positively into the bands from the band edges. ΔE, is the difference between the photon energy and the energy-gap and B is the bi-molecular recombination constant which is assumed to be independent of temperature, E is the energy of the emission wavelength 1.5 μm ≡0.826 eV. In practice, this has a weak temperature dependence, [67] but does not significantly alter our results. Other symbols used have their conventional interpretation.

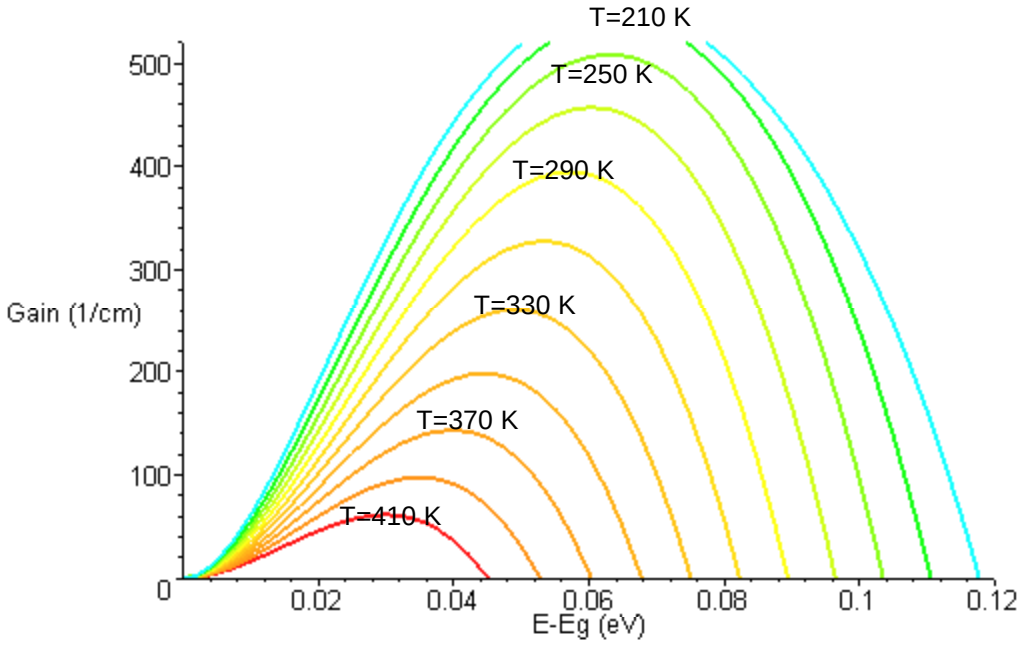

Figure 22. Gain Spectrum calculated using Marinelli approximation for InGaAsP based laser over a temperature range of T=210 K to T=410 K, with a carrier concentration of n=2x10^{18} cm^{-3}.

Figure 22 shows the gain spectrum for a bulk active region InGaAsP based laser, calculated using the Marinelli approximation with a constant carrier concentration of $n=2x10^{18}$ cm^{-3} over a temperature range of T=210 K (blue curve) to T=410K (red curve). As the temperature increases the peak gain decreases and shifts to lower energies, corresponding to longer wavelengths. We shall use this model in section 4.2.1 to verify our results.

2.6.6 Gain in Quantum Well Lasers

The gain spectrum runs along similar lines to that for bulk material, however there are a number of differences. Firstly, the density of states function used is the staircase like function described in Section 2.6.1 and the transition matrix elements are more complicated, since the interaction between the photons and electrons are strongly dependent on the polarisation of the light. Full discussion of this is beyond the scope of this discussion.

The effect of the these modifications is to create a gain spectrum which has a sharp onset at the first energy level with transitions from the first conduction band to the heavy-hole band. The gain from this transition tails off with energy until the next energy level transition is reached where upon, there is a second, although less intense peak since recombination occurs mostly from the first conduction and valence band energy levels.

2.6.7 Finite Barrier Quantum Well

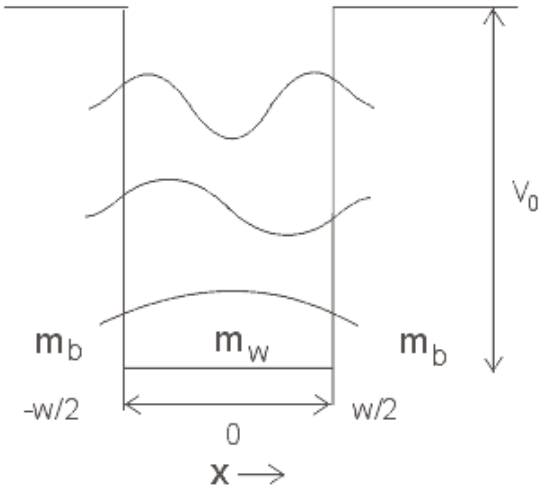

Figure 23. A schematic diagram of a finite barrier well of width w and potential V_0 showing the first three wavefunctions .

Solving the Schrödinger equation for a finite potential will produce eigenvalues for the energy levels within the well. Consider a potential well centred on the origin of width *w* and barrier height V_0. Inside the well, the potential is zero, the Schrödinger equation is

$$\frac{\hbar^2}{2m}\frac{d^2\psi(x)}{dx^2} + k_1\psi(x) = 0 \qquad |x| < w/2 \text{ where } k_1 = \sqrt{\frac{2mE}{\hbar^2}} \qquad \textbf{(62)}$$

Outside the well

$$\frac{\hbar^2}{2m}\frac{d^2\psi(x)}{dx^2} - k_2\psi(x) = 0 \qquad |x| \geq w/2 \text{ where } k_2 = \sqrt{\frac{2m(V_0 - E)}{\hbar^2}} \qquad \textbf{(63)}$$

For even wavefunctions, the solution of the Schrödinger equation within the well is:

$$\psi(x) = \begin{cases} C_1 \exp(-k_2|x| - w/2) & |x| \geq w/2 \\ C_2 \cos k_1 x & |x| < w/2 \end{cases} \qquad \textbf{(64, 65)}$$

The wavefunction and its derivative divided by the mass must be continuous at the boundaries of the well.

$$C_1 = C_2 \cos k_1 \frac{w}{2} \quad \textbf{(66)}$$

$$\frac{k_2}{m_b} C_1 = \frac{k_1}{m_w} C_2 \sin k_1 \frac{w}{2} \quad \textbf{(67)}$$

Eliminating C_1 and C_2, we obtain the quantisation condition:

$$k_2 = \frac{m_b k_1}{m_w} \tan k_1 \frac{w}{2} \quad \textbf{(68)}$$

Similarly for odd wavefunctions,

$$\psi(x) = \begin{cases} C_1 \exp\left[-k_2 \left(x - \frac{w}{2} \right) \right] & x > w/2 \\ C_2 \sin k_1 x & |x| \le w/2 \\ -C_1 \exp\left[k_2 \left(x + \frac{w}{2} \right) \right] & x < -w/2 \end{cases} \quad \textbf{(69, 70, 71)}$$

The boundary conditions give:

$$C_1 = C_2 \sin k_1 \frac{w}{2} \quad \textbf{(72)}$$

$$\frac{-k_2 C_1}{m_b} = \frac{k_1}{m_w} C_2 \cos k_1 \frac{w}{2} \quad \textbf{(73)}$$

The eigenequation is thus

$$k_2 = -\frac{m_b k_1}{m_w} \cot k_1 \frac{w}{2} \quad \textbf{(74)}$$

The solutions for the quantised eigen energies can be obtained by $k_1 w/2$ and $k_2 w/2$ using a graphical approach since

$$\left(k_1 \frac{w}{2}\right)^2 + \frac{m_w}{m_b}\left(k_2 \frac{w}{2}\right)^2 = \frac{2m_w V_0}{\hbar^2}\left(\frac{w}{2}\right)^2 \qquad \textbf{(75)}$$

and

$$k_2\sqrt{\frac{m_b}{m_w}}\frac{w}{2} = \frac{m_b k_1}{m_w}\frac{w}{2}\tan k_1 \frac{w}{2} \qquad \text{for even solutions} \qquad \textbf{(76)}$$

$$k_2\sqrt{\frac{m_b}{m_w}}\frac{w}{2} = -\frac{m_b k_1}{m_w}\frac{w}{2}\cot k_1 \frac{w}{2} \qquad \text{for odd solutions} \qquad \textbf{(77)}$$

plotting $k_2\sqrt{\frac{m_b}{m_w}}\frac{w}{2}$ against $k_1\frac{w}{2}$ produces a graph like Figure 24. The potential generates a circle of radius $\sqrt{\frac{2m_w V_0}{\hbar^2}}\frac{w}{2}$. The energy levels in the well are found from the intersection of the tangent and cotangent with the circular arc within the positive quarter.

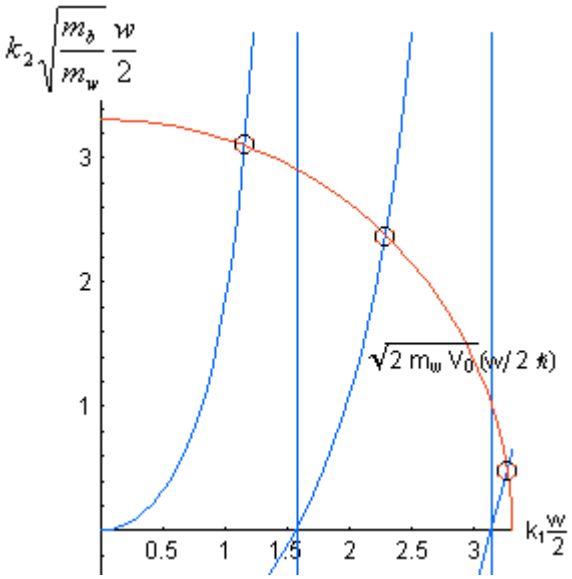

Figure 24. The graphical solution for finite barrier quantum well.

3. Experimental Techniques

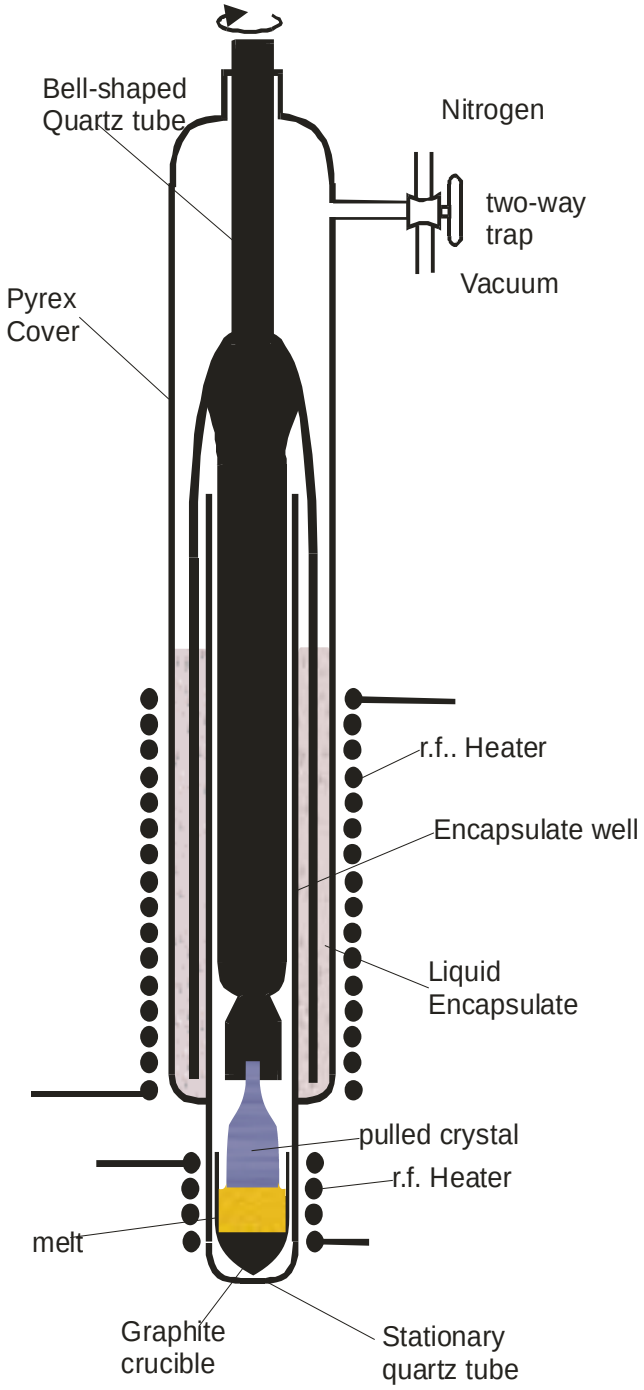

Figure 25 Liquid Encapsulated Czochralski crystal growth process

In this chapter we present the methods of growth and fabrication methods used in creating the very pure crystals used in the manufacture of the VCSEL devices used in these experiments. Once an understanding of the growth and fabrication technique has been established we examine the experimental methods used in this dissertation to characterise and investigate the VCSELs.

3.1.1 Liquid Encapsulated Czochralski Crystal Growth (LEC)

The first step in making any device is to start with a wafer of semiconductor material. These wafers are sliced from a large single crystal known as a *boule*.

Figure 25 shows the apparatus used to grow the boule. A small seed crystal of the material to be grown is lowered to the surface of the melt and then drawn upwards, slowly.

As the seed crystal is pulled from the melt, it draws with it a layer of molten material. This material cools gradually, taking on the same crystalline structure as the seed crystal. Pellets of dopant material are added to the melt if extrinsic semiconductor material is required. Making compound semiconductor crystals is somewhat more difficult because the vapour pressures of the constituent materials are different. At the temperature required to melt the higher temperature material, the lower melting-point material has evaporated. Evaporation can prevented by the use of a liquid-lid or encapsulate. The encapsulate must of course be made of a material that is less dense than the material in the crucible and must not be absorbed in the melt. For making Indium Phosphide crystals, a Boric-Oxide (B_2O_3) encapsulate [68], coupled with a high pressure of inert gas in the chamber, prevents the volatile phosphorous from vaporising from the melt.

3.1.2 Wafer Preparation

The next stage of the fabrication process is to turn the single crystal of semiconductor material into many thinly sliced wafers. The boule of semiconductor has a non-uniform diameter. In commercial wafer processing, high yields depend on the uniformity of the wafers. The semiconductor crystal is machined on a lathe into a cylinder. The orientation of the crystal planes is fixed by the seed crystal, usually {100} [69], for many semiconductors including GaAs and InP. The orientation within the plane must be fixed by x-ray diffraction. Once the geometry of the cylinder is established, a flat is ground along the its length. In devices such as Fabry-Perot lasers, the wafer has crucial cleavage

planes that will form the mirrors. The cylinder is sliced into thin wafers using a diamond annular saw. The cut wafers have some saw marks that must be removed. This is achieved using a combination of mechanical polishing and chemical etching until the surface of the wafer is optically flat.

3.1.3 Molecular Beam Epitaxy (MBE)

Molecular Beam Epitaxy (MBE) is a growth technique used for building up layered crystalline surfaces on a substrate crystal. A schematic diagram of the growth chamber of an MBE machine is shown in Figure 26. Generally, these machines consists of three vacuum sections, of which the growth chamber is the most important. The buffer section (not shown) is involved in the preparation and storage of the wafers before entering the growth chamber. While the load-lock is used to insert and remove samples while retaining the integrity of the vacuum. Samples are loaded onto a rotational magnetic holder for Continual Azimuthal Rotation, commonly know as the (CAR). Cyropanels are used in conjunction with the vacuum system to keep the partial pressure of undesirable gases such as CO_2 and H_2O to around 10^{-11} Torr. The principle of operation of the cryopanels, is that gaseous substances are bound to the cold surfaces within the pump by means of cryocondensation, cryosorption or cryotrapping.

Epitaxial growth starts with the many heated cells, called effusion cells or *Knudsen* cells, that contain a compound required for the addition of a particular atomic species into the vacuum chamber. Each source is independently heated until the atoms of the source material have enough kinetic energy to escape by thermionic emission. An advancement of MBE, Gas Source MBE (GSMBE), uses room temperature gases for the source

materials, thus avoiding significant contamination problems and the necessary higher substrate temperatures that can cause segregation of dopant atoms.

Within the ultra-high vacuum, the free atoms have a long mean-free path and collisions with other atoms are infrequent. Atoms from the sources are able to travel in a straight line until they collide with the substrate material. A computer remotely operates the shutter controls, allowing the emission of different species of atom to be directed at the substrate. The typical rate of growth with MBE is around a single mono-layer per second. [70] Although quite slow, this allows for abrupt changes in material composition. Under the right conditions, of substrate temperature and beam pressure, the beam of atoms will attach to the substrate material and an epitaxial layer will begin to form.

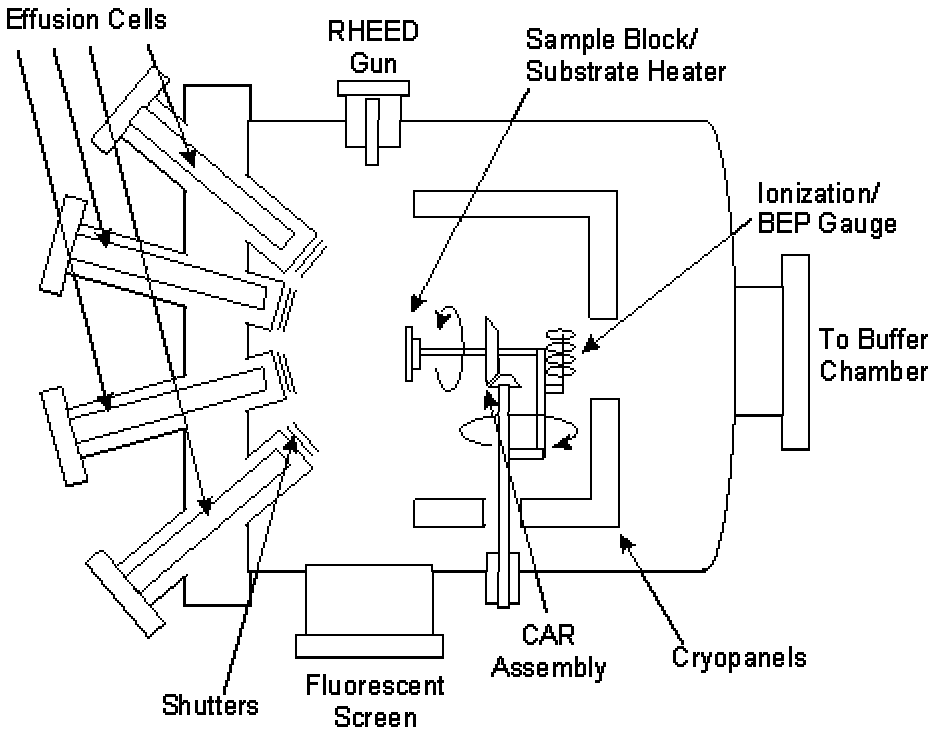

Figure 26. Schematic diagram of a MBE machine.

Control over the thickness is determined using an ion gauge mounted to face the beam sources. The Beam Equivalent Pressure (BEP) of the material sources can be used to measure the rate of growth of the layers. Alternatively, Reflection High-Energy Electron Diffraction (RHEED) is another useful measuring technique [71]. Electrons are emitted from an electron gun at a glancing incidence (about 1°) to the CAR. The electrons are Bragg diffracted by the surface. The diffracted beams form a distinctive pattern when they strike a phosphor screen. Figure 27 shows the process schematically. Starting from a flat substrate, the electrons are not scattered greatly and are recorded as an intense array of streaks. As material is deposited on the surface, the atoms create islands of epitaxial growth with a concomitant increase in the roughness of the surface. The diffraction become more diffuse with an associated decrease in the intensity of the streaks. The isolated islands join together and create new flat surfaces as the deposition continues, with the original surface becoming voids in the new layer of material. As yet more material forms, the voids begin to fill up and the intensity of the streaks increases once again. In practice, the intensity does not reach as high a value, since the process of deposition is random and the surface never regains the completely flat profile of the initially polished substrate. By monitoring the frequency of the oscillations in the intensity of the diffracted beams, one can estimate the thickness and rate of growth of the epitaxial material.

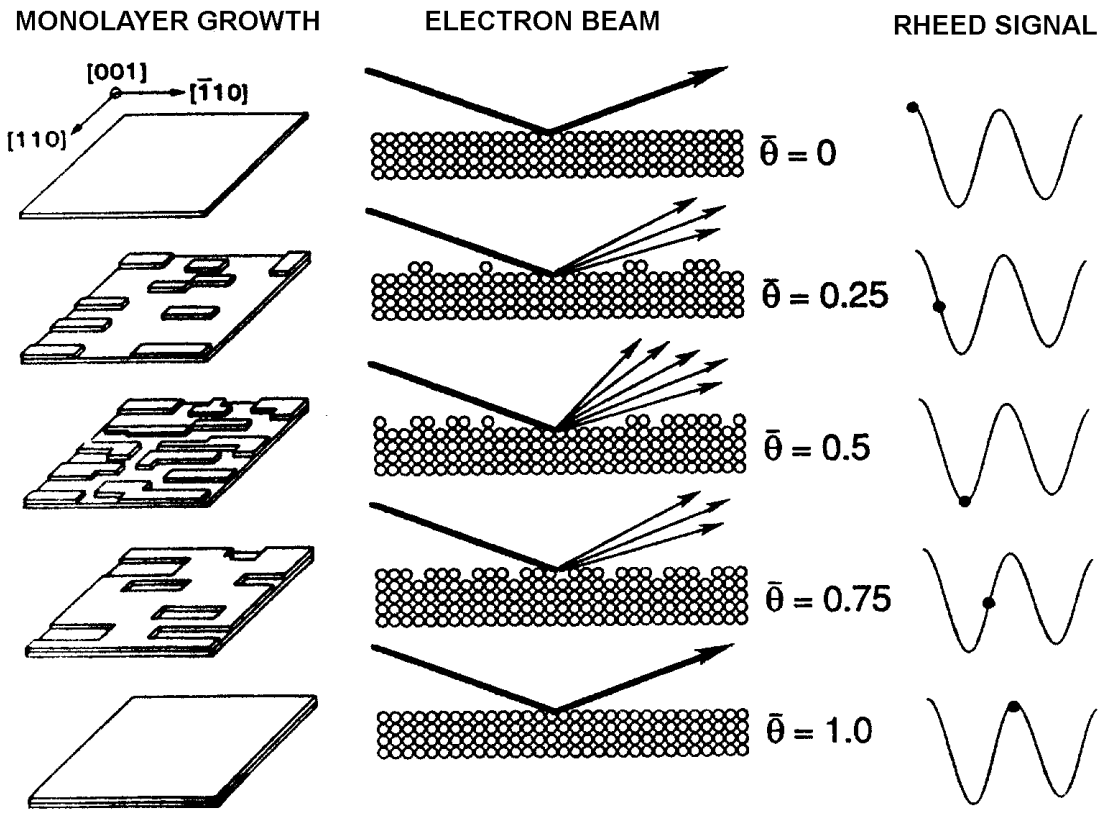

Figure 27. Reflection High-Energy Electron Deflection (RHEED) measurement system. Electrons are scattered more when a new mono-layer of atoms are being formed. The intensity of the RHEED signal oscillates as new layers are progressively formed.

3.1.4 Metal-Organic Chemical Vapour Deposition (MOCVD)

MOCVD or MOVPE (Metal-Organic Vapour Phase Epitaxy) is another widely used method of creating controllable epitaxial layered structures by atomic deposition over a substrate material. [72]

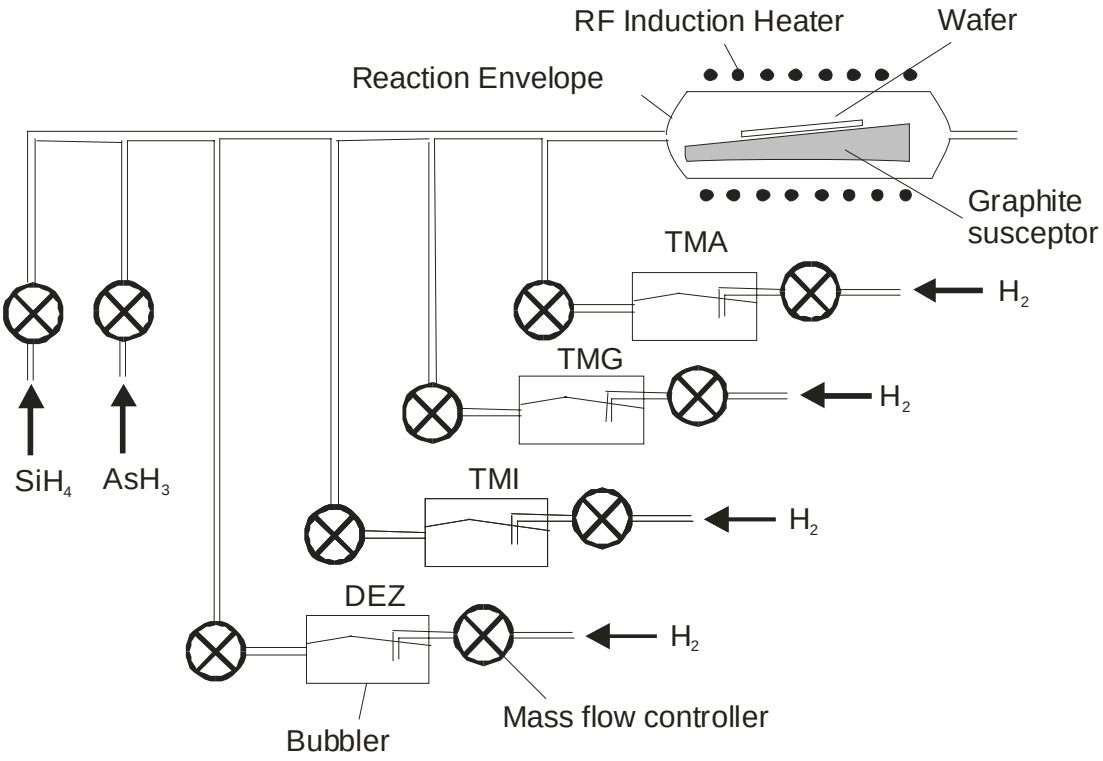

Figure 28 Schematic diagram of the MOCVD process.

The substrate wafer is placed on a graphite susceptor inside a reaction vessel and heated by an RF induction heater. The temperature depends on the type of compounds grown, but it is usually between 500°C and 700°C.

Growth occurs in an atmosphere of Hydrogen at a pressure between 100 and 700 Torr. The growth precursors decompose on contact with the hot substrate to form epitaxial layers. Group V precursors are AsH_3 (arsine) while group III are $Ga(CH_3)_3$ trimethylgallium (TMG). The other group III precursors shown in the diagram are: $Al(CH_3)_3$ trimethylaluminium (TMA) for Aluminium, $In(CH_3)_3$ trimethylindium (TMI) for Indium, SiH_4 Silane for Silicon, AsH_3 Arsine for Arsenic and $Zn(C_2H_5)_2$ Diethylzinc (DEZ) for Zinc.[51] The main advantages of MOCVD are its operation at nearly atmospheric pressure, the high growth rates (compared to MBE). With very good gas

flow control and regular monitoring, an accuracy comparable with MBE can be achieved on much larger zones. In low-pressure MOCVD, the growth chamber pressure is kept low, leading to a slower growth rate as with MBE.

3.1.5 Wafer Bonding

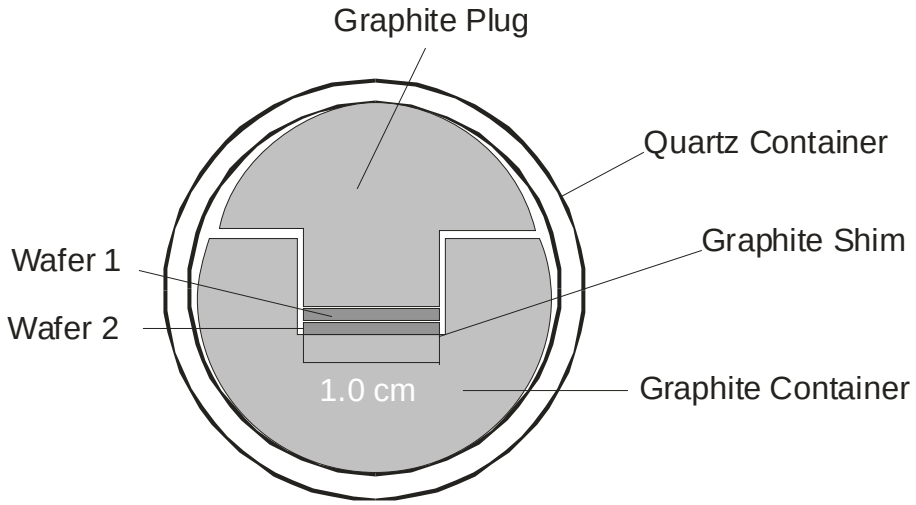

Figure 29. A schematic diagram of a wafer bonding reactor.

Wafer bonding is a method of fusing two semiconductor materials at the atomic level. The method is especially useful in bonding materials such as GaAs and InP which have different lattice constants.[73] (Approx. 5.8 Å for InP compared to approx. 5.6 Å for GaAs/AlAs.) This technique has been successful in creating long wavelength VCSELs with InGaAsP active regions and InP cladding layers bonded to GaAs/AlAs DBRs.[74,75,76] The difference in refractive index of InP and InGaAsP, used is in epitaxial DBR mirrors is very small. At least 30-periods are required to achieve the desired reflectivity.[77] GaAs/AlAs has a greater contrast in refractive index, therefore fewer periods are required to achieve the same reflectivity. Figure 29 shows a schematic diagram of the wafer fusion reactor.

The wafers to be fused are placed within the quartz reactor. When heated, the difference in the thermal expansion coefficients of the graphite and the quartz reactor cause the wafers to be compressed together. For successful fusion to occur, the wafers must be optically flat and free of contaminants. VCSELs created with this method showed normal device operation characteristics indicating the integrity of the fusion boundary.

3.2 Device Fabrication Processes

The fabrication of VCSELs demands a number of additional processes take place before the final device is complete. These processes include: masking of contacts, photolithography, etching, metalisation and re-growth.

3.2.1 Lithography

Masks are created to define areas that will be protected or removed during the lithography stage. Photoresist is spin-coated onto the semiconductor wafer. A photoresist is a light-sensitive material that on exposure to ultra-violet light causes it to undergo a chemical reaction. This is similar to the action of light on a photographic film. The photoresist is developed creating an image of the mask. An etchant will selectively etch away the material not protected by the photoresist. There are two types of photoresist that react in differently on exposure to ultra-violet light. If the photo-resist hardens on exposure to the light, when the excess resist is removed a negative copy of the mask is left behind and hence it is known as a negative photo-resist. Positive resists are designed to degrade on exposure to light. When developed, the resist is deposited in those areas where the light did not expose the resist, resulting in a positive copy of the mask.

For VCSELs, the typical dimensions of the contacts are suitable for ultra-violet light lithography to be used. The smaller features such as those found in integrated circuits require smaller wavelengths of light to be used. As more complex circuits are packed into a smaller space, the feature resolution is limited by the wavelength of the light used to expose the photoresist. This demands the use of techniques such as electron-beam lithography or x-ray lithography.

3.2.2 Metalisation

There are three techniques that are commonly used to create contacts: thin-film vacuum evaporation, sputtering and electroplating. With vacuum evaporation, the device is suspended above a Tungsten or Molybdenum boat containing the metal to be deposited on to the surface of the device. The boat is heated either by applying a current through it or by electron bombardment, vaporising the metal within the boat. Within the vacuum, atoms of the metal are emitted from the surface and travel in all directions, condensing on the inside of the bell-jar. A mask is used to control the geometry of the evaporated film on the device.

Sputtering also takes place within a bell-jar. The bell-jar is evacuated and an inert gas such as Argon is bled into the jar keeping a background pressure of 10^{-2} Torr. The material to be deposited onto the surface acts as the cathode. When a high-voltage of 2-6 kV is applied, the gas is ionised and the positive ions are accelerated to the cathode. The ions have sufficient energy to eject atoms of the cathode material. The mean free path of the atoms is long enough under the conditions of vacuum within the bell-jar to eventually coat the surface of the semiconductor.

Electroplating has the material to be plated acting as a cathode, submerged in an aqueous solution of metal salts. A potential difference is applied across the cathode and anode causes the metal to decompose coating the substrate. Electroplating is more simple and cheaper than evaporation or sputtering. However, the resulting metallic coating is difficult to control in thickness, less pure than either evaporation or sputtering and with surface topography that is relatively poor.

3.2.3 Etching

Etching may be required in the fabrication of VCSELs, for example to create the mesa structure of an air post VCSELs or in creating areas for re-growth for current blocking layers. The most common method of etching material is chemical etching. Table 6 lists some chemical etchants, the materials they are designed to etch and the rate of etch.

Etchant and ratio of mixture	**Material Etched**	**Approx. etch rate μm per min at 20°C**
HCl (conc.)	InP	5-15
HCl (conc.)	Surface oxide on GaAs	Fast
HCl (conc.)	InGaAs	<0.02
HCl:$H_2$0 (2:1)	InP	8
HCl:H_2O (1:1)	InP	0.7
HCl:H_2O (1:2)	InP	0.09
H_3PO_4:HCl (1:1)	InP	2.5
H_3PO_4:HCl (1:2)	InP	4.8
H_3PO_4:HCl (1:3)	InP	6.6
H_3PO_4:HCl (3:1)	InP	0.75
H_3PO_4:H_2O_2:H2O (3:4:3)	GaAs	6

$H_2O:NH_4OH:H_2O_2$ (20:2:1)	GaAs	0.5
$HBr:CH_3COOH:K_2Cr_2O_7$ (1:1:1)	Most III-V compounds	2-5
$H_2O_2:NH_4OH:H_2O$ (0.7:2:100)	GaAs	0.1
$H_2SO_4:H_2O_2:H_20$ (1:8:80)	InGaAs or AlGaAs	0.5
$Br:CH_3OH$ (1:100)	Most III-Vs	1-10
$HCl:H_2O_2:H_2O$ (80:4:1)	GaAs	1

Table 6 Common etchants for various semiconductor materials and etch rates. [78]

The etching rate is also affected by the plane of atoms that is presented to the etchant. A {111} plane of atoms is more closely packed than a {100} plane, leading to a slower etch rate. The atomic plane can also affect the shape of etch produced. Etching {100} planes leads to pyramidal holes in Si. [79] Other forms of etching including: ion etching, plasma etching and reactive plasma etching.

3.3 I-V Characteristics

We characterised all the VCSELs investigated by measuring the current voltage curve. The device to be tested is electrically pumped using an Avtec (AVR-3-PW-C) pulse generator. The pulses were kept short enough and at a frequency that will not cause an adverse amount of heating in the active region of the device. In our experiments, we used pulses with a pulse-width of 200 ns and a repetition rate of 1 kHz. This gives a duty cycle of 0.02 %.

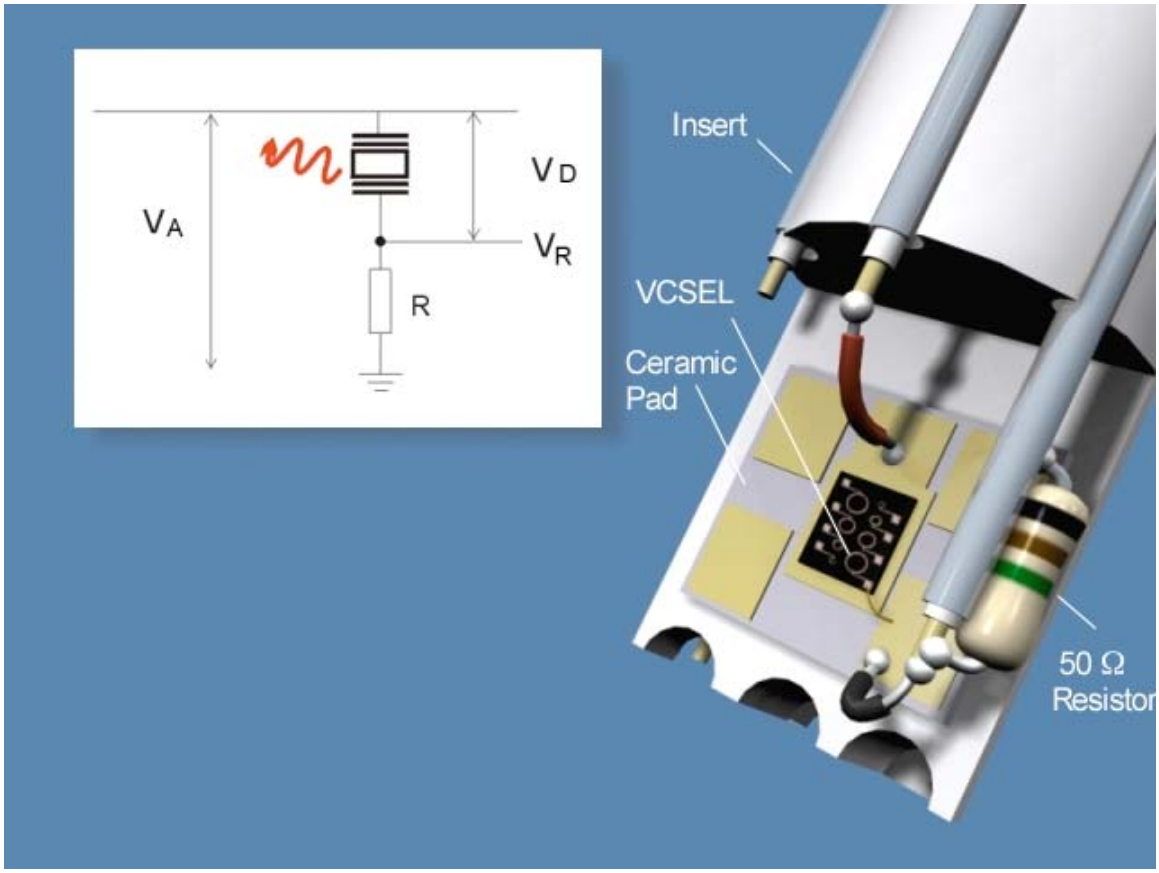

Figure 30 diagram showing the VCSEL mounted for testing in the cryostat and the circuit used to read voltages flowing through the VCSEL and 50 Ω resistor.

Figure 30 shows the circuit used to obtain the I-V characteristic of the laser under test. A 50 Ω resistor is placed in series with the laser. The applied voltage V_A and the voltage drop across the 50 Ω resistor are recorded using the 50 Ω input of a Tektronix 4907, high-speed oscilloscope.

The voltage drop across the VCSEL (V_D) is then:

$$V_D = V_A - V_R \quad \textbf{(78)}$$

The current flowing through the laser is:

$$I_D = V_D / R_{eff} \quad \textbf{(79)}$$

where

$$R_{eff} = 25\Omega \quad \left(\frac{1}{R_{eff}} = \frac{1}{R} + \frac{1}{Z_{in(scope)}} \right) \quad \textbf{(80)}$$

The I-V plot can be calculated over a range of applied voltage values. A typical plot for one of the GaAs VCSELs investigated is shown in Figure 31.

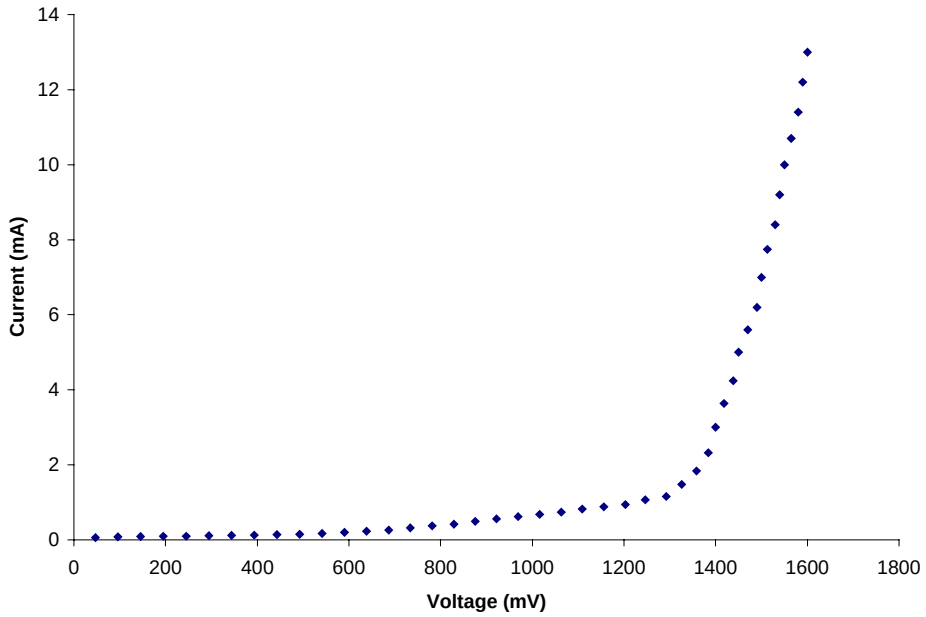

Figure 31. I-V characteristic of an A5 MQW GaAs VCSEL with 100 μm window diameter at 290K.

The I-V characteristic shows the variation of current flowing though the laser with applied voltage. This I-V characteristic has a typical form of a laser diode, with two distinct regimes. At low voltages, little current flows. Energy is required to overcome the

resistance of the DBRs and alter the band profile of the junction before the carriers can flow freely into the quantum wells. At the threshold voltage, the slope of the curve, increases sharply. A small increment in the applied voltage leads to a larger increment in the current. At this point, the band-edge diagram is close to the flat-band condition and carriers are being injected into the active region.

3.4 L-I Characteristics

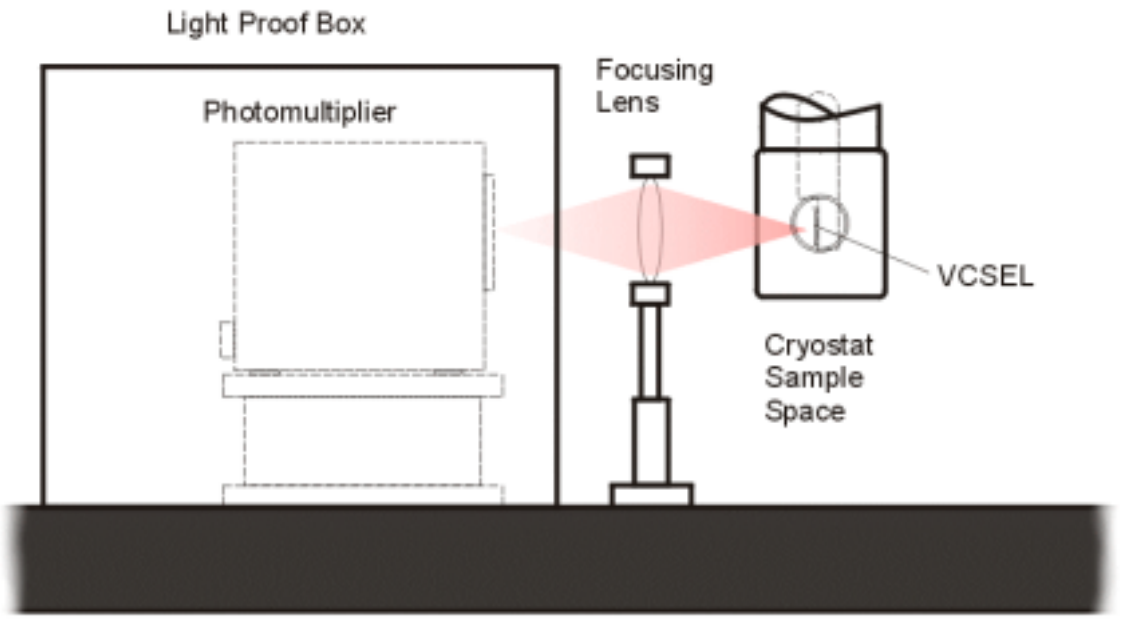

Figure 32. Arrangement of device, focusing lens and photomultiplier for gathering L-I characteristics.

L-I characteristics (light-output against current) are used in conjunction with I-V characteristics to determine the threshold current for a semiconductor laser. At low currents, any emission from the laser is from spontaneous emission. As the current is increased, more carriers are injected into the active region. When the gain in the device is equal to the losses, the device has reached threshold or transparency. Further increase in

current leads to a greater proportion of stimulated emission and lasing. Beyond the threshold current a small increase in current leads to an exponential increase in the light output, with stimulated emission dominating. In our experiment, the light from the VCSEL was directed out of one of the windows in the cryostat. The divergent beam, is refocused onto the GaAs photocathode of a Hamamatsu (R493-02) photomultiplier tube, by a 50 mm diameter convex lens of 20 cm focal length. The output voltage from the photomultiplier is read from the 1 MΩ input of the oscilloscope, with a 50 Ω terminator bring the RC time constant of the pulse down.

The L-I characteristic in Figure 33 shows these two regimes clearly. The threshold current is determined by extrapolating a line from the points above threshold to through the x-axis. Threshold current occurs where the extrapolated line crosses the x-axis. The slope of the L-I curve in the linear region above threshold gives the slope efficiency of the device.

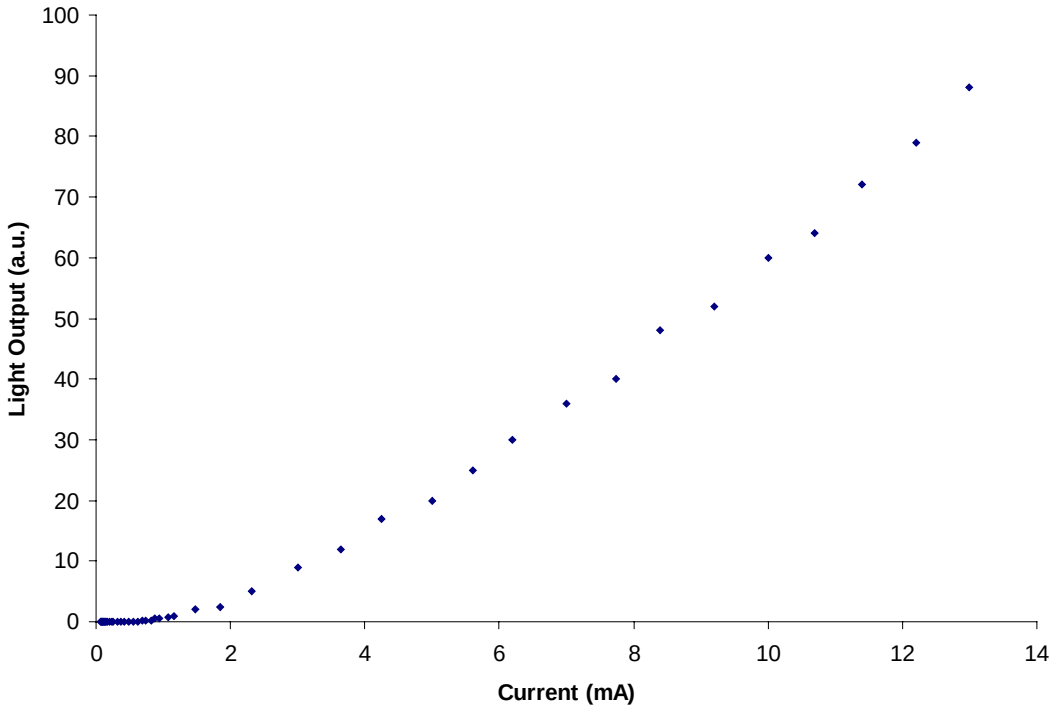

Figure 33 L-I characteristics for A5 100μm, GaAs MQW VCSEL at 290K.

3.5 Temperature Dependence of Threshold Current

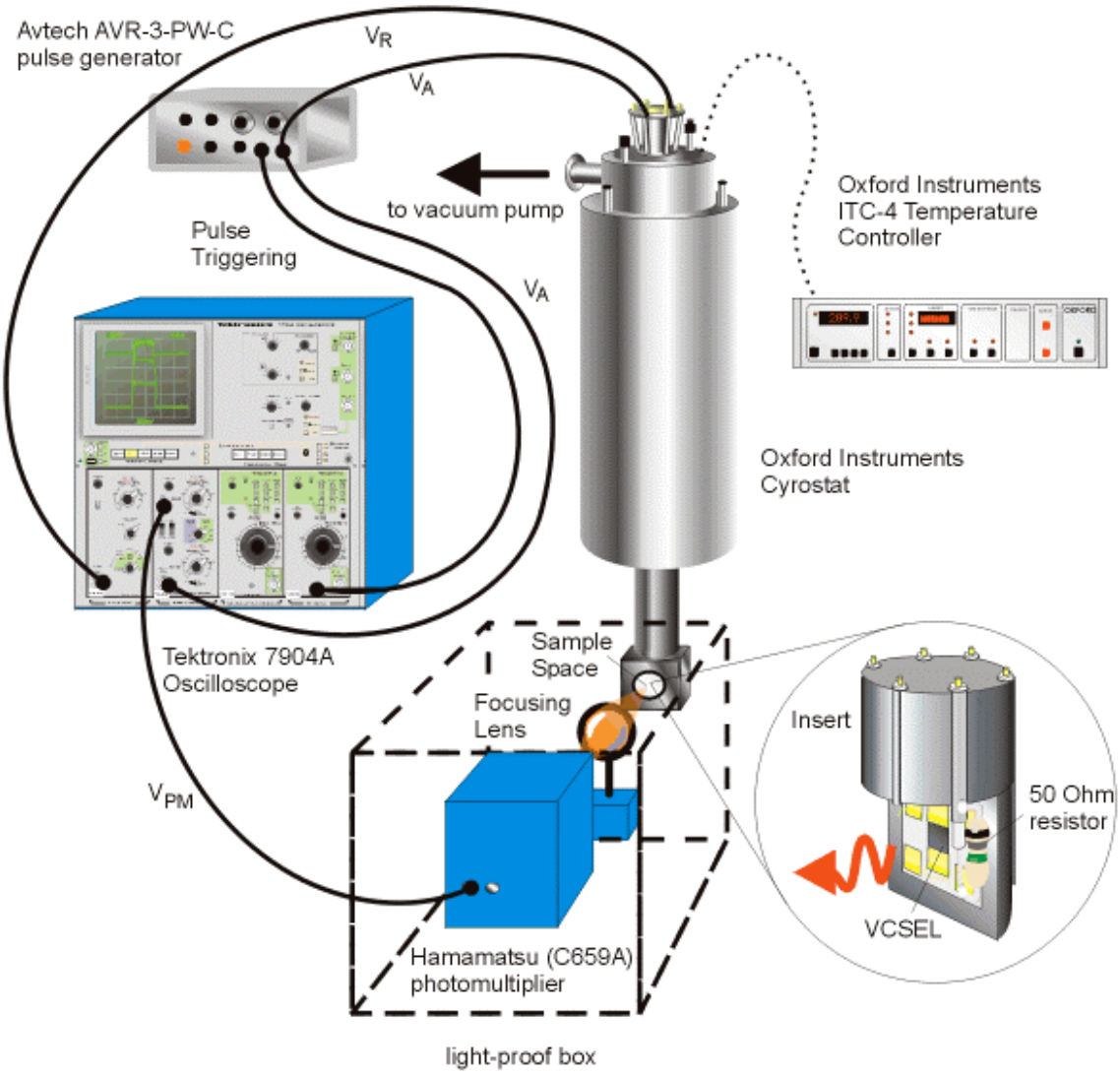

Figure 34. Apparatus used to measure temperature dependence of VCSELs. I-V characteristics and L-I characteristics can be obtained using this equipment over a range of 77-300 K.

Figure 34 shows a schematic diagram of the experimental set-up for measuring both I-V characteristics and L-I characteristics from 300 K down to 77K. The device is mounted onto an insert and placed within the Helium cryostat. The cryostat is designed to be used between 4 K<T< 300 K. The experiments reported here, however, the lowest temperature

was 77 K and this was achieved using Liquid-Nitrogen only. The temperature of the sample is regulated using a needle valve, to alter the flow of Liquid-Nitrogen into the sample space together with an Oxford Instruments ITC-4 temperature controller. Electrical connections were made using rigid coaxial cables and SMA connectors, readings were made using a Tektronix Model 7904A oscilloscope. At the required temperature, pulses from an Avtec (AVR-3-PW-C) pulse-generator at a low duty cycle to prevent the device from excessive heating, were used to excite the device. The voltages were noted and I-V characteristics calculated as outlined in the previous section. To obtain L-I measurements, light emitted from the VCSEL was focused by a convex lens onto the window of a water-cooled, Hamamatsu (R943-02), GaAs photomultiplier tube for GaAs based VCSELs, while a Newport Germanium (818-IR) APD was used for InGaAsP based VCSELs using the kit described in Section 3.6. This was also connected to the oscilloscope and the output-voltage recorded.

3.6 Temperature Dependent Photoluminescence

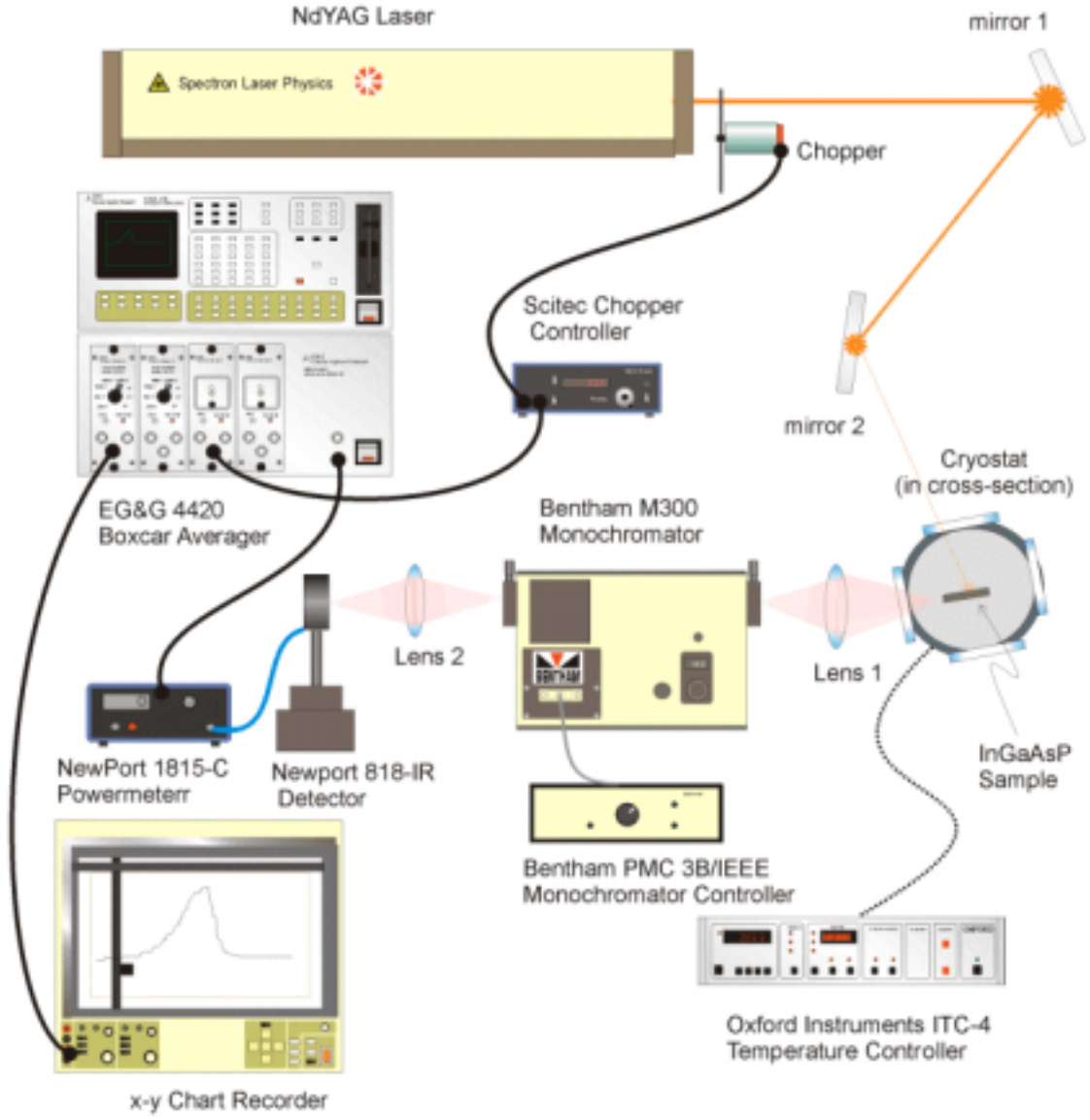

Figure 35. Experimental apparatus for studying the temperature dependent photoluminescence of InGaAsP/InP material systems. The sample is optically-pumped by a NdYAG laser. The resulting emission is spectrally sampled using a monochromator and the intensity is recorded using a power-meter and boxcar-averager.

The photoluminescence experiments for the InGaAsP/InP material system took place using the experimental set-up in Figure 35. The sample is mounted in the cryostat and can be maintained at a predetermined temperature between room temperature and approximately 110 K using liquid-Nitrogen and controlled using an Oxford-Instruments intelligent temperature controller, ITC-4. During measurements, samples are optically pumped using a NdYAG laser line at λ=1064 nm. The wavelength of the optical excitation was shorter than the critical wavelength for Inter-Valence Band Absorption (IVBA) in the InGaAsP system. As the photo-generated electron-hole pairs recombine (spontaneous emission), they emit photons. The light is focused into a Bentham M300 1/3m monochromator to select a wavelength to be detected by a Newport Germanium detector (818-IR) The signal from the detector is passed into an EG&E 4420 and 4422 boxcar-averager system that averages the signal and sends the value to an x-y chart recorder. Experimental measurements were carried out at wavelengths between λ=1340 nm and1640 nm and the results recorded at a range of different temperatures and pump (excitations) powers.

3.7 Fibre Coupling to VCSELs

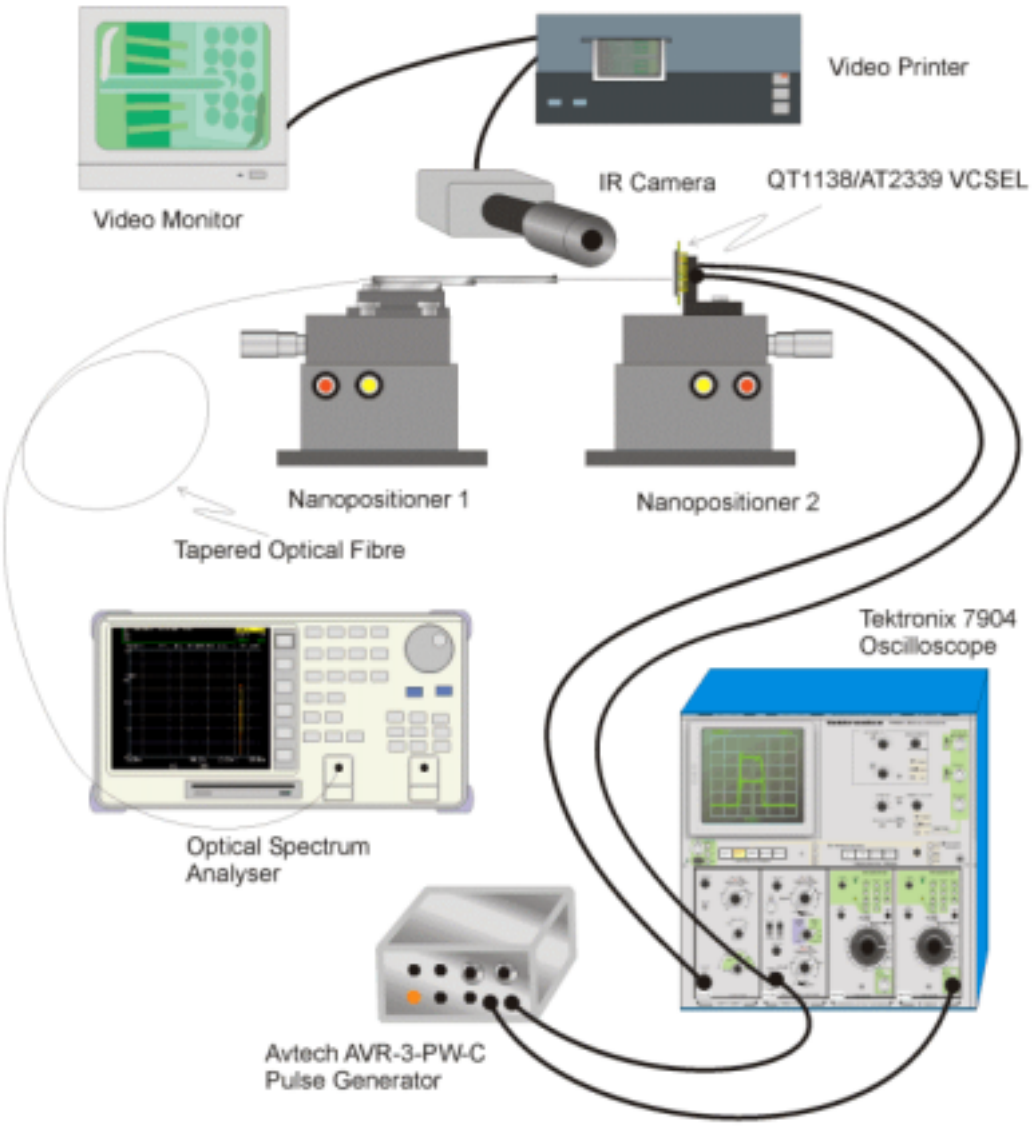

Figure 36. Alignment of optical fibre with a VCSEL.

The purpose of this experiment is to analyse the emission spectrum of the VCSEL. This experiment was performed on GaAs QT1138 samples and also InGaAsP AT2339. The device and fibre are mounted on separate nano-positioning stages. The position in the x, y and z-planes of the fibre are minutely altered until the fibre is directly over the VCSEL connected. This is a delicate procedure and to aid the positioning, an IR camera and

highly magnifying lens image the VCSELs and the end of the fibre. When the fibre is close to the VCSEL surface, a laser pointer is shone down the fibre and a faint reflection can be seen on the surface of the wafer. Another aid to locate the connected VCSEL was a second dc power supply which was adjusted until the device just emitted light visible on the camera and then turned off to avoid over heating the device. When satisfactory alignment was achieved, the single VCSEL is pulsed using a duty cycle of 0.02%, with a pulse-width of 200 ns and a repetition rate of 1 kHz using the pulse generator. The current and voltage are displayed on the oscilloscope. The optical spectrum analyser is set to scan from 700-900 nm in the case of the QT1138 GaAs VCSEL and from 1300–1600 nm for the InGaAsP VCSELs. A normal optical fibre has a numerical aperture that is too small gather much light from the device, therefore a tapered fibre is used to collect as much of the emitted light as possible. An interesting technique for producing a rudimentary tapered fibre, was to use a fibre fusion splicing machine to pass a controlled arc of electricity over the end of the fibre causing the glass to melt and reform as small spherical bead on the end of the fibre.

4. Results and Discussion

4.1 GaAs VCSELs

In order to develop and test our model for the temperature dependent operation of VCSELs for InGaAsP/InP material systems we initially investigated GaAs/AlGaAs material system with better established characteristics and more reliable DBRs.

4.1.1 Device Structure

The structure of VCSELs, supplied by DERA, under the code A5, is shown in Figure 37. These devices have a graded index, multi-quantum well active region with three GaAs quantum wells of width 60 Å separated by 80 Å barriers of $Al_{0.3}Ga_{0.7}As$, in the centre of the 3λ/2. cavity. The top DBR is built up from the repetition of a single unit consisting of {AlAs, $Al_{0.12\text{-}1.0}Ga_{0.88\text{-}0.0}As$, $Al_{0.12}Ga_{0.88}As$, $Al_{1.0\text{-}0.12}Ga_{0.0\text{-}0.88}As$} with 19 repeats. Four layers per period and grading within layers aid to reduce the electrical resistance across the DBR. The repeat period for the bottom DBR also created from four layers,{$Al_{1.0\text{-}0.12}Ga_{0.0\text{-}0.88}As$, $Al_{0.12}Ga_{0.88}As$, AlAs, $Al_{0.12\text{-}1.0}Ga_{0.88\text{-}0.0}As$} with 30 repeats. Therefore, emission is from the top surface, through a etched circular mesa of either, 100 μm, 70μm, 50μm or 10μm, diameter. The VCSELs were supplied on a single chip, with two devices of each size on the wafer.

The second GaAs VCSEL investigated was grown at Sheffield University with the batch number QT1138. This VCSEL is also a top emitting, air post, mesa structure design,

with a top Ti-Au ring-contact and a circular emission window of 8 μm. The internal layer structure of the is shown schematically in Figure 38. Starting at the top of the device, the top DBR consists of 27 periods of p-doped, {$Al_{0.2}Ga_{0.8}As$, $Al_{0.5}Ga_{0.5}As$, $Al_{0.78}Ga_{0.22}As$, $Al_{0.5}Ga_{0.5}As$}. The cavity has 3-GaAs 100 Å quantum wells separated by 100 Å barrier layers. The multi-quantum well structure is grown to interact with an anti-node of the resonant mode. The bottom DBR structure has two sets of n-doped periodic layers, the first set has 15 periods of {$Al_{0.2}Ga_{0.8}As$, $Al_{0.5}Ga_{0.5}As$, $Al_{0.78}Ga_{0.22}As$, $Al_{0.5}Ga_{0.5}As$} which is the same as in the top DBR. In addition, there is a second periodic structure with a higher refractive index contrast consisting of, 27 periods of {$Al_{0.2}Ga_{0.8}As$, $Al_{0.5}Ga_{0.5}As$, AlAs, $Al_{0.5}Ga_{0.5}As$}. These layers were grown using MOCVD on a GaAs substrate heavily n-doped to provide an Ohmic contact with the bottom TiAu contact.

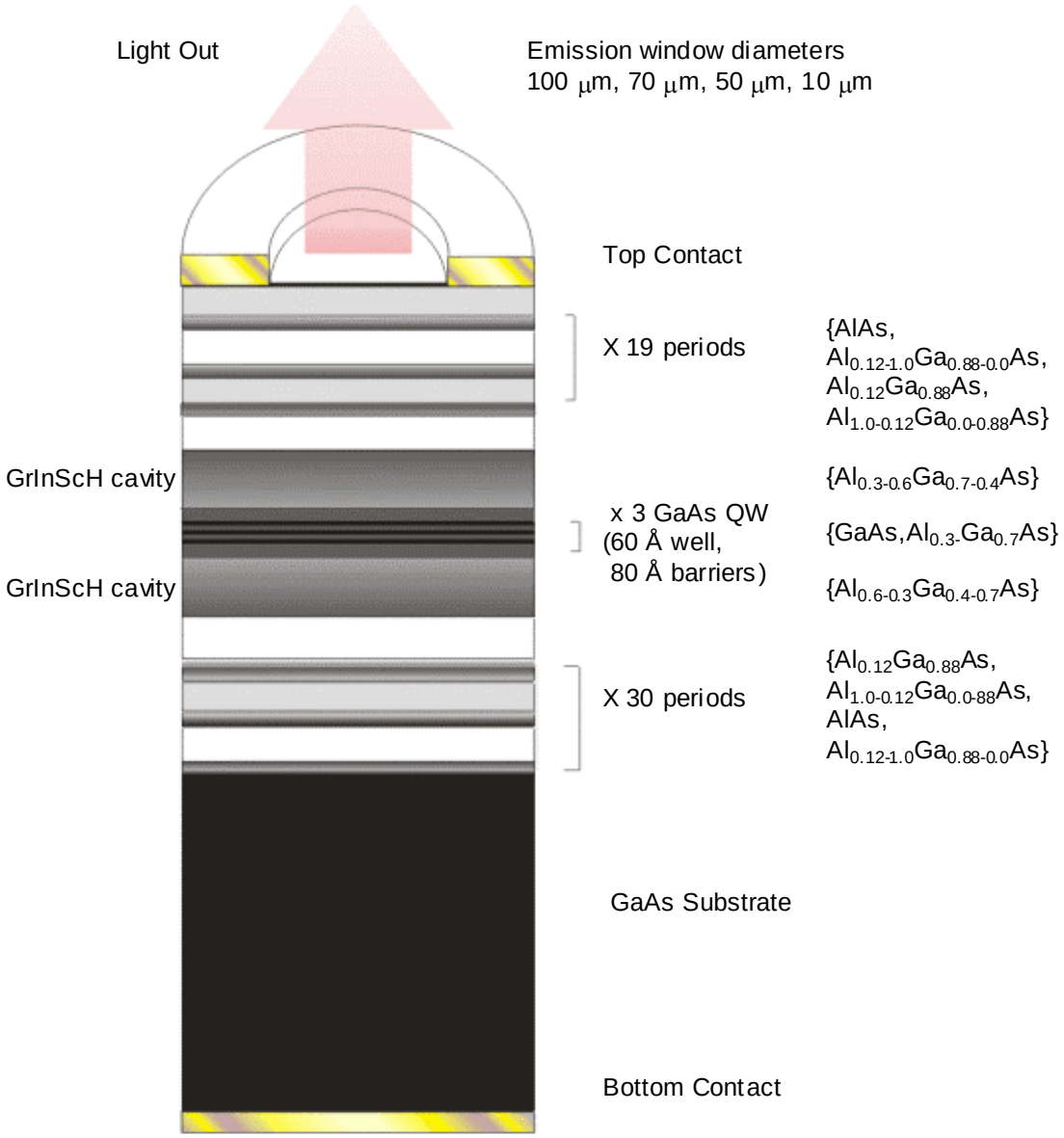

Figure 37: Schematic diagram of the A5 GaAs VCSEL samples.

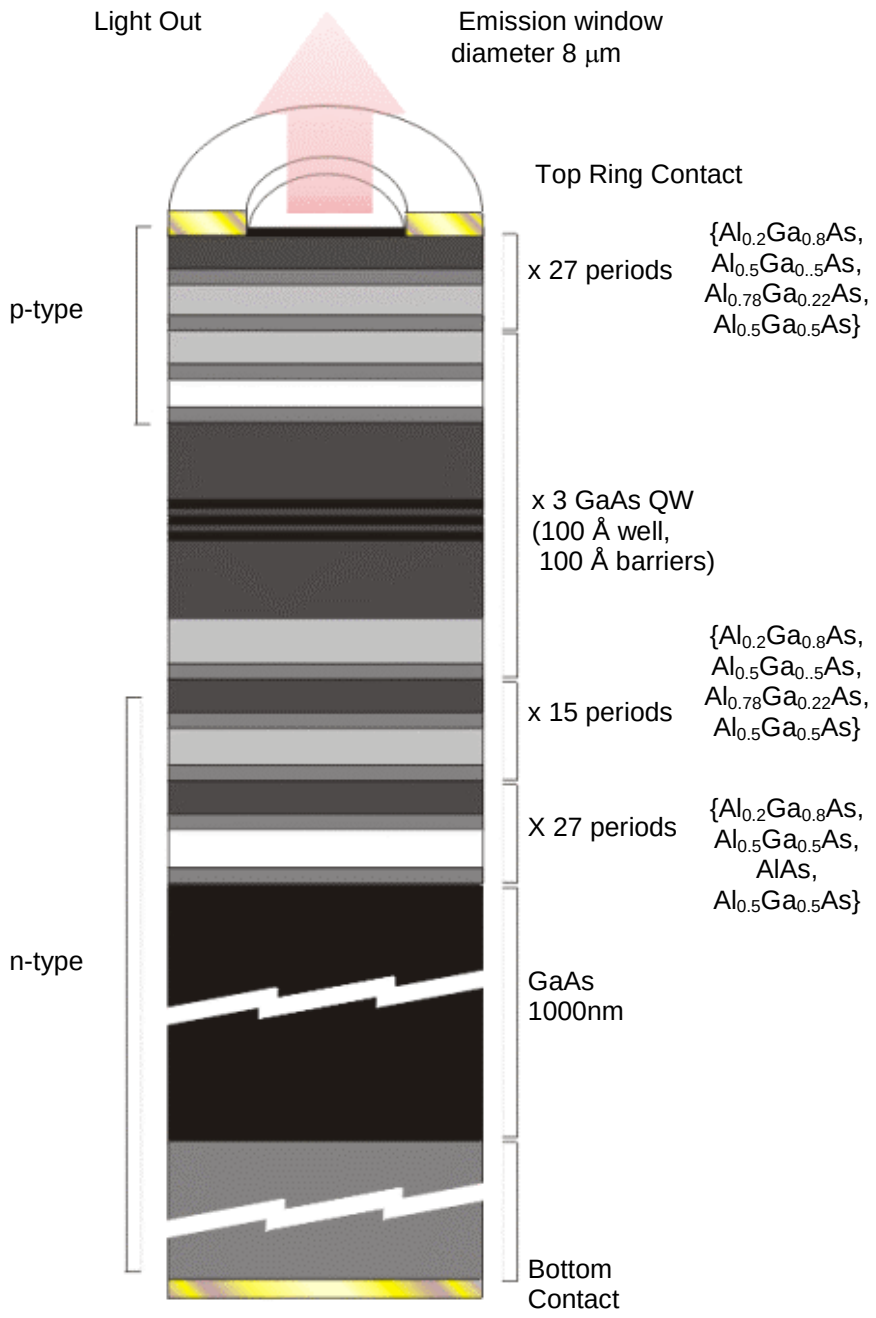

Figure 38. Schematic diagram of QT1138 VCSEL. Layers correct thickness scale and the degree of whiteness indicates Al fraction, i.e. white indicates AlAs while black indicates GaAs.

4.1.2 A5 VCSELs

The results showing the temperature dependence of the I-V characteristics and L-I characteristics are shown in Figure 39 and Figure 40 respectively.

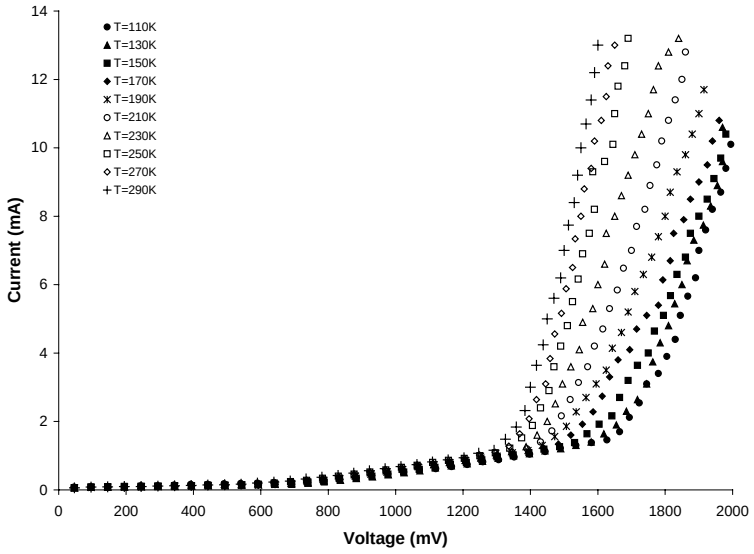

Figure 39: A5 100μm Combined I/V Plot for T=110K to T=290K

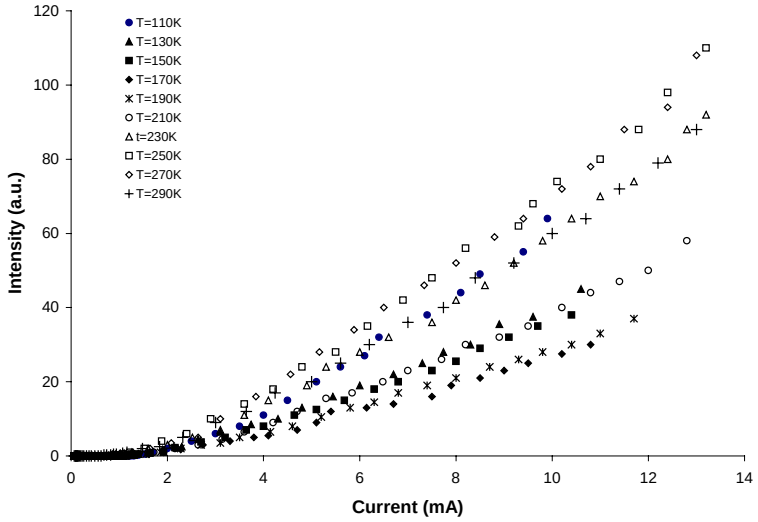

Figure 40: A5 100μm VCSEL Combined L-I Plot at T=110 K to T=290 K

The I-V characteristics of the VCSEL show the voltage at which the current starts to flow through the device increases with decreasing temperature. This follows the temperature dependence of the energy gap of the buffer layer. The L-I curve is determined not only by how many carriers are in the active region but also, primarily, on the relative positions of the cavity resonance and the gain peak.

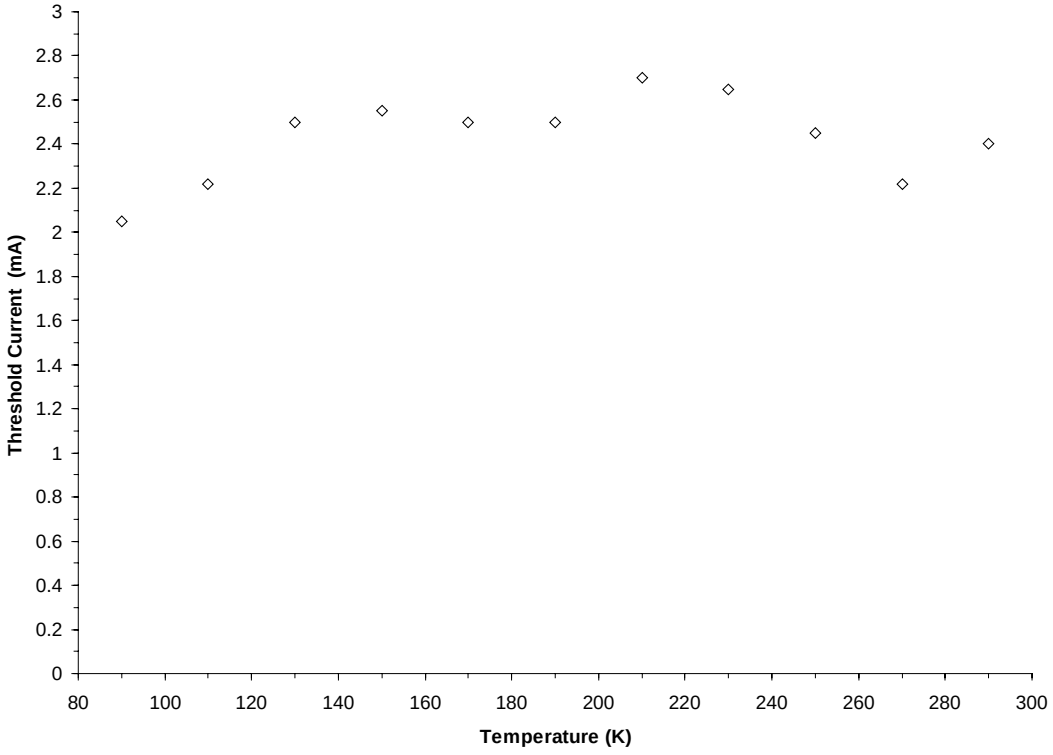

Figure 41. Threshold current against temperature for the 100 μm A5 VCSEL. A simple temperature dependence of threshold current is not easily discernible.

Figure 41 shows the temperature dependence of the threshold current obtained from Figure 40. The observed dependence is not a typical of the output for the threshold current against temperature, one would expect from a VCSEL. We can see that the temperature dependence is not simple. The emission from the cavity depends on the wavelength of single cavity mode Light is emitted from the portion of the gain spectrum that is at the

same wavelength as the cavity resonance. The shift in the emission spectrum is caused by the temperature dependence of the energy-gap, while the shift in the cavity resonance is largely governed by the change in the refractive index within the layers forming the DBRs. For an increase in temperature, both the emission spectrum and the cavity resonance are red-shifted. However, the cavity resonance red-shifts at a much slower rate. If the gain spectrum is blue-shifted with respect to the cavity resonance at lower temperatures, then the cavity resonance will encounter gain at the long-wavelength end of the emission spectrum. To reach threshold requires the injection of more carriers into the active region to overcome the losses within the cavity. Increasing the temperature red-shifts the emission spectrum still further and the cavity resonance will experience a higher amount of gain at the cavity resonant wavelength, reducing the current required to reach threshold. This will continue until the cavity resonance is over the gain peak. (At least, this is largely true for GaAs. We shall see later, for InGaAsP, this is not the whole story.) Further increasing the temperature, the cavity resonance begins to sample the tail-end of the emission spectrum. Once again the threshold current has to increase to overcome the loss. The overall effect is to produce a parabolic-like threshold current against temperature curve.

In the event of more than one cavity mode being present within the stop band, this will modify the threshold current temperature dependence. If the separation between the resonant modes is sufficient, then the temperature dependence of the threshold current could exhibit more than one parabolic curve. Additional cavity modes can be caused by the accumulation of small errors in the thickness of the layers, during the growth process. The temperature dependence of the threshold current shown in Figure 41 is indicative of

the existence of several parabolic temperature dependence curves and hence the presence of more than one cavity resonance. The gradient of the L-I curve, above threshold, is a measure of the slope efficiency of the device; greater values of the slope of the L-I curve imply an increase in the light output for the same increase in current. The slope of the L-I curve above threshold broadly follows an inverse proportionality with the temperature dependence of the threshold current. Where the L-I curve is steepest, the threshold current is lowest. A better example of the variation of the threshold current with temperature for a VCSELs is obtained for the A5 VCSEL with a 70 μm diameter window.

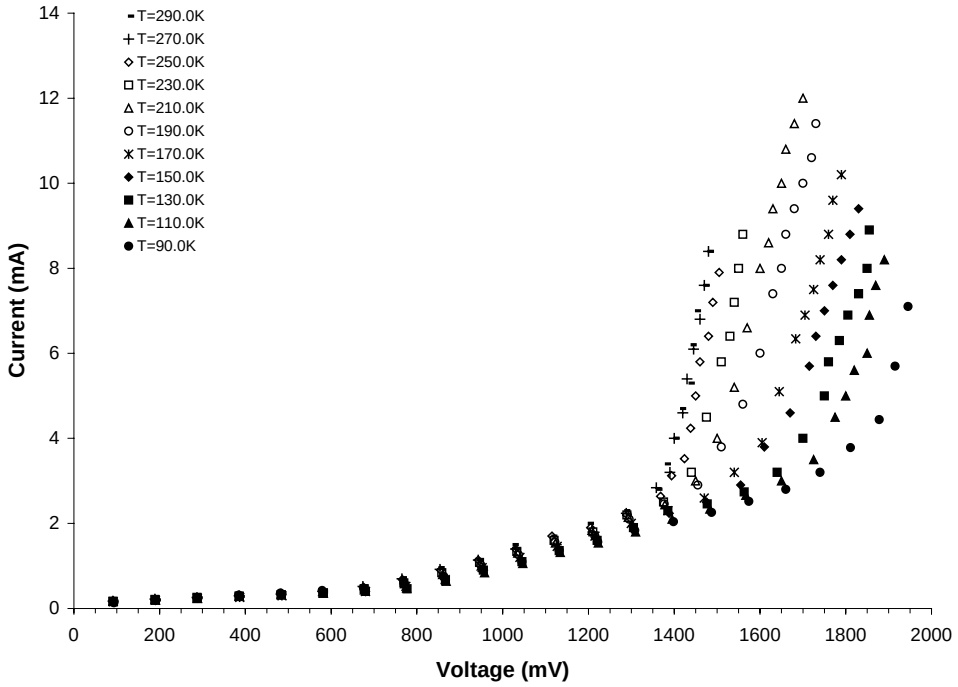

Figure 42. I-V characteristics for an A5 70 μm VCSEL over a temperature range T= 90 K -290 K.

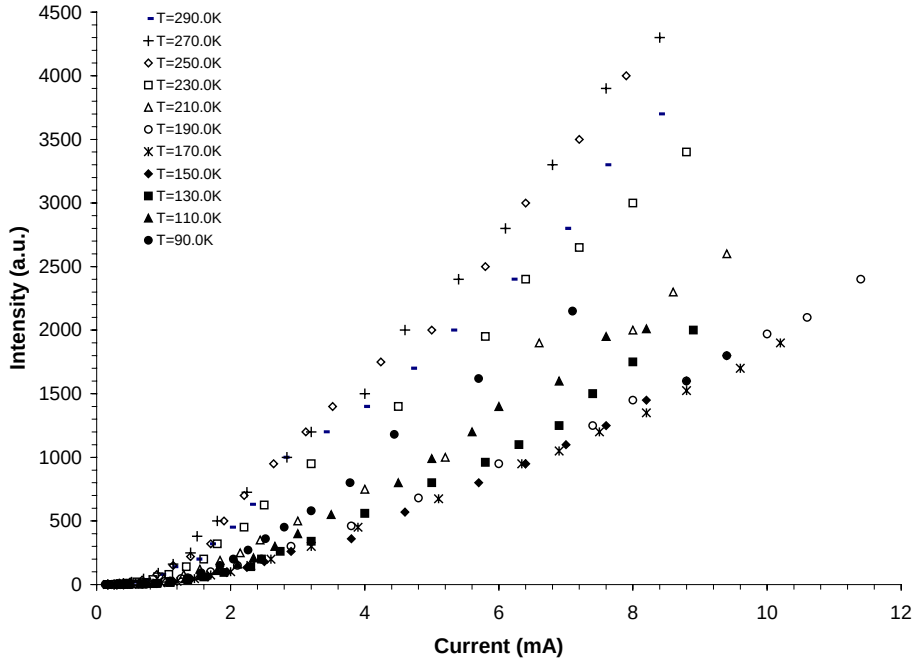

Figure 43. L-I characteristics for an A5 70 μm VCSEL from T=90 K – 290 K

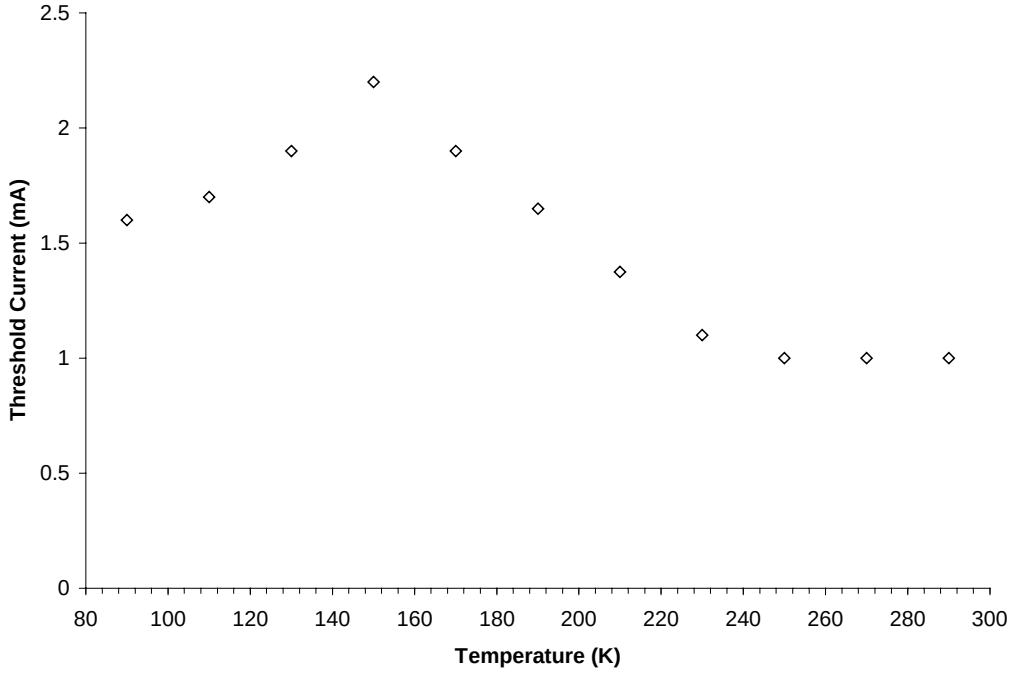

Figure 44. The threshold current against temperature for the A5 70 μm VCSEL

The threshold current against temperature plot (Figure 44) shows two distinct regions. The threshold current shows one half of a parabolic temperature dependence for temperatures above T=150K to T=290 K with a minimum threshold current of close to 1 mA occurring over a temperature range of T=250K to T=290 K. This device was designed to operate at room temperature, it is perhaps not surprising that the device exhibits its lowest threshold current close to room temperature. Below T=150 K, the threshold current starts to reduce again. from a peak of 2.25 mA. The second temperature dependence also seems to show the right-hand portion of a parabolic temperature dependence although its minimum may occur below T=90 K.

It is useful to calculate the emission wavelength of the device and the position of the cavity resonance to examine the how well the two coincide, since only light at the cavity resonance wavelength will be emitted strongly. Most of the radiative transitions occur from the first energy level in the conduction band to the first energy level in the heavy-hole valence band. The number of energy levels and their separation within the quantum well are determined by the well width. Using the finite barrier calculation, outlined in Section 2.6.7, we can calculate the wavelength for transitions from the first conduction band to the first heavy-hole valence band.

	CC	HH
m_b mass in barrier layer	0.0056 m_0	0.34 m_0
M_w mass in well	0.0916 m_0	0.466 m_0
V_0 (barrier height)	250.6 meV	123.5 meV
L_z	60 Å	60 Å

Table 7. Parameters used in the calculation of the energy levels within the quantum well.

The total transition energy is then the sum of the energy-gap, energy of the first energy level in the conduction band and the first energy level in the heavy-hole valence band. These were 1.424 eV, 30.7 meV, 7.4meV, respectively.

$$\lambda = \frac{1.24}{1.462} = 848\ nm \qquad \textbf{(81)}$$

To find the position of the cavity resonance, the reflectivity spectrum is calculated using the transmission matrix method. (Section 2.5.1.) The A5 VCSEL structure has a number of layers that have a graded refractive index. The refractive index for these layers was taken as the average refractive over the graded layer Figure 45 shows the calculated reflectivity spectrum using parameters provided by the growers. The spectrum shows a strong cavity resonance at a wavelength of 845 nm. A slight dip in the reflectivity spectrum at 805 nm is also apparent.

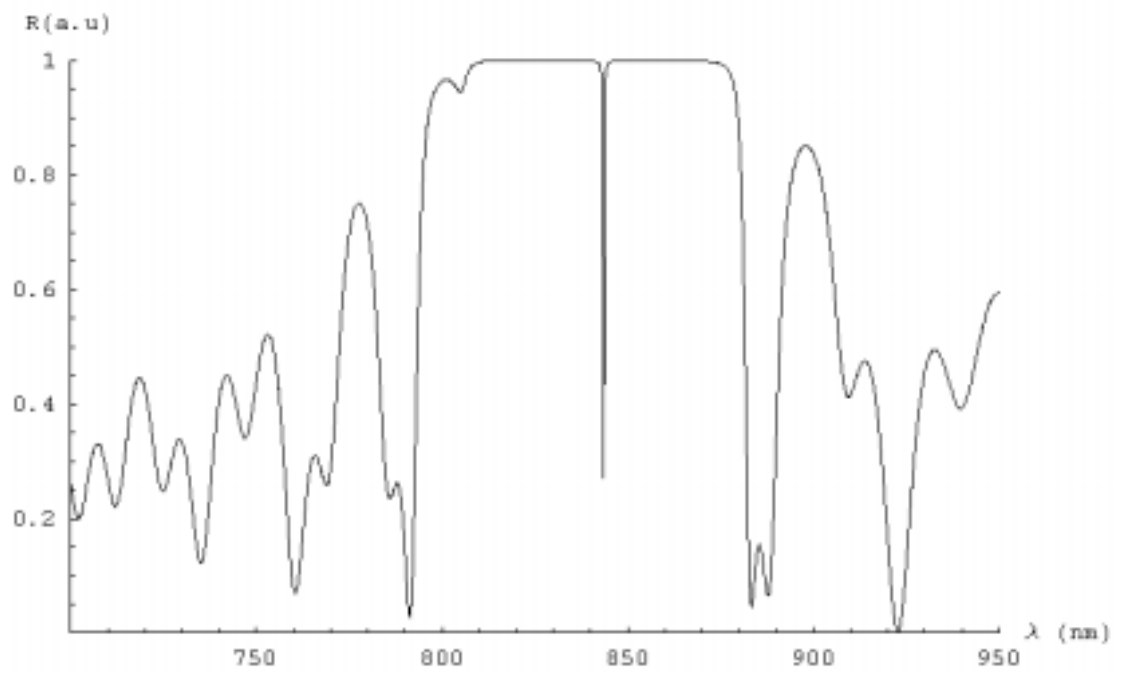

Figure 45. Reflectivity Profile of the A5 structure calculated from the growth sheet without any change in the layer structure.

We are now in a position to explain the temperature dependence of the threshold current. As the temperature of the VCSEL increases, the energy gap of the semiconductor decreases and the transitions from the conduction-band to valence-band produce photons with a longer wavelength. A second effect of increasing temperature is to increases the refractive index of the layers of semiconductor. This has a marked effect in the many layers forming the DBRs, since the cavity resonance is determined by the effective thickness of the layers within the device, an increase in the refractive index causes the cavity resonant wavelength to be red-shifted. The rate of change of the energy gap shift is material dependent. For GaAs, a red-shift of 0.32-0.33 nmK^{-1} has been observed by many authors.[80,81,82,83] The red-shift in the cavity resonance is much slower, at between 0.06-0.09 nmK^{-1}. [84, 85, 86, 87,88, 89, 90, 91, 92]

At room temperature, the e_1-hh_1 transition is calculated at 848 nm and the cavity resonance 845 nm. Decreasing the temperature has both the gain spectrum and cavity resonance shifting to shorter wavelengths. The net effect is a blue-shift of the gain spectrum with respect to the cavity resonance. When there is a high level of gain under the cavity resonance, the threshold current is reduced. Although much of the gain comes from transitions from the conduction band to the heavy-hole valence band, there are contributions to the gain from the conduction band to the light-hole band at high carrier injection. If these transitions are present, then they will also contribute to the intensity of the light received by the photomultiplier.

From Figure 45, the difference in the wavelength between the two 'cavity-modes' is 40 nm. Assuming the cavity modes and the emission spectrum are coincident, as the temperature is reduced, the gain spectrum will blue-shifted at around 0.32 nmK^{-1}. At the same time the cavity resonance and the whole reflectivity spectrum will blue shifted at around 0.09 nmK^{-1}. The gain spectrum peak moves away from the first cavity resonance at 845 nm to the shorter-wavelength 'cavity resonance' at 805 nm. The relative motion of the gain spectrum to the cavity resonance is about 0.23 nmK^{-1}. The temperature drop required for the gain spectrum to travel 40nm is, 40 nm/0.23 nmK^{-1} = 173 K below the 290 K we started at, which gives the second minimum at 117 K. This is not too far away from where the second minimum in the threshold current occurs.

To see the effect of random errors introduced into the structure on the cavity resonance, the reflectivity spectrum was calculated with the inclusion of a random error of up to ± 4 monolayers in the thickness of all layers. The presence of carbon as a dopant, implies that these devices was grown using MOCVD. The nature of the gas-flow process leads to

variation in the thickness of the deposited layers depending on the position of the wafer. If not carefully monitored. However, even with MBE there can be variation, in the thickness of the layers, as one layer is not completely filled with atoms before the next begins to assemble. These effects were found in other devices, such as the HELLISH VCSELs [93,94], modelled and verified by experimental reflectivity. Non-uniformity that exists within the structure can also lead to more than one cavity resonance.

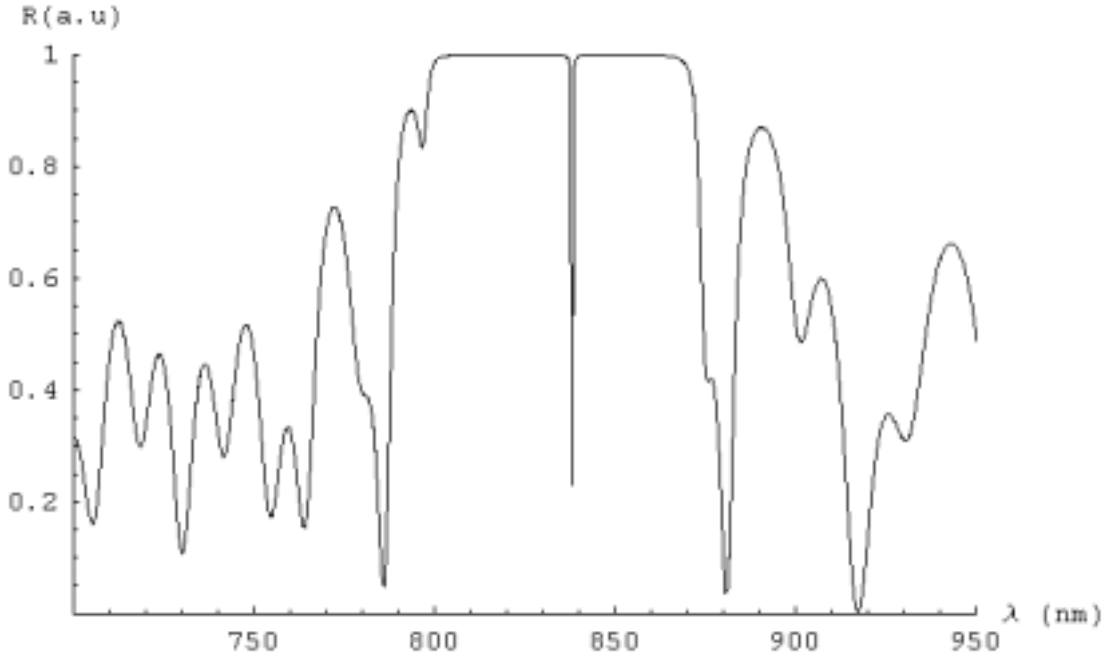

Figure 46. Reflectivity spectrum for the A5 VCSEL with random errors of ± 4 monolayers growth to each layer. The effect is to introduce a second mode into the stop-band. In this case, the strongly defined cavity resonance is marginally blue-shifted although the separation between the cavity resonance remains roughly the same.

The effect of the second resonance may be stronger than in the calculated spectrum because of the variation in the layer structure across the area of the wafer, however the threshold current at room temperature is at a minimum suggesting the cavity resonance and gain peak are coincidental.

The second cavity resonance appears to be an artefact of the number of periods in the bottom DBR as can be seen by increasing the number of layers in the bottom DBR. Starting with 10 periods in the bottom DBR the second cavity dip is not apparent. With 20 layers we can see a shoulder developing at the blue edge of the stop-band. With 25 layers the second cavity resonance is nearly fully incorporated into the stopband and with 30 periods in the top DBR the second cavity resonance is as described in the reflectivity spectrum of the VCSEL. With an even greater number of layers in the bottom DBR we can see the development of even a third potential cavity resonance.

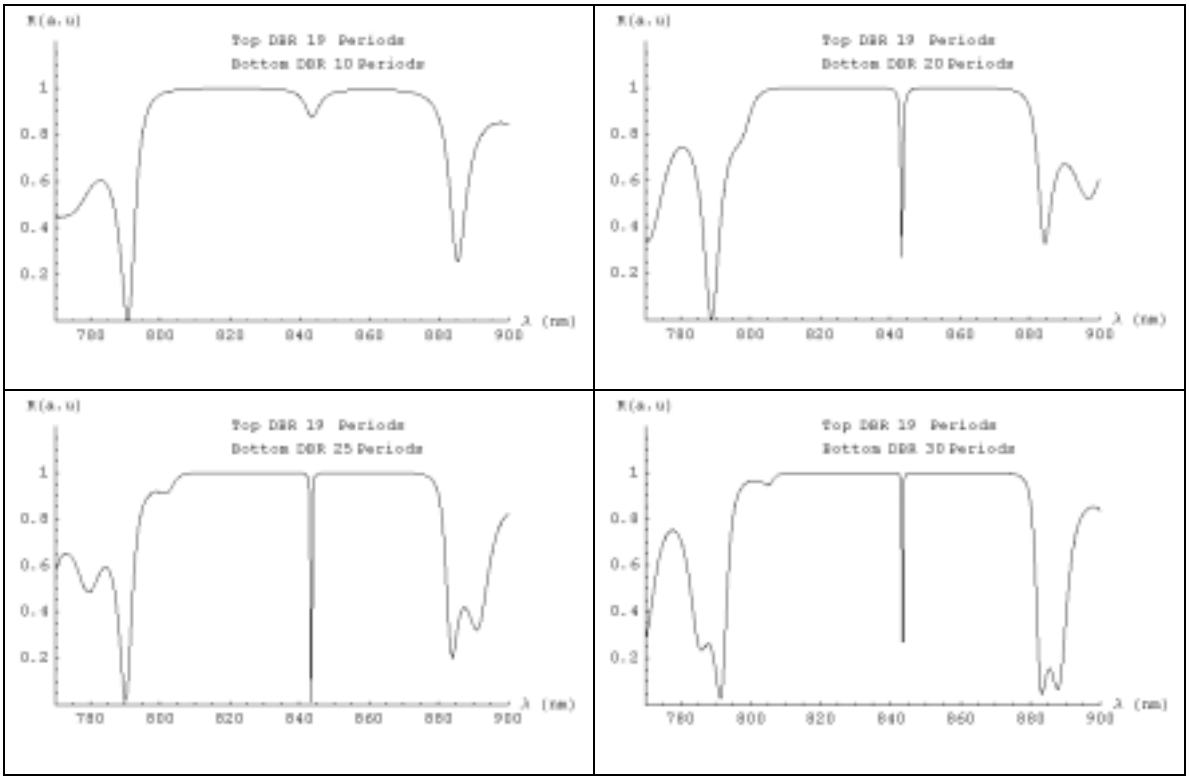

Figure 47. Calculated reflectivity spectra of A5 VCSEL with increasing number of periods in the bottom DBR. a) 10 Periods, b) 20 Periods, c) 25 Periods and d) 30 Periods.

Unfortunately, the other VCSELs were destroyed when our laboratory was relocated and so there is no data for 50 μm or 10 μm.

4.1.3 QT1138 Results

The I-V and L-I results are shown below in Figure 48 and Figure 49

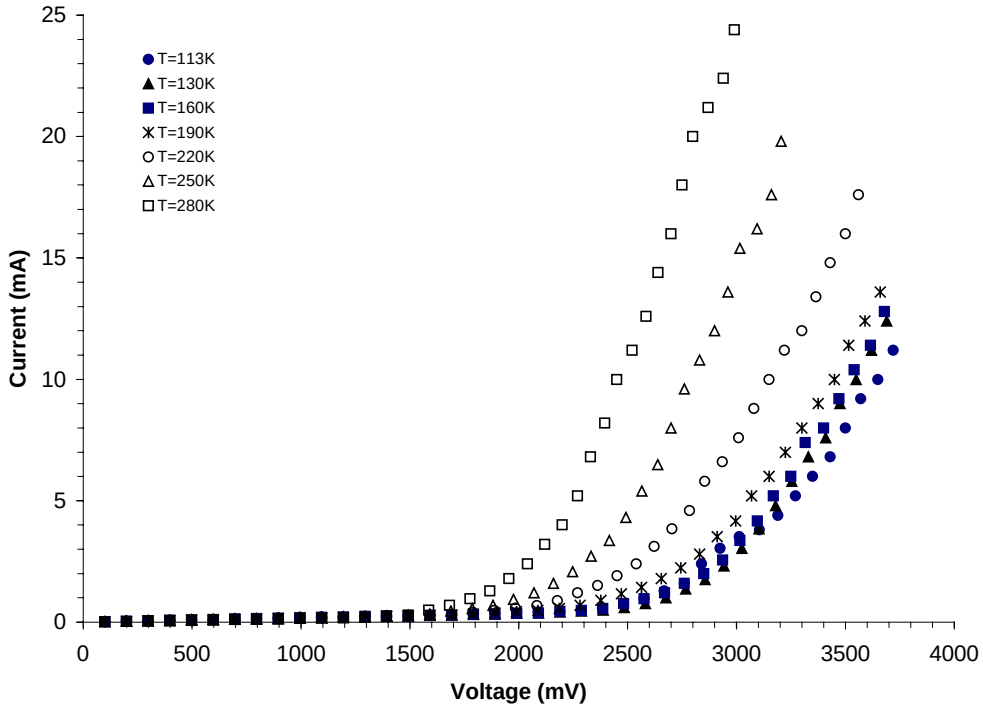

Figure 48. I-V Characteristics of QT1138, GaAs VCSEL.

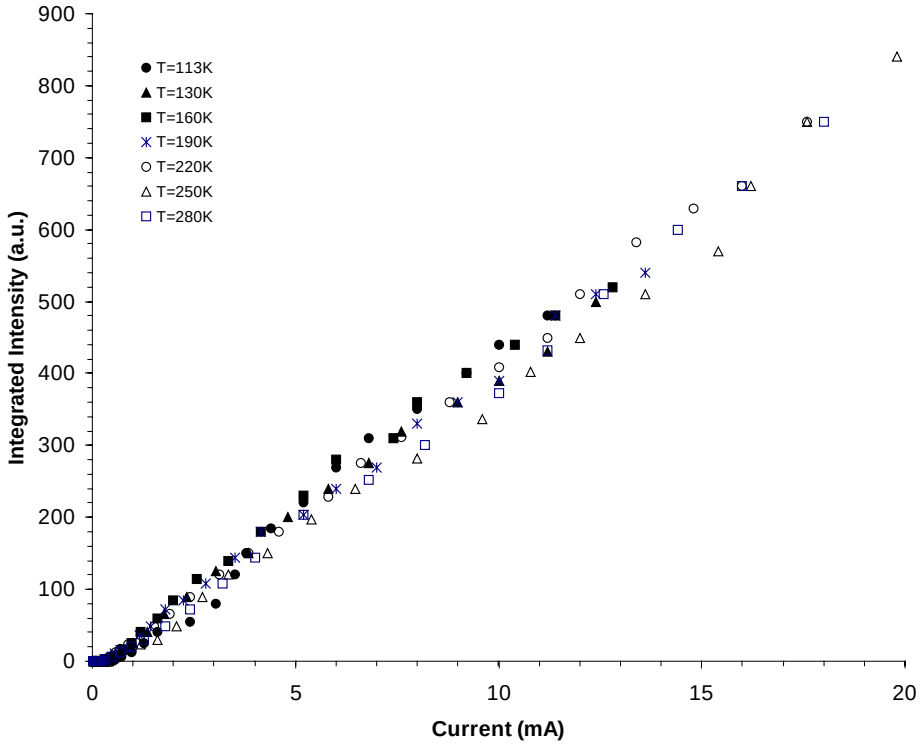

Figure 49. The light-output against current of QT1138 temperature dependence.

The temperature dependence of the L-I plots show that there is very little change in the slope of the L-I curve. The threshold currents are very low with a maximum of 0.75 mA. Although there is a definite take-off in the L-I curves, the emitted light is rather low. The temperature dependence of the threshold current is shown in Figure 50. It follows a parabolic variation in threshold current The broken line is a curve fitted to guide the eye.

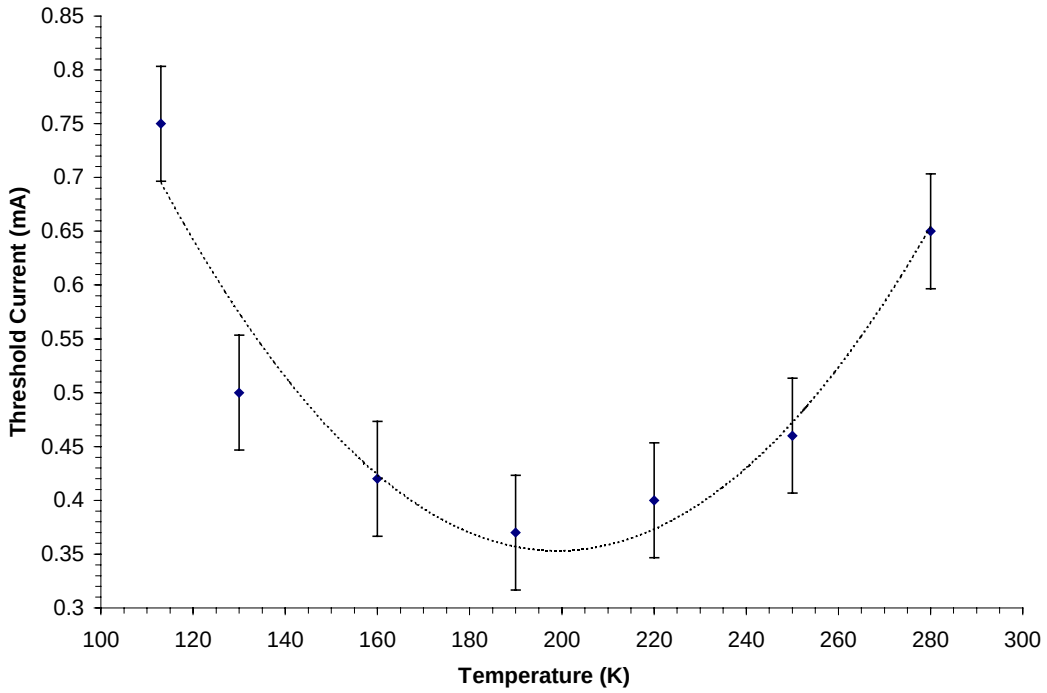

Figure 50. Temperature dependence of the threshold current, the broken line is a curve fitted to a parabola. The minimum threshold current occurs close to T=190 K.

The broad minimum threshold current occurs at temperatures between 160 K and 220 K with the threshold current increasing sharply at a temperature close to T=290 K. This gives an insight into the low power output from the device a room temperature. At this temperature, the cavity resonance is sampling the tail-end of the gain spectrum and lasing occurs only at high threshold currents and power outputs are low. The current density, rather than threshold current, is a comparable measure between different devices. The threshold current at room temperature will be 0.8 mA, the emission diameter is 8 μm giving a current density of

$$J_{th} = I_{th} / A = \frac{0.8 \times 10^{-3}}{\pi \times \left(4 \times 10^{-4}\right)^2} \cong 1.59\, kAcm^{-2} \qquad \textbf{(82)}$$

This does seem reasonable. Other examples of GaAs MQW lasers report threshold current densities of around 1 $kAcm^{-2}$ [81,95] The light from the QT1138 VCSEL was also coupled into an optical fibre and the spectrum measured using an optical spectrum analyser The output power is 1 μW at 868 nm which is very low. The FWHM is 3 nm, which is very high. At room temperature, the observed emission wavelength is 868 nm.

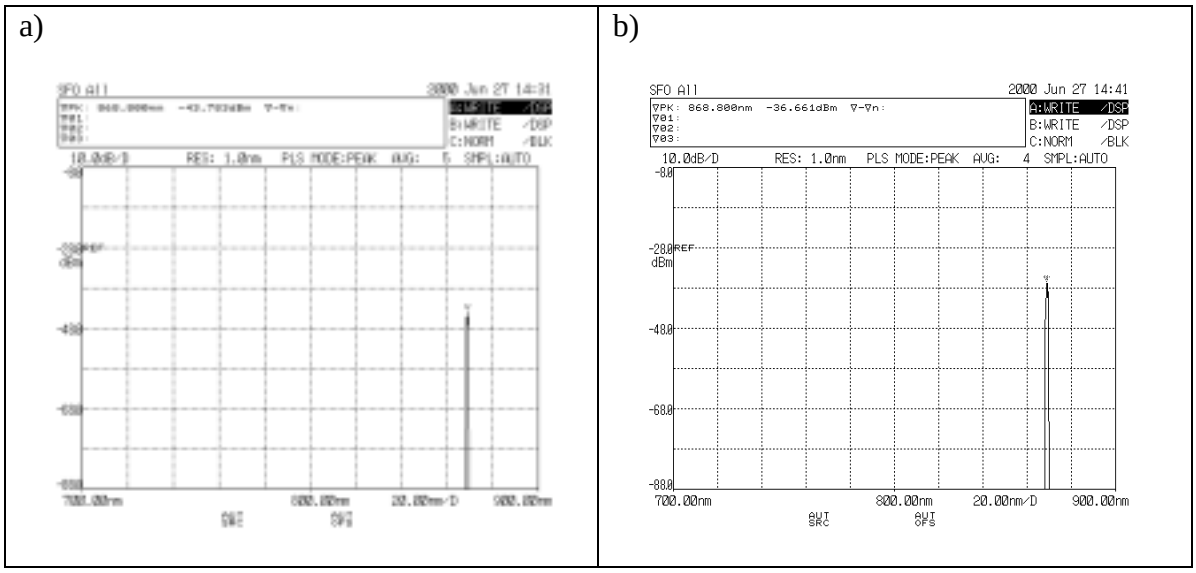

Figure 51 The emission spectrum from the VCSEL current. Emission is at 868 nm. a) shows the spectrum at 2 mA with peak intensity –35 dBm, while b) is at, 36 mA with peak intensity – 30 dBm corresponds to a power of 1 μW.

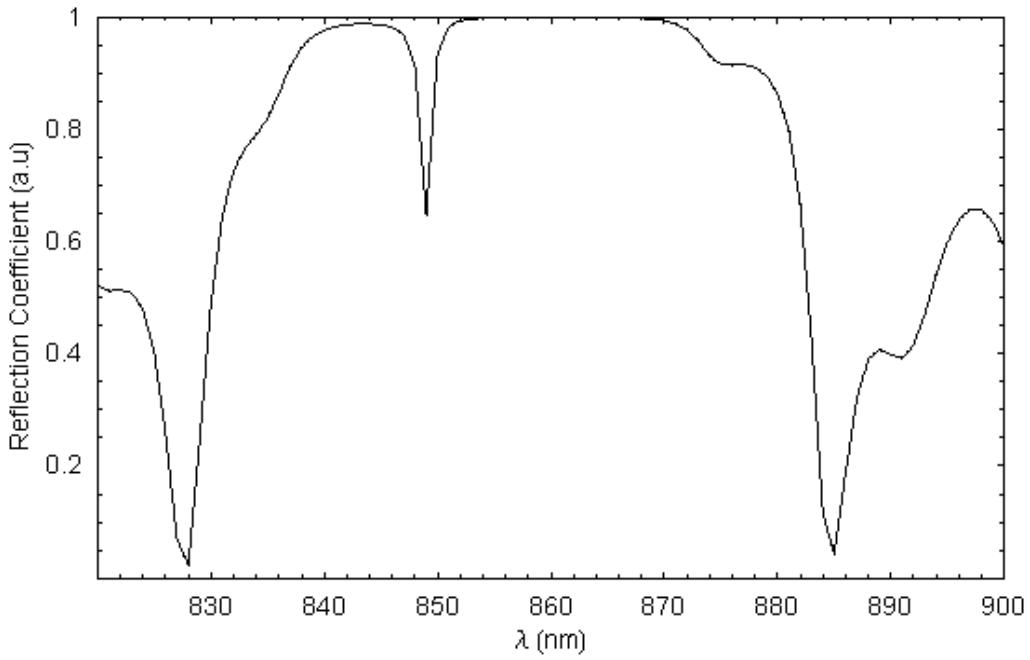

Figure 52. Calculated reflectivity profile at T=300 K using the layer structure from the growth sheet. Cavity resonance occurs at 849 nm.

The calculated reflectivity results at room temperature is shown in Figure 52. The stop band has a FWHM of 54 nm with a definite but broad cavity resonance at 849 nm. The cavity resonance must be at 868 nm at room temperature since is a measured result. To adjust the reflectivity spectrum so that the cavity resonance is at 868 nm we must introduce a systematic growth error of 1.5 monolayers over the entire structure. Figure 53 shows the newly calculated reflectivity spectrum incorporating this relative growth error.

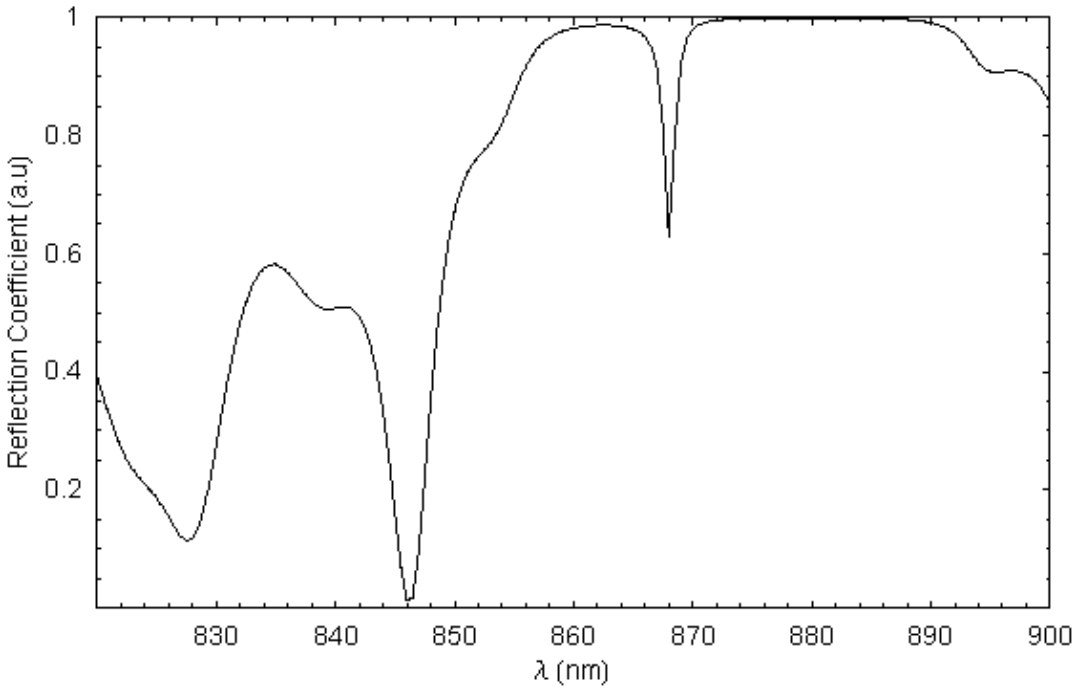

Figure 53. Calculated reflectivity profile at T=300 K using the layer structure from the growth sheet and systematic error of +1.5 monolayers. Cavity resonance now occurs at 868 nm

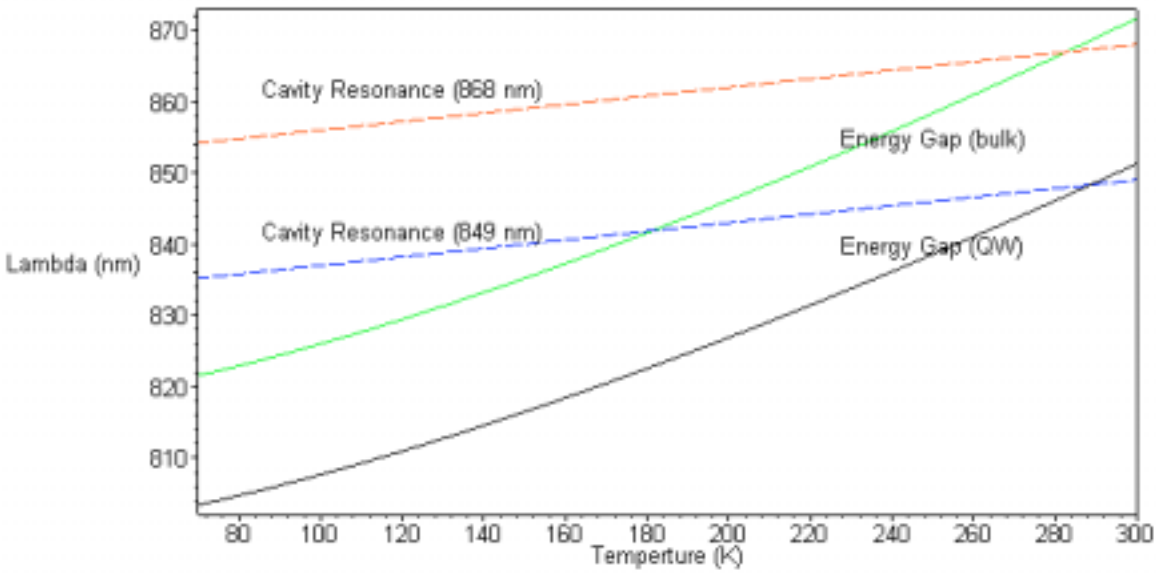

Figure 54. The temperature dependence of the gain spectrum and cavity resonance.

Figure 54 shows the temperature dependence of the cavity resonance and energy gap, as calculated using Equation 45. There are two sets of temperature dependence for the cavity resonance. The red, dashed curve shows the temperature dependence of the cavity resonance starting at 868 nm at room temperature, while the blue dashed curve shows the temperature dependence of the cavity resonance starting at 849 nm at room temperature. Both of these curves will be used in the following discussion. Also shown, is the temperature dependence of the energy gap for bulk material and the temperature dependence of the energy gap for the quantum well. The lowest threshold current, in GaAs/AlGaAs material, occurs at a temperature where the energy gap and the cavity resonance are coincident. With the cavity resonance set at 849 nm at room temperature, the energy gap for the bulk material and cavity resonance are coincident at T=175 K. The energy gap of bulk material is the limiting case of the energy levels in a quantum well; when the well width. is large, the steps in energy become quasi-continuous. Since no energies in the quantum well can be below the energy gap, the bulk material energy gap is a lower bound on the energy.

The temperature dependence of the quantum well is calculated by finding the first energy level in the conduction band and the first energy level in the valence band and adding it to the temperature dependent energy gap. For the quantum wells in this device, the first energy level (e_1) occurred at 25 meV in the conduction band and at 5.6 meV in the heavy hole valence band (hh_1) giving a total emission wavelength of 852 nm. The temperature dependence of the quantum wells follow the temperature dependence of the bulk state but the wavelength is reduced as the energy for the e_1-hh_1 transition is greater than of the energy gap.

Figure 50, shows that the minimum threshold current occurs at temperatures between 160 K to 220 K. The temperature dependence of energy gap for the quantum well is coincident with the cavity resonance at a temperature of T= 290 K. Clearly, this is well above the observed threshold current minimum. We might explain the difference in temperature by overgrowth of the quantum wells which will bring the e_1-hh_1 transition closer to the energy gap and produce a result that is in agreement with the observed minimum threshold current temperature. This is assuming that the cavity resonance was at 849 nm. This conflicts with observed results from the spectral results which showed emission at 868 nm.

Taking the cavity resonance as being at 868 nm, which could be achieved by the systematic overgrowth over the entire wafer, the cavity resonance is shifted, to match the gain spectrum. Now, the temperature at which the energy gap and cavity resonance are equal is above room temperature. We can try and shift the quantum well energy but the energy levels cannot be less than the bulk energy-gap. We cannot meet the temperature dependence requirement by assuming the energy gap is fixed, however, the results might be explained if the energy gap at T=0 K is treated as a variable.

The cavity resonance has been determined experimentally at 868nm and cannot be shifted, however, the initial value of the energy gap can be shifted by the introduction of impurities in the active region, this enables us to shift the bulk value of E_0 in the Varshni temperature dependence. Taking this into consideration, an increase in the wavelength of 30-50 nm at T=0 K will bring the energy gap for the quantum well and the experimental cavity resonance into line with the emission spectrum at the same temperature observed for the minimum threshold current.

4.2 InGaAsP VCSELs

The main aim of the work presented in this section was to understand the temperature dependent operation of InGaAsP/InP VCSEL structures. This was carried out by i) studying the experimental temperature dependence of VCSEL.[96] ii) studying the temperature dependence of photoluminescence from the edge and top of the structure containing the bottom DBR but no top DBR forming what we shall term the quasi-cavity. iii) Developing a theoretical model to describe the experimental results.

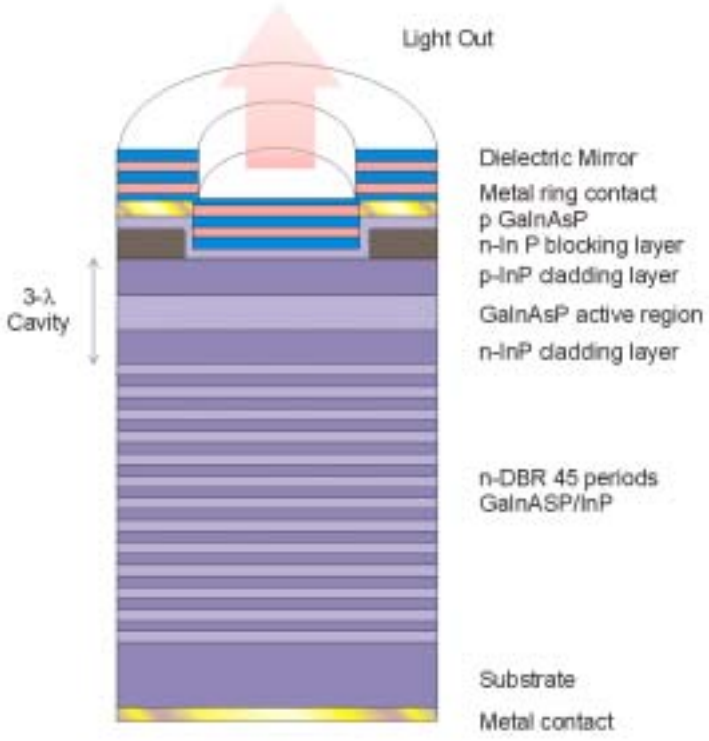

Figure 55. Schematic diagram of AT2339 VCSEL for 1.5 μm operation.

The VCSEL structure used for this work has a 45 period n-type InP and n-type InGaAsP pair DBR grown by gas source MBE. The layers above were grown by MOVPE,

consisting of an n-doped InP spacer layer, a bulk InGaAsP active layer, and a p-type InP spacer layer, forming a 3-λ cavity. This was topped by an n-type current confinement layer, etched away to form a 16 μm diameter top window, and a p-type InGaAsP contact layer. A Ti-Au top ring contact is covered by a 4 period Si/Al_2O_3 dielectric reflector. This structure was mesa-etched to form a two-dimensional array of 64 individual VCSELs with an outside mesa diameter of 56 μm.

Testing on the VCSEL, structure was carried out earlier on the VCSEL structures by Russell Sceats a colleague in our research group. The following section presents some important results from his work.

The VCSEL was electrically pulsed with 100 ns pulse widths at a frequency of 5 kHz. In order to ensure that the Joule heating was minimal experiments were carried out as a function of pulse width and/or duty cycle. At pulse widths around 100 ns neither the emission wavelength nor threshold current change with pulse width and therefore heating effects were minimised but by no means eliminated completely, as we discuss below. Light output was measured over a range of temperatures from 125 K to 240 K. In this temperature range the VCSEL had a clearly defined set of lasing threshold currents with a minimum value at 180 K of 26.5 ± 0.5 mA as shown in Figure 56. This corresponds to a threshold current density of 13.2 $kAcm^{-2}$.

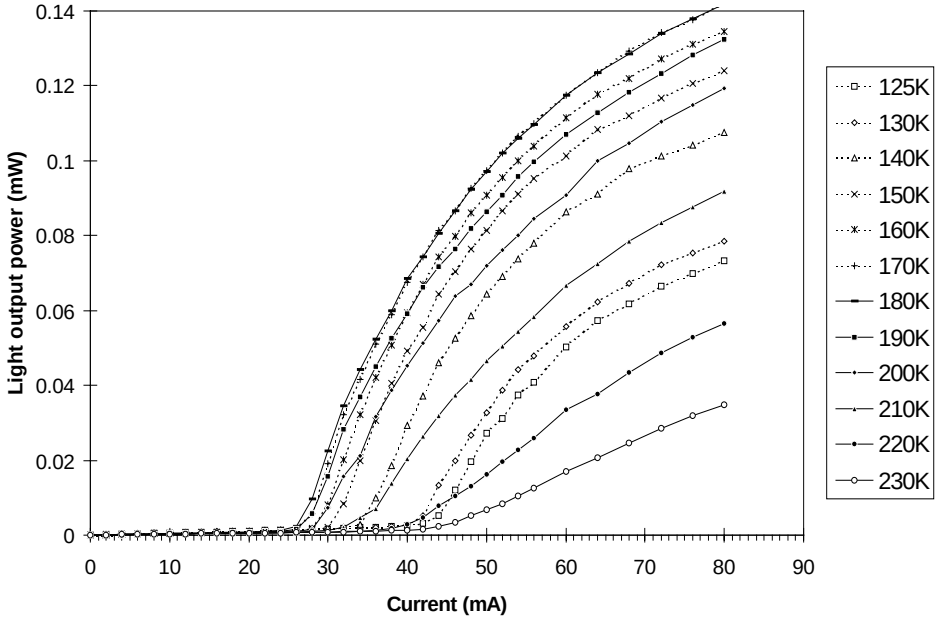

Figure 56. VCSEL light output over a range of temperatures. [96]

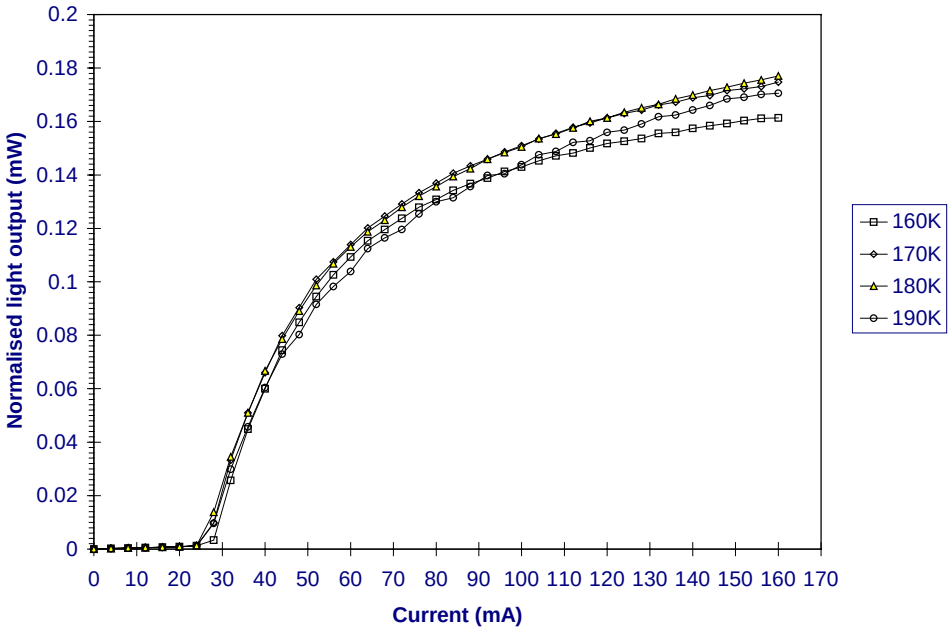

Figure 57. Power output showing saturation. [96]

It is evident from Figure 57 that the light output (L-I) curves at each temperature tend to saturate as the injection current is increased. This saturation effect has been reported previously [97, 98]. The L-I curves of edge emitting laser diodes, where the Fabry-Perot modes are closely spaced, do not show this effect. However the 3-λ cavity within the VCSEL structure has very widely spaced modes, so any changes to the material gain peak relative to the Fabry-Perot mode will affect the output power. Since the current is injected into the laser diode via the bottom 45-period DBR, which has a relatively high series resistance, the active layer temperature can increase relative to the heat sink. Furthermore, higher current densities give rise to a higher heat density, causing a larger temperature gradient throughout the VCSEL. This is further complicated, since the optical field also increases the internal temperature at different locations within the VCSEL structure. However, on reducing the pulse width of the current injection from 100 ns to 40 ns and 20 ns, very little change in this L-I saturation occurred, indicating that heating may not be the entire cause of the output saturation in our device. Due to the relatively large optical window, spatial hole burning (SHB) [99] at higher current densities may have a major contribution to the L-I curve roll-off. As the centre of the optical window, where the optical mode is strongest, draws the carriers in to maintain the material threshold gain, so the carrier density around the perimeter of the window increases. The optical mode at the perimeter is weak, so the conversion of carriers into light is poor, causing a local increase in the lasing threshold current density away from the centre of the optical window.

The variation in lasing threshold current (I_{th}) with lattice temperature is shown in Figure 58. The threshold current density has approximately a parabolic dependence on temperature with a broad minimum at temperatures between T=170 K and T=190 K. The

observed behaviour may be due to the disparity between the temperature dependence of the material gain peak and the cavity resonance. [80] This causes the material gain peak to red shift at a higher rate than the Fabry-Perot mode as the temperature increases. Below 180 K, the gain peak moves towards the Fabry-Perot mode, whilst above 180 K the gain peak moves away from the Fabry-Perot mode. To obtain VCSEL operation at room temperatures, the cavity resonance needs better matching to the material gain by adjusting the design parameters [100].

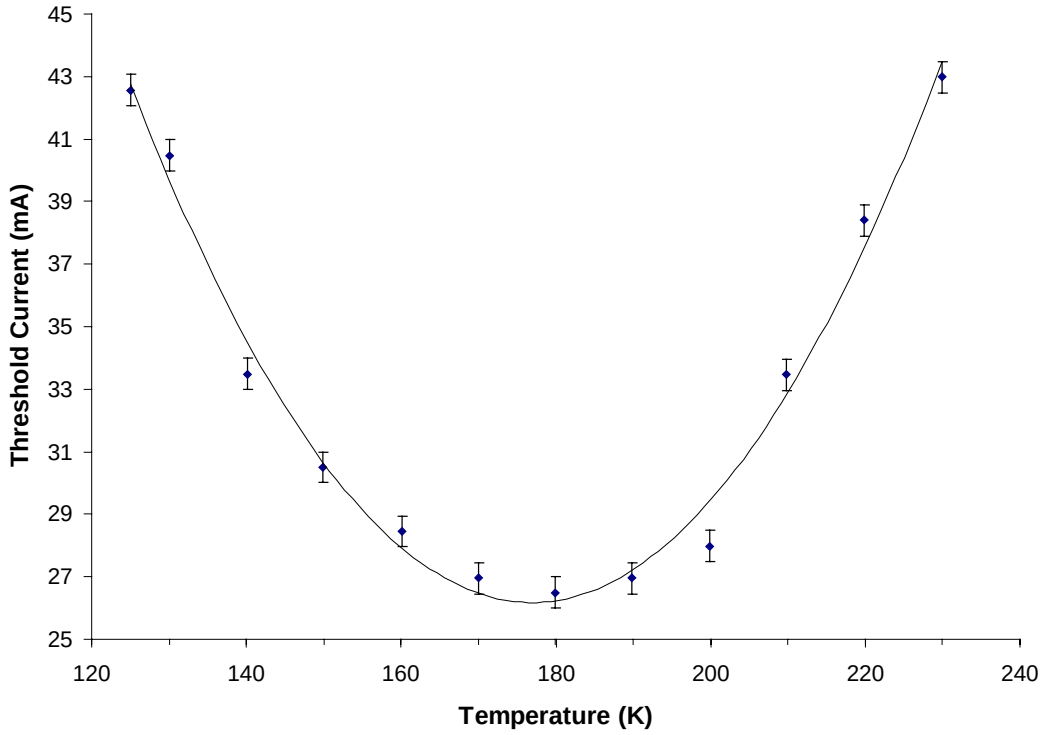

Figure 58. Measured temperature dependence of threshold current. [96]

The output power of the VCSEL at 180 K with an injection current of 160 mA was 0.18 mW, measured from the top surface. To confirm lasing the output was measured through a Newport Broadband polariser, rotated through 360°. The output was highly linearly

polarised with an extinction ratio of greater than 20, indicative of a coherent optical emission.[96]

The spectral peak of the VCSEL output was also measured across the temperature range of 125 K to 235 K. The peak wavelength which is the cavity resonance in a VCSEL structure - varied with temperature as $\lambda = \lambda_o + mT$ with m = 0.095 K^{-1}, in a range between 1.501 μm and 1.512 μm across a 100 K temperature span.

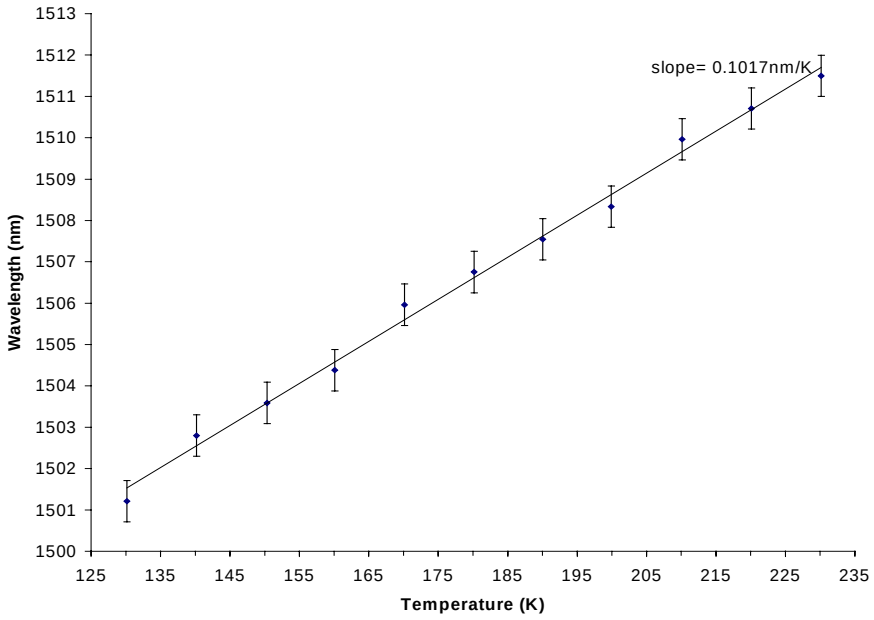

Figure 59 Peak wavelength of AT2339 VCSEL measured as a function of temperature. [96]

The reflectivity spectrum was calculated using parameters given by growers along with the transfer matrix method outlined in Section 2.5.1, for this device and is shown in Figure 61. The cavity resonance occurs at 1.5 μm.

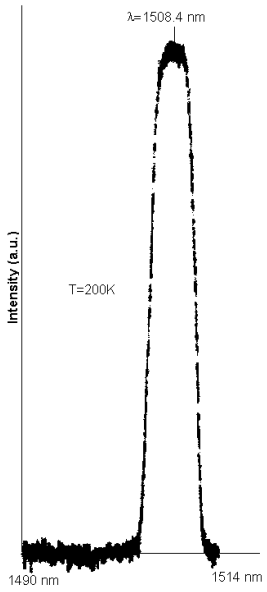

Figure 60. Emission Spectrum at T=200K. [101]

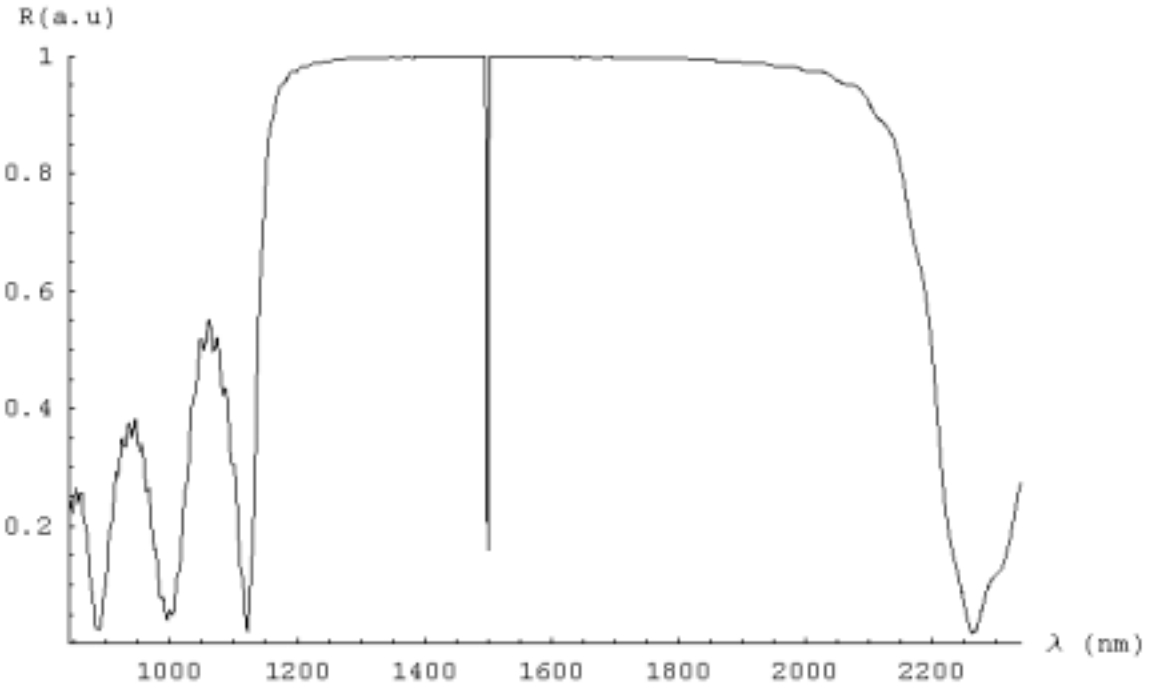

Figure 61. The reflectivity spectrum for the BT VCSEL. The wide stop-band is due to the high contrast ratio of the dielectric top mirror.

4.2.1 Quasi-Cavity Surface Emission

The effect of the emission spectrum in a VCSEL is masked by the cavity. In order to de-couple the effects of the cavity we looked at same AT2339 VCSEL structure without the top mirror. The quasi-cavity device has the same structure as the VCSEL, with the exception that top dielectric mirror is omitted. In addition, there is no need for metal contacts evaporated on to the structure since it is to be optically pumped. We performed photoluminescence and electroluminescence from the top surface and edges of the device as a function of temperature and pump laser power. The structure of the quasi cavity is shown in Figure 62.

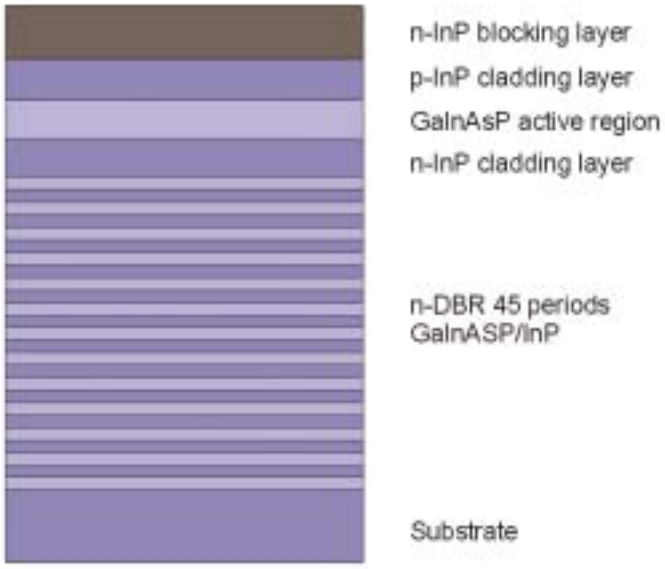

Figure 62. Quasi-cavity wafer structure.

The wavelength and intensity of the emitted light from the top surface of the quasi-cavity device is determined by the emission spectrum of the active region and the reflectivity spectrum of the quasi-cavity. Using transfer matrices, the reflectivity spectrum of the

quasi-cavity was calculated as shown in Figure 63 together with the photoluminescence (PL) spectrum measured as described below, at the same temperature.

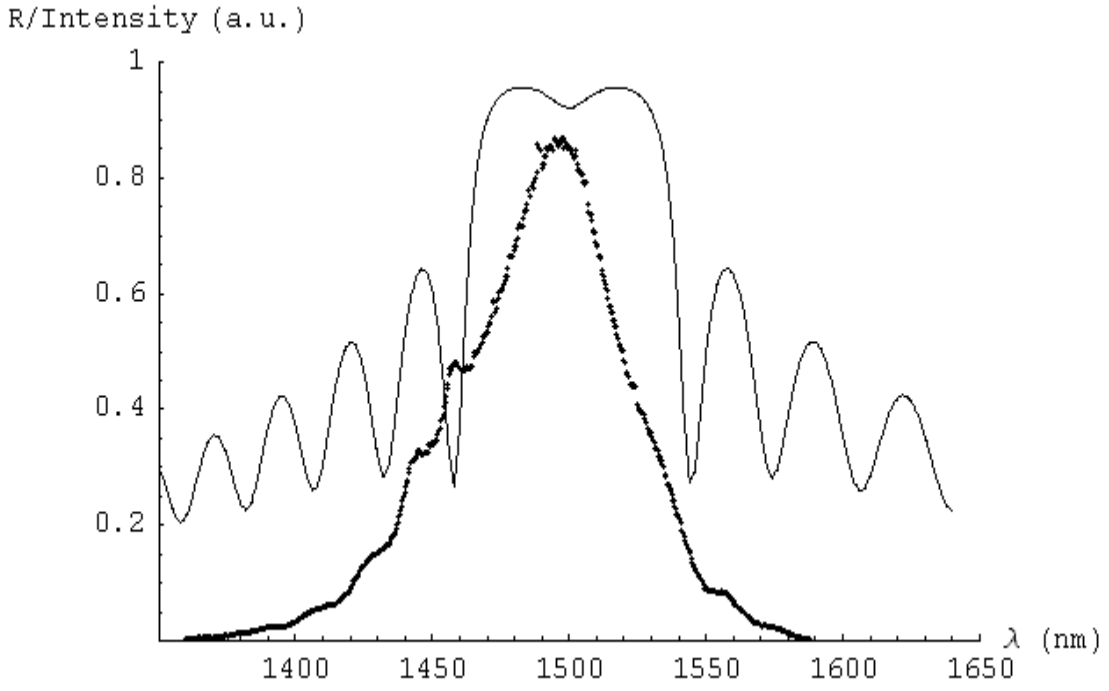

Figure 63. Calculated reflectivity spectrum for the quasi-cavity at T=140 K with the photoluminescence data (points) at the same temperature superimposed.

The calculated reflectivity profile shown in Figure 63 is in excellent agreement with photoluminescence results. The mode spacing for the side lobes of the calculated reflectivity profile is 25 nm, with a stop band of 75 nm at full width-half maximum, extending from 1460 nm to 1540 nm. The reflectivity spectra shows a slight cavity dip at 1520nm. The peak of the photoluminescence coincides well with the cavity dip in the quasi-cavity reflectivity spectrum and the first prominent side modes is coincident with the minima in reflectivity spectra.

Figure 64, shows the measured PL spectra from the device with quasi-cavity at temperatures between T=120 K and T=280 K. The PL spectra are measured using a λ=1064 nm line of a NdYAG laser, as an excitation source. PL is dispersed, collected and plotted using a 1/3 m monochromator together with a Newport 818IR Germanium detector, boxcar and chart-recorder assembly. The spectra show several minor peaks associated with the minima in the reflectivity profile (peaks 1-4) and an emission peak, where the gain spectra is within the stop-band. The wavelengths of the minor peaks and emission peak 5 are plotted against temperature in Figure 65. The minor peaks have a linear temperature dependence, with slopes between 0.06-0.09 nm/K. The dominant peak in the PL spectra departs from the linear dependence of the side lobes.

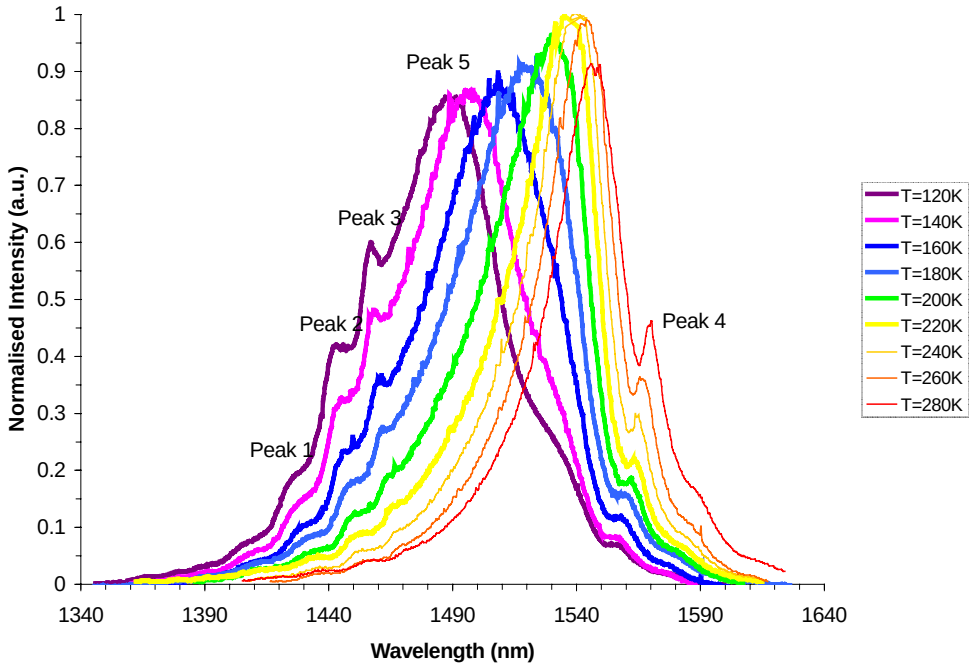

Figure 64. Photoluminescence data as a function of temperature, showing the side lobes and peak intensity used to construct Figure 65

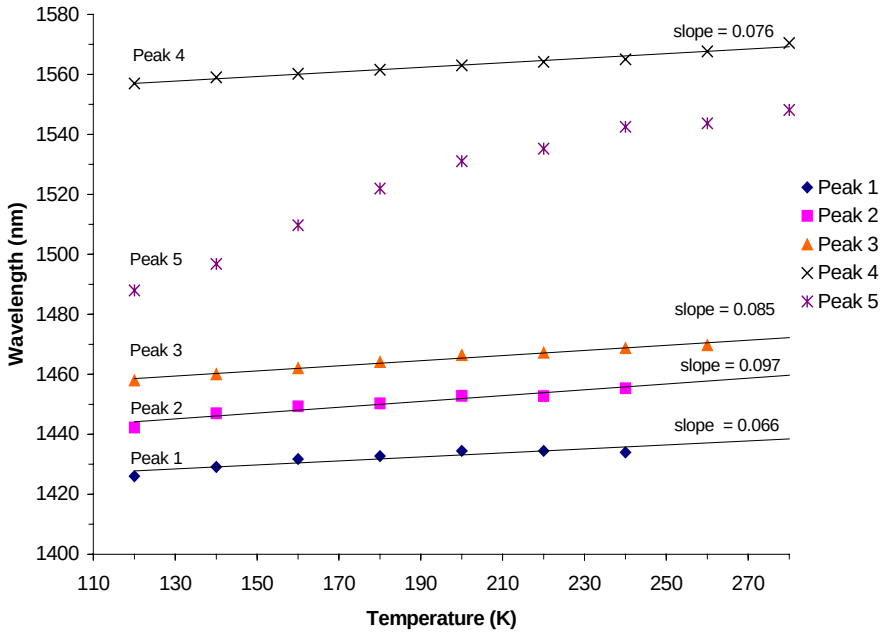

Figure 65. The temperature dependence of the side-modes of the photoluminescence spectra shown in Figure 64 against wavelength. Each mode is linear and has a similar slope, with the exception of the peak wavelength which has a non-linear temperature dependence which follows the change in the band-gap energy.

The temperature dependence of the cavity resonance is as a result of the change in the refractive index of the layers in the structure. The variation with refractive index is linear having the following relationship: [59]

$$n = n_0 + \Delta n\, T \qquad \textbf{(83)}$$

In most semiconductor materials, the change in refractive index has a magnitude of 10^{-4} K^{-1} [102] and for the purpose of the model we have used a value of 2 x 10^{-4} K which gave a good agreement within the model.

For Fabry-Perot modes which the spectrum follows we have:

$$\frac{M\lambda}{2n} = L \qquad \textbf{(84)}$$

Since n is proportional to λ, the variation in wavelength with refractive index must be linear. The change in refractive index with temperatures is therefore:

$$\frac{\Delta\lambda}{\Delta T} = \lambda_0 \frac{\Delta n}{n} = \frac{1500 \times 2 \times 10^{-4}}{3.3} = 0.091 nmK^{-1} \qquad \textbf{(85)}$$

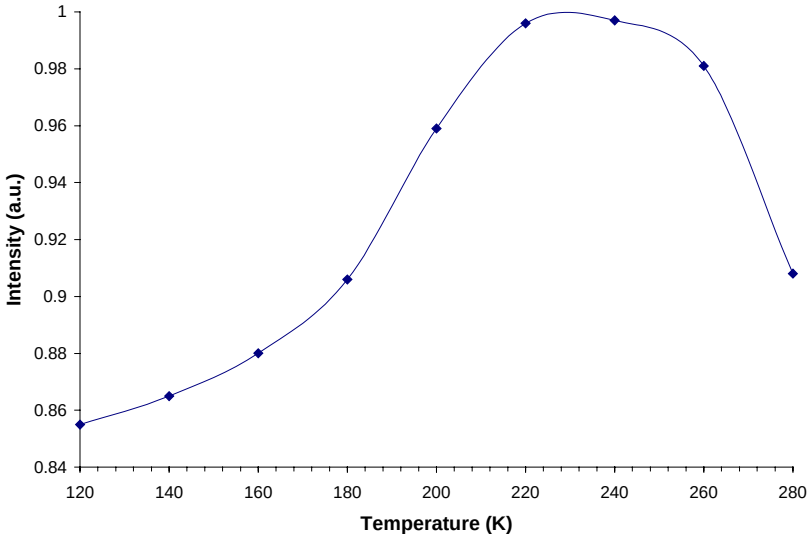

Figure 66. Peak intensity of the photoluminescence mode against temperature.

For a constant pump power, the temperature dependence of the peak PL intensity also gives information about the relative positions of the emission spectra and the cavity dip. Figure 66, shows the maximum intensity of the dominant PL peak (Peak 5) as a function of temperature. As the peak of the emission spectra moves into the cavity dip, the intensity of emission increases. At higher temperatures the gain peak moves away from

the cavity dip and the intensity of emission reduces. The maximum intensity is reached at a temperature of T=230 K. The temperature at which the maximum intensity occurs within the quasi-cavity can be compared with the temperature at which the minimum threshold current occurs for the VCSEL structure. The threshold current against temperature results are shown for the VCSEL structure in Figure 58. The VCSEL exhibits a minimum threshold current where the peak in the gain spectrum is coincident with the cavity resonance. The lowest threshold current occurs at T=180 K. The difference in temperature at which the maximum intensity of the photoluminescence mode occurs in the quasi-cavity and the temperature at which the minimum threshold current occurs within the VCSEL can be accounted for if the gain spectrum and cavity resonance were mismatched by 50 K at the minimum threshold current. Just such a mismatch has been shown to occur for bulk active layer materials [100] and for quantum well active regions by Piprek [103]. Also of note is the wide temperature range over which the peak intensity of the photoluminescence mode is high. This is because the cavity dip of the quasi-cavity is less pronounced than would be expected for a VCSEL cavity.

4.2.2 Quasi-Cavity Edge-Emission

In order to de-couple the effect of the shift in the cavity dip from the gain spectrum we performed PL on the quasi-cavity pumped from top surface and the emission was collected from the edge of the structure. In this configuration, the cleaved facets are expected to act as a Fabry-Perot cavity. The large size of the cavity introduces a large number of cavity modes. Resonance occurs when an integer number of half-wavelengths that fit into the cavity.

If the change in refractive index with wavelength is small, the spacing between modes is of the order of 0.2 nm and thus the Fabry-Perot modes are too close to be resolved on our plots, as the resolution of the monochromator that was used in the experiments was about 1nm at the measured wavelengths. The photoluminescence recorded from the edges of the structure, the cleaved sides of the device are expected to act as a Fabry-Perot cavity. However, the modes are superimposed upon the gain spectrum.

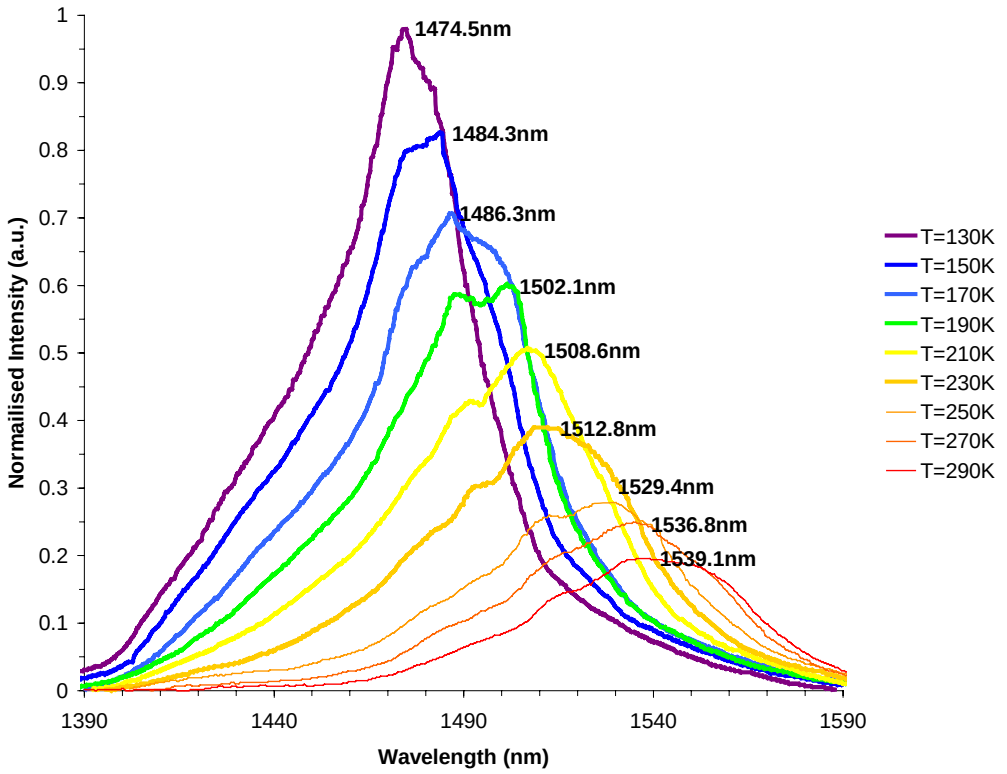

Figure 67. Edge-emission photoluminescence results for temperatures between T=130 K and T=290 K. The numbered wavelengths represent the wavelength where peak emission occurs.

The dependence of the emission spectra will be determined by the temperature dependence of the energy gap of the active layer, InGaAsP. This is given by the Varshni relationship:

$$E(T) = E_0 - \frac{\alpha T^2}{T + \beta} \quad \textbf{(86)}$$

Where E_0 is the energy gap at zero Kelvin, α and β are constants for the material concerned. E_0 = 0.86 eV gives a close fit to the experimental data, α = 4.906x10^{-4} and β=327 [58] corresponding to InP.

Figure 67 shows the edge emission spectra from T=130 K to T=290 K. The figures alongside each curve are the peak wavelength of the emission. In Figure 68, the peak wavelength of the edge-emission photoluminescence is plotted along with the temperature dependence of the energy-gap. There is a good agreement between the two curves indicating that the emission spectra from the edge-emission photoluminescence results has separated the emission spectrum from the cavity. Also shown, by the dashed line, in Figure 68 is the temperature dependence of the cavity resonance for the VCSEL structure. Where the line of the cavity resonance crosses the curve for the peak of the edge emission data, indicates where the emission spectrum and the cavity resonance are aligned. It is between 190 K-210 K. The result obtained from the study of the threshold current against temperature for the VCSEL. (Figure 58) was 180 K. Given that the effects of the cavity have been separated from the gain spectrum, by edge emission PL, we can see that the 180 K minimum threshold current is closer if we accept the 30 K gain offset predicted by the theory. The main peak from the top emission as shown in Figure 64 however does not agree with a temperature dependence predicted by the equation (86) because its temperature dependence is partially modified by the wide cavity resonance as explained above.

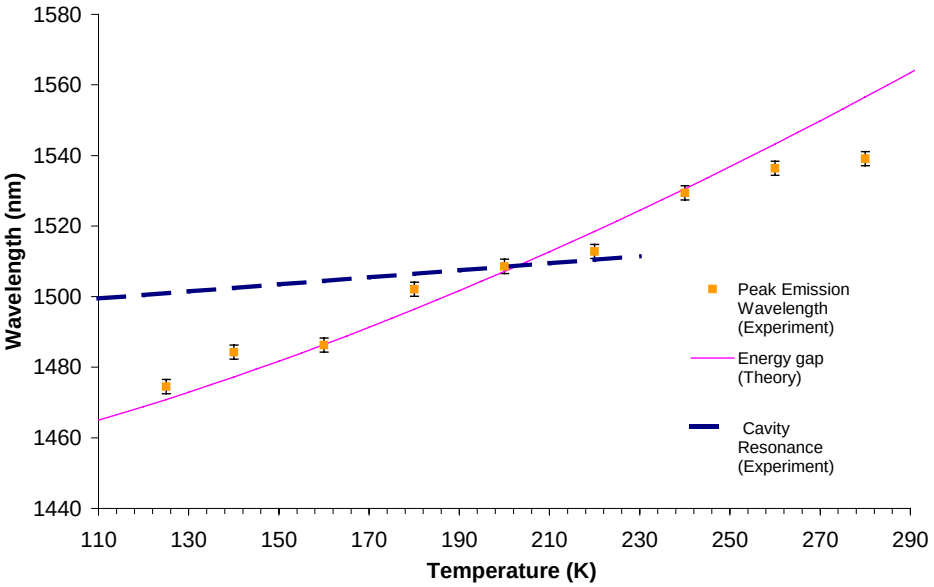

Figure 68. Peak emission plotted for edge-emission photoluminescence results. Solid line represents the temperature dependence of the energy-gap. Also shown by the dashed line is the temperature dependence of the cavity resonance for the VCSEL structure.

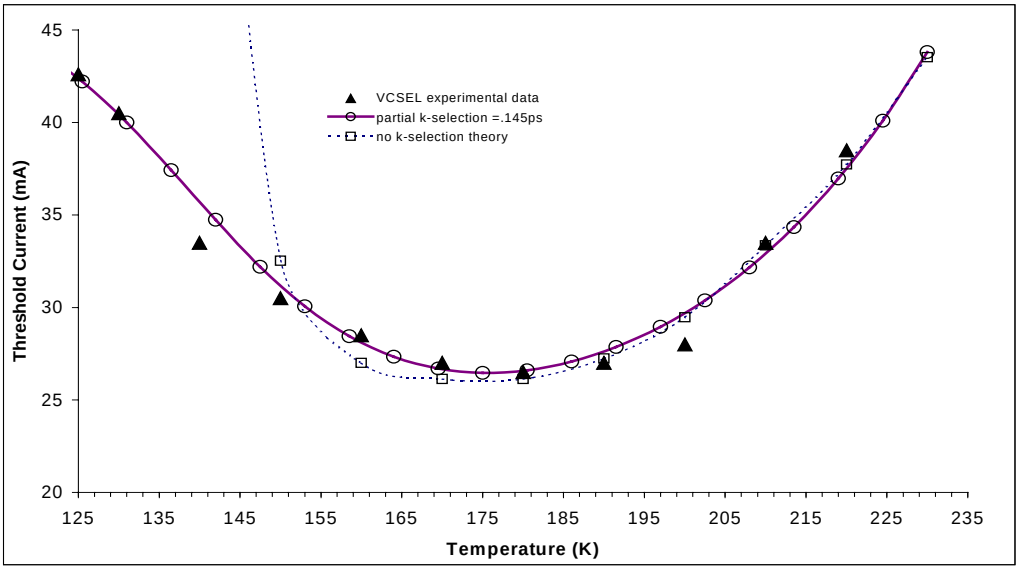

Figure 69. Best fit curves for energy gap temperature dependence and cavity resonance temperature dependence of quasi-cavity experimental data applied to theoretical calculation to obtain the threshold current/temperature dependence of the VCSEL structure. [96,104]

Figure 69, shows the result of theoretical modelling by Desi Ramoo, a colleague within the optoelectronics research group, of the threshold current with temperature applied to a VCSEL structure with the parameters obtained with the experimental data. No k-selection shows a marked divergence at low temperatures and this is to be expected given the simple nature of the model. When, partial k-selection is introduced, the fit becomes significantly better. The best fit is obtained with adjustment of the optical confinement factor and scattering time constant. To compare with this theoretical model and experimental results, the temperature dependent operation of the AT2339 VCSEL was also modelled using the approximation given by Marinelli, [66] described in Section 2.6.5. Figure 70, shows the temperature dependence of the threshold carrier concentration. There is good agreement with the threshold current model and experimental results. with the minimum carrier density occurring at T=176 K

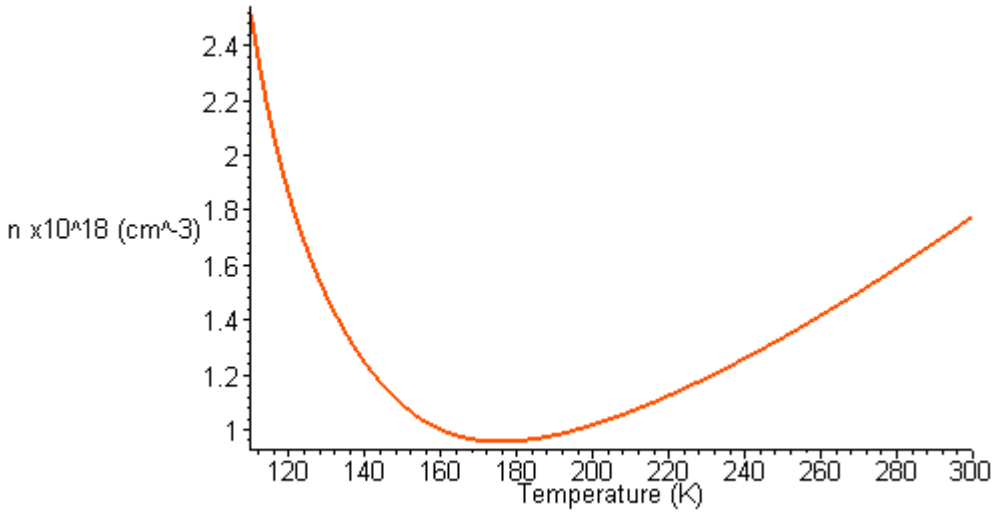

Figure 70. Threshold carrier concentration of a bulk InGaAsP VCSEL. The minimum carrier concentration occurs at T=176 K.

By using the transparency condition of gain equals loss, and estimating the losses to be α=100 cm^{-1}, the peak energy, at threshold, against temperature can be calculated. Figure 71 shows the result of this calculation. We have taken the energy gap as E_g=0.827, which corresponds to an emission wavelength of 1.5 μm, and used the Varshni parameters α and β from the variation of InP.[58] Superimposed on this curve is the rate of change of the cavity resonance with temperature, inferred from the movement of the side lobes in (Figure 65) and also the shift in the emission spectra of the VCSEL. Figure 59

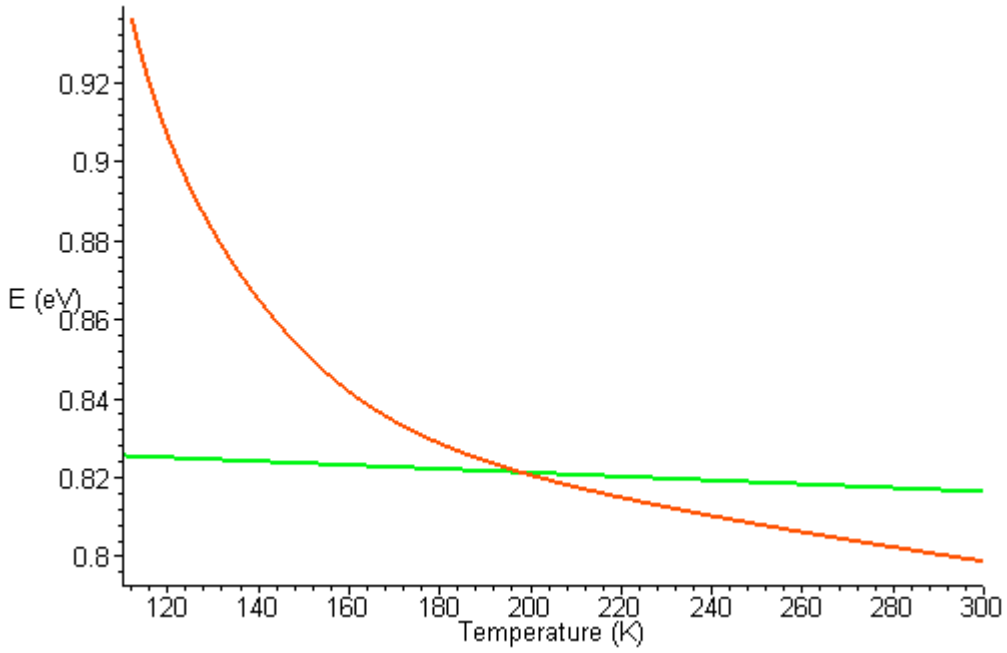

Figure 71. The temperature dependence of the gain peak with temperature and the variation of the cavity resonance. The crossing point occurs at T=196 K, this is 20 K higher than the minimum temperature of the threshold current for the VCSEL structure.

Figure 71, shows the variation of the peak energy of the gain spectrum for the same device and the temperature dependence of the cavity mode. The coincidence of the gain peak and cavity resonance occurs at T=196 K, good agreement with the experimental

results found in the photoluminescence of the quasi-cavity (Figure 68). From the model we see that the temperature at which the gain peak is coincident with the cavity resonance is some 20 K higher than the temperature for which the minimum threshold current occurs. This model doesn't take into account any losses from non-radiative recombination effects which are significant for this material at high pump powers. Auger recombination tends to decreases the temperature at which the minimum threshold current occurs while IVBA increases the temperature at which the laser gain peak is coincident with the cavity resonance.

4.2.2 Power Dependence

To examine the effect of increasing power at constant temperature on the PL spectrum, the quasi-cavity was subjected to increasing levels of laser pump power. PL spectra were taken at T=110 K to ensure that strong emission from the sample was obtained even at low pump powers. PL against laser pump power was recorded from both the top and edge of the quasi-cavity. Figure 72, shows the peak intensity of the PL curves against incident power for both top-emission and edge-emission of the quasi-cavity. The top emission curves show little variation in wavelength with increasing pump intensity, with an almost linear change in wavelength with power of 5.7 nmW^{-1}. With increasing power, we would expect some heating and the injection of carriers into the sample to cause a change in the refractive index of the material. The wavelength of the emission will be modified by the bottom DBR layers and so the emission wavelength increases slowly with increasing pump power. With edge-emission PL results, the device is once again acting like a Fabry-Perot cavity. Increasing the power causes the wavelength to shift as the emission spectrum moves with temperature. As a new resonant mode becomes

dominant, the emission jumps to a new wavelength. This is a common characteristic in Fabry-Perot lasers. [105]

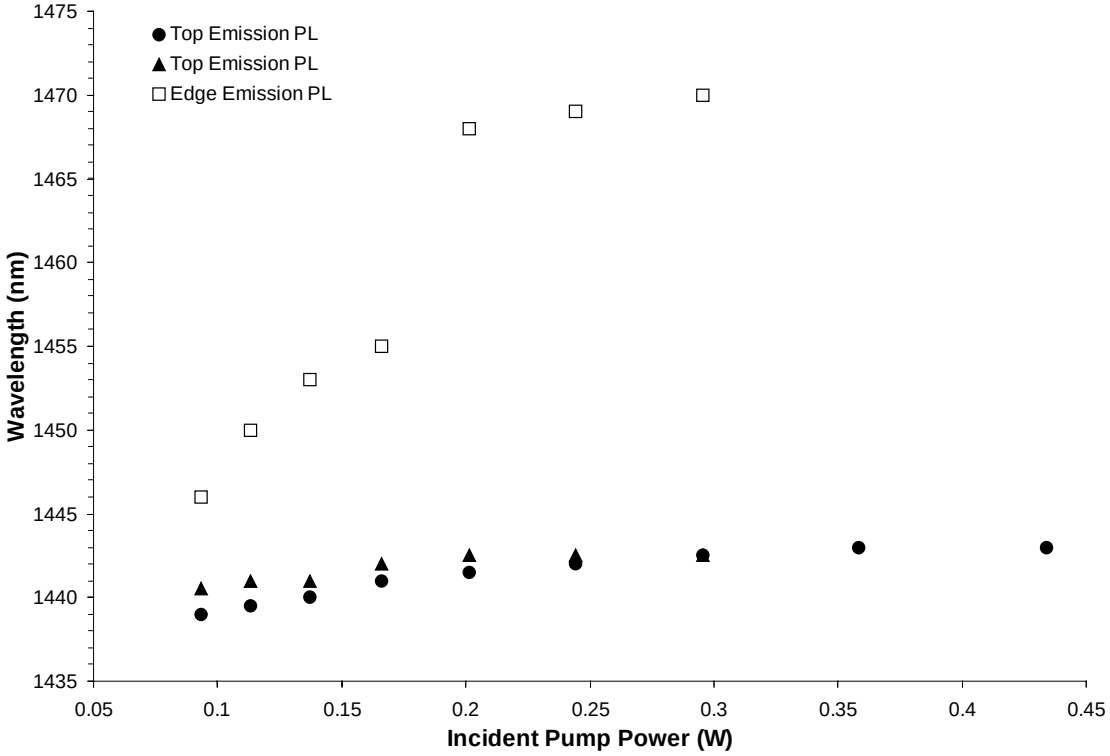

Figure 72. Dependence of wavelength on the incident power of the pump laser at T=110 K.

4.2.3 Electroluminescence

Electroluminescence on the quasi-cavity structure was attempted but yielded no useful results. The original wafer structure had a layer of blocking InP semiconductor for current confinement, which was etched away over the active region of the VCSEL. However, no information regarding the thickness of this layer was available to us, as the people that had been working on these devices had left BT Labs to work elsewhere and so it was pure

guesswork as to how thick this blocking layer was. Using $HCl:H_3PO_4$, in a ratio of 1:3 a sample of the wafer was etched for 2 minutes and the surface profile measured using a stylus. Observing no more change in the depth after a further ten minutes, the etchant was changed to an aqueous solution of citric acid and H_2O_2 in the ratio of 10:1. Etching once again, a further increase in the depth was observed. Etching continued until it was believed to have formed a stripe across the wafer sample. Three such stripes of 200 μm in width and 1 mm long were created. The I-V characteristics of this sample were just a straight line, and no light was detected. The possible cause for this is that the etchant ate away too much of the surface layers, although the stylus reported only a about one micron depth.

5. Conclusions and Further Work

5.1 GaAs VCSELs

We examined the temperature dependence of the A5 GaAs VCSELs for two emission window diameters, namely 100 μm and 70 μm. From the analysis of the I-V and L-I characteristics, we measured the temperature dependence of the threshold current and found it not to have a simple relationship. For the 100 μm VCSEL, the expected parabolic temperature dependence was not apparent. The actual temperature dependence results showed no discernible trend. This was thought to be caused by poorly grown DBRs. Errors in the growth of these layers can cause the emission spectrum to be offset with respect to the gain peak or introduce additional unwanted cavity resonance modes within the stop-band. For the 70 μm VCSEL, instead of a single parabolic variation in threshold current with temperature, the threshold current was minimal over a broad temperature

range of T=300 K to 240 K. Below 240 K, the threshold current increased steadily until it reached 150 K. For temperatures below 150 K, the threshold current once again started to fall until another minimum was observed at T=90 K. These results were explained by the introduction of a second cavity mode caused as a result of random errors in growth. The reflectivity calculations showed that a second mode could have been present although it was somewhat subdued in the data from the growth sheet. Incorporating random errors in the thickness of the layers showed that these features could become more pronounced. Furthermore, the relative movement of the reflectivity spectrum and emission spectrum were such that the modes could become coincident at low temperatures.

A second variety of GaAs VCSEL, with an 8 μm diameter emission window, was investigated. Once again, the temperature dependence of these devices was examined using I-V and L-I characteristics. From the L-I curves, the temperature dependence of the threshold current was found. It showed the characteristic variation of threshold current with temperature associated with VCSELs. To check the position of the cavity resonance, the spectrum of the device was taken by coupling the light into an optical fibre, connected to an optical spectrum analyser. Weak emission occurred at a wavelength of 868 nm The maximum emitted intensity recorded was –30 dBm (~1 μW), at a current of 35 mA. The reflectivity spectrum predicts a cavity resonance at 849 nm, which is not too far from the calculated emission spectrum which occurred at 852 nm.

When the results were analysed and compared with calculations for the emission wavelength of the quantum wells and reflectivity spectrum, it was found that while the results were consistent in their own right, the experimental results for the temperature dependence and the emission spectrum became inconsistent if they were recorded for the

same device. The experimental results are not explained by assuming E_0 in the Varshni temperature dependence can be shifted to higher wavelengths at T=0 K. This would be the case if the active region was not pure GaAs. Decreasing the value of E_0 increases the wavelength at T=0 K and with a shift between 30-50 nm the cavity resonance and energy gap and cavity resonance come into alignment at the temperature of the minimum threshold current. Although the devices tested showed very untypical behaviour, it should not be thought that GaAs/AlGaAs VCSELs cannot be successfully manufactured. Commercially available GaAs VCSELs emitting at 850 nm are available with consistent performance. It is regrettable that the devices we tested performed so poorly. The results were useful in becoming familiar with the experimental techniques and thinking about why properties of VCSELs vary with temperature.

In analysing these result for the GaAs, it would have been helpful in hindsight to have had experimental reflectivity spectra of the devices. We can calculate the reflectivity spectrum, based on the design parameters for the layers, and calculate the emission wavelength of the quantum well. While these are useful in determining the validity of an a particular argument about what is happening within the device, or designing VCSEL structures, actual experimental results are more valuable. For future work, it would be useful to set up the reflectivity kit to verify the position and number of cavity resonances for these GaAs VCSELs.

5.2 InGaAsP VCSELs

Using previously obtained results, from an array of 64 InGaAsP/InP VCSELs, we compared the temperature dependent properties of the device with PL and EL on a sample of the wafer missing the dielectric top DBR, known as the quasi-cavity. From the VCSEL, the threshold current was recorded. The minimum in the threshold current occurred at T=180 K, (Figure 58) and temperature dependent spectral data showed the shift in the cavity resonance (Figure 59).

Collecting the light emission from the top of the quasi-cavity, the bottom DBR modifies the emission spectrum, causing the appearance of numerous side-lobes. From the temperature dependence of these side-lobes, the rate of change with temperature of the cavity resonance for the VCSEL was inferred and found to be in good agreement with the shift in the peak wavelength with temperature for the VCSEL.

To see what is happening to the gain spectrum in a VCSEL is more complicated, since emission is selected by the cavity resonance. To overcome this, PL was used to de-couple the emission spectrum from the cavity. PL from the edge of the quasi-cavity showed it to behave like a Fabry-Perot laser, with many closely space modes within the cavity. As the temperature is increased, the effective length of the cavity is also increased due to the refractive index change and linear expansion of the cavity. The position of the resonant modes will shift relative to the emission spectra. The wavelength will shift until an adjacent mode is closer to the gain peak, causing mode-hopping. This shown in Figure 68. Combining the results from edge emission PL and the inferred shift in the cavity

resonance, the two were combined to predict the temperature at which the lowest threshold current occurs for this device, the temperature was T=200 K. The theoretical model written by Desi Ramoo, which takes into account non-radiative recombination, showed that the temperature for the minimum threshold current occurs at T=180 K. This model provides very good agreement with the experimental temperature dependence of the threshold current for the VCSEL.

Following the procedure described in Masum *et al.*, [100] and substituting parameters for the InGaAsP VCSEL, the threshold carrier density is calculated by matching gain equal to loss. With this information the peak energy of the gain spectrum was obtained. and the experimental temperature dependence of the cavity resonance superimposed. The temperature at which the minimum carrier concentration occurs can be related to the temperature at which the minimum threshold current occurs and it is found to be in good agreement with both the theoretical model by Desi Ramoo and the minimum threshold current for the VCSEL. (Figure 50 and Figure 69)

The theoretical model also predicts that the gain peak will coincide with the cavity resonance at a temperature of 196 K, and this is in good agreement with the temperature predicted by the crossover of the experimental edge-emission PL results and the temperature dependence of the cavity resonance (Figure 68).

In the field, the temperature dependence of VCSELs leads to undesirable characteristics that engineers would like to minimise such as an increasing threshold current, and a roll off in optical power. The traditional method of solving these problems is to maximise the heat-dissipation and cool the VCSEL, but this increases the cost, complexity and reduces the reliability of complete system. A better solution, is to design the cavity in such a way

that the gain spectrum is blue-shifted with respect to the cavity resonance at room temperature. At the operating temperature, the gain spectrum comes into line with the cavity resonance and experiences less variation in the threshold current with increasing temperature. Quantum well structures within the cavity provide numerous advantages and lead to lower threshold currents. The problem of non-radiative recombination in the active-region still remains. Further improvements to the performance can be made with the use of strain in the quantum wells. This leads to a reduction of the effective mass in the heavy hole valence band. In the E-k diagram, effective mass is represented in the curvature of the bandstructure:

$$\frac{1}{m^*} = \frac{1}{\hbar^2}\frac{d^2E}{dk^2} \qquad \textbf{(87)}$$

A reduction in effective mass is shown as an increase in the curvature and transitions between the bands of the correct energy are less likely close to k=0 thus Auger and IVBA are reduced. As long as the strain is kept below the critical value, which is material dependent, the reliability of the laser is very good, as shown by lifetime tests. [106]

Other material systems are available for 1.3 μm VCSELs such as InGaAsN/GaAs.[107] The difference in the refractive indices for this material system is greater than that for InGaAsP/InP. Therefore, fewer layers are required to reach the peak reflectivity in the lower DBR. In addition, InGaAsN/GaAs system has a large conduction band offset resulting in superior electron confinement. Room temperature operation of selectively oxidised InGaAsN/ QW VCSELs has been demonstrated, [108, 109] however, at the present time, growth of high quality InGaAsN is still a problem due to the large miscibility

gap[110, 111, 112, 113] and incorporation rate of Nitrogen drops exponentially with increasing growth temperature. [114]

The formation of self assembled quantum dots has been shown to occur in InGaAsN when deposited on a GaAs substrate, with emission at up to 1.52 μm. [115] Quantum dots are particularly interesting in terms of their temperature dependence. Thomas *et al.* [116] using InGaAs quantum dots emitting at 980 nm, have shown the modal gain and single layer quantum dot systems as a function of temperature. The quantum dots states move with temperature but the peak gain wavelength is insensitive to temperature. Movement of the density of states is offset by the increased Fermi function below E_f, that occurs with lowering temperature. If the desired temperature dependence can be engineered in InGaAsN by controlling the size distribution of the dots, less temperature sensitive VCSELs operating at 1.3 –1.55 μm window will become a reality.

5.3 Publications

1. "Hot Electron VCSEL" - *Part of the SPIE Conference on Physics and Simulation of Optoelectronic Devices VII, San Jose, California 1999 SPIE Vol. 3625, 0277-786X/99*

2. R. Sceats, C. J. Hepburn, R. J. Potter, A. Dyson, N. Balkan, M. J. Adams, "1.5μm Surface Emission From GaInAsP/InP HELLISH Structure", *SPIE Conference*, (2001).

3. Temperature Dependence of GaInAsP VCSELs - *Part of the SPIE Conference on Physics and Simulation of Optoelectronic Devices, San Jose, California*, (2001).

4. N. Balkan, A. Serpenguzel, A. O. Brien-Davis, I. Sokmen, C. J. Hepburn, R. J. Potter, M. J. Adams J. S. Roberts, "VCSELs Structure Hot-Electron Light Emitter", *Materials Science and Engineering*, **B47** pp 96-100, (2000).

5. C. J. Hepburn, R. Sceats, A. Boland-Thoms, N. Balkan, A. J. Dann, S. D. Perrin, I. Read, J. Reed, P. Cannard, M. A. Fisher, D. J. Elton, M. J. Harlow, “Temperature Dependent Operation of GaInAsP/InP VCSELs”, (*to be published*).

5.4 References

1 I. Melngailis, *Appl. Phys. Lett.*, **6**, 3, pp 59-60, (1965).

2 R. Potter, "Surface Emitting Lasers", *MPhil Dissertation, University of Essex*, (1998).

3 R. D. Burnham, D. R. Scifres, and W. Striefer , *IEEE J. Quantum Electron.* **QE-11,** pp 439-449, (1975).

4 Zh. I. Alferov, V. M. Andreyev, S. A. Gurevich, R. F. Kararinov, V. R. Larionov, M. N. Mizerov, and E. L. Portnoy, *IEEE J. Quantum Electron*, **QE-11,** 449-451, (1975).

5 H. Soda, K. Iga, C. Kitahara and Y. Suematsu,, *Jpn. J. Appl. Phys.*, **18**, pp 2329-2330, (1979).

6 A. Chailertvanitkul, S. Uchiyama, Y. Kotaki, Y. Kokobun and K. Iga, *Annual Meet. Jpn. Soc. Appl. Phys. Tokyo, Japan*, (1983).

7 I. Ibaraki, S. Ishikawa, S. Ohkouchi and K. Iga, *Elect. Lett.*, **20** pp 420, (1984).

8 D. L. Huffaker *et al.*., *IEEE Photon. Tech. Lett.* **8**, pp 974-76, (1996).

9 H. Gebretsadik, K. Kamath, W. D. Zhou, and P. Bhattacharya, *Appl. Phys. Lett.*,**72**, 2, pp 135, (1998).

10 B. J. Thibeault, K. Bertilsson, E. R. Hegblom, P. D. Floyd, R. Nanone and L. A. Coldren, *IEEE Photon. Lett.*, **9**, 1, (1997).

11 M. Margalit, J. Piprek, S. Zhang, D. I. Babic, K. Streubel, R. P. Mirn, J. R. Wesselmann, J. E. Bowers, and E. L Hu, *IEEE J. Quant. Elect.*, **3**, 2, pp 359-365, (1997).

12 Y. Qian, Z. H. Zhu, and Y. H. Lo, *Appl. Phys. Lett.*, **71**, 1, pp 25-27, (1997).

13 Y Nakano,. K. Takahei, Y. Noguchi, Y. Suzuki and H. Nagai, *Elect. Lett.*, **25**, pp 1369-137, (1989).

14 H. Nakimizaki,, R. Hirano, H. Higuchi, E. Oomura, Y. Sakakibara, and W. Susaki, *Elect. Lett.*, **18**, 703, (1982).

15 N. K. Dutta, D. P. Wilt, and R. J. Nelson, *J. Lightwave Technol.*, **LT-2**, 201, (1984).

16 W. M. Hinley, M. P. Christensen, P. Milojkovic, J. Ekman, R. Chandramani, R. Rozier, Kiamilev, Y. Liu, *Appl. Optics*, **38**, 29, pp. 6190-6200, (1999).

17 A.E. Wilner, C. J. Changhasnain and J.E. Leight, *IEEE Photon. Tech. Lett.*, **5**, 7, pp 838-841, (1993).

[18] A. Einstein, *Deutsche Physikalische Gesellschaft. Verhandlungen*, **18**, pp 212, (1916).

[19] D. M. Eagles, *Proc. Phys. Soc. London*, **78**, 204, (1961).

[20] L. A. Coldren, S. W. Corzine, "Diode Lasers and Photonic Integrated Circuits", *John Wiley and Sons.*

[21] G. P. Agrawal and N. K. Dutta, "Long Wavelength Semiconductor Lasers", *Van Nostrand Reinhold*, (1986).

[22] M. Takeshima, *J. Appl. Phys.*, **58**, pp 3846, (1985).

[23] B. Sermage, H. J. Eichler and J. P. Heritage, *Appl. Phys. Lett.*, **42**, pp 259, (1983).

[24] E. Winter and E. P. Ippen, *Appl. Phys. Lett.*, **44**, pp 999, (1984).

[25] Syouichi Kakimoto, Hitoshi Watanabe, *J. Appl. Phys.*, **87**, 5, pp2095-97, (2000).

[26] Syoichi Kamimoto and Hitoshi Watanabe, *J. Appl. Phys.*, **85**, 3, pp 1822-24 (1999).

[27] Jason Taylor and Valery Tolstikhin, *J. Appl. Phys.* **87**, 3, pp. 1054-59, (2000).

[28] John Gowar, "Optical Communication Systems (2nd Edition)", *Prentice Hall International Series in Optoelectronics*, (1993).

[29] http://www.amgsystems.techie.org.uk/page6.htm

[30] http://www.treasure-troves.com/physics/MieScattering.html

[31] M. S. Tyagi, "Introduction to Semiconductor Materials and Devices", *John Wiley & Sons, Inc.*, (1991).

[32] I. Mito, M.Kitamura, K. Kaede, Y. Odagiri, M. Seki, M. Sugimoto, and K. Kobayashi, *Elect. Lett.*, **18**, 2, (1982).

[33] R. J. Nelson, P. D. Wright, P. A. Barnes, R. L. Brown, T. Cela, and R. G. Sobers, *Appl. Phys. Lett.*, **36**, pp 358, (1980).

[34] H. Ishikawa, H. Imai, T. Tanahashi, Y. Nishitani, M. Takusagawa and K. Takahei, *Elect. Lett.*, **17**, pp 465, (1981).

[35] N. K. Dutta, D. P. Wilt, P. Besomi, W. C. Dautremont-Smith, P. D. Wright and R. J. Nelson, *Appl. Phys. Lett.*, **44**, pp 483, (1984).

[36] R. A. Logen, J. P. Van der Ziel, and H. Tamkin, *Proc. SPIE Int. Soc. Opt. Eng.*, **380**, pp 181, (1981).

[37] M. Oron, N. Tamari, H. Shtrikman and C. A. Burrus, *Appl. Phys. Lett.*, **41**, pp. 609, (1982).

[38] T. Murotani, E. Oomura, H. Higuchi, H. Namizaki, and W. Susaki, *Elect. Lett.*,**16**, pp 566, (1980).

[39] I. P. Kaminow, P. R. E. Nathory, L. W. Stulz, and J. C. Dewinter, *IEEE J. Quant. Elect.* **QE-19**, pp. 1312, (1983).

[40] W. T. Tsang and R. A. Logan, *Appl. Phys. Lett.* **45**, pp 1025, (1984).

[41] H. Temkin, R. A. Logan, M. B. Panish and J. P. Van der Ziel, *Appl. Phys. Lett.*, **45**, pp 330, (1984).

[42] P. Blood, "Principles of Semiconductor Laser Diodes", *Devices and Systems Winter School Conference, University of Essex*, (1998).

[43] Shun Lien Chaung, "Physics of Optoelectronic Devices", *Wiley Series in Pure and Applied Optics.*

[44] P. R. Thornton, "The Physics of Electroluminescent Devices", *E. & F. N. Spon. Ltd,* (1967).

[45] Walter T. Welford, "Useful Optics", *University of Chicago Press.*

[46] J. Tatum, D. Smith, J. Guenter and R. Johnson, "High speed characteristics of VCSELs", *Honeywell Micro switch Division.*

[47] Honeywell, "VCSEL Comparison to other Source Technology", (*http://content.honeywell.com/vcsel/advantage/comparison)*.

[48] B. Hawthorne, "Oxide Isolated VCSELs Reliability Summary", *Honeywell VCSEL Products, (http://content.honeywell.com/vcsel/pdf/oxidequal.pdf).*

[49] E. Hecht, Optics, 2nd Ed., *Addison Wesley Publishing Company*, (1987).

[50] George Hass, "Physics of Thin Films", *Academic Press*, (1963).

[51] T. E. Sale, "Vertical Cavity Surface Emitting Lasers", *Research Studies Press Ltd, John Wiley & Sons*, (1995).

[52] I. Vurgaftman, J. R. Meyer, L. R. Ram-Mohan, *J. Appl. Phys.*, **89**, 11, pp 5825, (2001).

[53] M. Yano, H. Nishi and M. Tagusagawa, *Jpn. J. Appl. Phys.*, **51**, pp 4022-28, (1980).

[54] G. H. B. Tompson and G. D. Henshall, *Elect. Lett.*, **16** pp42-44, (1980).

[55] T. Uji, K. Iwamoto and R. Lang, *Appl. Phys. Lett.*, **38**, pp 193-195, (1981).

[56] A. Sugimura, *IEEE J. Quant. Elect.*, **QE-17**, pp 627-635, (1981).

[57] A. R. Adams, M. Asada, Y. Suematsu, and S. Arai, *Jpn. J. Appl. Phys.*, **19**, 10, pp 621-624, (1980).

[58] Y. P. Varshni, *Physica*, **34**, pp. 149-154, (1967).

[59] G. W. Taylor, P. A. Evaldsson, *IEEE J. Quant. Elect*., **30** pp 1839 (1994).

[60] W. B. Joyce and R. W. Dixon, *Appl. Phys. Lett.*, **31**, pp 354, (1977).

[61] N. G. Nilsson, *Phys. Sta. Solidi (a),* **19**, K75, (1973).

62 L. G. Shantharama, A. R. Adams, C. N. Ahmad and R. J. Nicolas, *J. Phys. Solid State Phys.*, **17**, pp 4429-4442, (1984).

63 M. G. A. Bernard, G. Duraffourg, *Physica Status Solid*, **1**, pp 699, (1961).

64 G. Lasher and F. Stern, *Physical. Rev*. **133**, A553, (1964).

65 M. J. Adams and P. T. Landsberg, "Theory of the Injection Laser", *(Chapter from Galium Arsenide Lasers", edited by C. H. Gooch, Wiley – Interscience)*, pp 6-79.

66 F. Marinelli, *Solid State Elect.*, **8**, pp 939-942, (1965).

67 A. Haug, *Appl. Phys. B*, **44**, pp 151, (1987).

68 R. K. Willardson, H. L. Goering, "Compound Semiconductors Vol. I. Preparation of III-V" Compounds, *Reinhold Publishing Corporation.*

69 D. V. Morgan, K. Board, "An Introduction to Semiconductor Microtechnology", *John Wiley & Sons.*

70 I. Brodie, J. J. Murray, "The Physics of Microfabrication", *Plenum Press.*

71 P. K. Larsen and P. J. Dobson , "Reflection High-Energy Electron Diffraction and Reflection Electron Imaging of Surfaces", *Plenum, New York*, (1988).

72 H. M. Manasvit, *Appl. Phys. Lett.*, **12**, pp 136, (1968).

73 Z. L. Liau and D. E. Mull, *Appl. Phys. Lett.*, 56, **8**, pp 737-739, (1990).

74 R. J. Ram, J. J. Dudley and J. E. Bowers, *J. Appl. Phys.*, **78**, 6, pp 4227-4237, (1995).

75 H. Gebretsadik, K. Kamath, K. K. Linder, X. Zhang, and P. Bhattacharya, *Appl. Phys. Lett.*, **71**, 5, pp 581-583, (1997).

76 Y. Qian, Z.H. Zhu, Y.H. Lo, D. L. Huffaker, D. G. Deppe, H.Q. Hou, B.E. Hammons, W. Lin and Y.K. Tu, *Appl. Phys. Lett.*, **71**, 1, pp 25-27, (1997).

77 J. Koeth, R. Dietrich, and A. Forchel, *Appl. Phys. Lett.*, **72**, 13, pp 1638-1640, (1998).

78 University College London, microfabrication page.

79 A. J. Vickers, "Solid State Physics Lecture Notes", *University of Essex*, (1996).

80 W. Nakwaski, *Opt. & Quantum Electron*, **28** pp 335-352, (1996).

81 B. Tell, K. F. Brown-Goebeler, R. E. Leibenguth, F. M. Baez and Y. H. Lee, *Appl. Phys. Lett.*, **60**, pp 683, (1992).

82 J. P. Van Der Zeil, D. G. Deppe, N. Chand, G. J. Zydkzik and S. N. G. Chu, *IEEE J. Quant. Elect.*, **26** pp, 1873, (1990).

[83] J. W. Scott, S. W. Corzine, D. B. Young and L. A. Coldren, *Appl. Phys. Lett*., **62**, pp 1050, (1993).

[84] G. Hasnain, K. Tai, L. Yang *et al.*, *IEEE. J. Quant. Elect.* **27**, pp 1377 , (1991).

[85] B. Tell, K. F. Brown-Goebeler, R. E. Leibenguth, F. M. Baez, and Y. H. Lee, *Appl. Phys. Lett*., **60**, pp 683, (1992).

[86] D. B. Young, J. W. Scott, F. H. Peters *et al.*, *IEEE. J. Quant. Elect.*, **29**, pp 2013, (1993).

[87] J. P. Van der Ziel, D. G. Deppe, N. Chand, G. J. Zydzik and S. N. Chu, *IEEE J. Quant. Elect.,* **26**, pp 1873, (1990).

[88] R. S. Geel, B. J. Thibeault, S. W. Corzine, J. W. Scott and L. A. Coldren, *IEEE J. Quant. Elect.,* **26**, pp 2977, (1993).

[89] T. Wipiejewski, K. Panzlaff, E. Zeeb, and K. J. Ebeling, *IEEE Photon. Tech. Lett.*, **5**, pp 889, (1993).

[90] J. M. Catchmark, R. A. Morgan, K. Kojima *et al*., *Appl. Phys. Lett.*, **63**, pp 3122, (1993).

[91] P. M. Noriss, G. Chen, and C. L. Tien, *Inst. J. Heat Mass Transfer*, **37,** (Suppl. 1), pp 9, (1994).

[92] J. W. Bae, H. Temkin, C. Parsons *et al.*, *Appl. Phys. Lett*., **64**, pp 400, (1994).

[93] N. Balkan, A. Serpenguzel, A. O' Brien-Davies, I. Sokmen, C. J. Hepburn, R. Potter, M. J. Adams, J. S. Roberts, *Mat. Sci. and Eng.*, **B74,** pp96-100, (2000).

[94] A. Amiel, "Measurement and Modelling of the Reflectivity Spectrum of VCSEL Structures", *MSc Laser Comm. Course, Mini-Project Dissertation, University of Essex*, pp 16-17, (1999).

[95] J. Cheng, P. Zhou, S. Z. Sun, S. Hersee, D. R. Meyers, J. Zolper and G. A. Vawter, *IEEE J. Quant. Elect.*, **27**, pp 457-458, (1993).

[96] R. Sceats, N. Balkan, M. J. Adams and J. Masum, *Turkish J. of Phys.*, **23**, 4, pp 781-787, (1999).

[97] G. Hasnain, K. Tai, L. Yang, Y. H. Wang, R. J. Ficher, J. D. Wynn, B. Weir, N. K. Dutta, and A. Y. Cho, *IEEE J. Quant. Elect.*, **27**, 6, pp1377-1385, (1991).

[98] S. W. Koch, F. Janhnke and W. W. Chow, *Semicond. Sci. Technol.*, **10**, pp 739-751, (1995).

[99] J. W. Scott, R. S. Geel, S. W. Corzine, L. A. Coldren, *IEEE J. Quant. Elect.*, pp 1295-1307, (1993).

[100] J. Masum, N. Balkan and M. J. Adams, *Optics Comm*., **154**, pp43-46, (1998).

[101] R. Sceats, (Electroluminescence spectrum results for AT2339 VCSEL).

[102] H. C. Casey Jr. and M. B. Panish, "Heterostructure Lasers Part A: Fundamental Principles", *New York: Academic*, (1987).

[103] J. Piprek, Y. A. Akulova, D. I. Babic, L. A. Coldren, and J. E. Bowers, *Appl. Phys. Lett.*, **72,** pp 1814-1817, (1998).

104 C. J. Hepburn, R. Sceats, D. Ramoo *et al.,* (to be published).

105 J. Singh, "Semiconductor Optoelectronics Physics and Technology", *Mc Graw Hill*, (1995).

106 L. S. Heath, K. Meehan, A. K. Chin, P. Gavrilovic, J. H. Zarrabi, M. Wober and J. E. Bisberg, *Appl. Phys. Lett.*, **62**, 16, pp 1869-1871, (1993) .

107 R. Potter, S. Mazzucato, N. Balkan, M. J. Adams, P. R. Chalker, T. B. Joyce, T. J. Bullough, *Supperlattices and Microstructures*, **29**, 2, pp 169-186, (2001).

108 K. D. Choquette, J. F. Klem, A. J. Fischer, O. Blum, A. A. Allerman, I. J. Fritz, S. R. Kurtz, W. G. Breiland, R. Sieg, K. M. Geib, J. W. Scott and R. L. Naone, *Elect. Lett.*, **36**, 16, pp 1388-1390, (2000).

109 R. L. Naone, *et al.*, CLEO 2001.

110 G. B. Stringfellow, *J. Electrochem. Soc.*, **119**, pp 1780, (1972).

111 Y. Qiu, S. A. Nikishin, H. Temkin, V. A. Elyukhin, and Yu. A. Kudravtsev, *Appl. Phys. Lett.*, **70**, pp 1134, (1997).

112 J. Neugebauer and C. G. Van de Walle, *Phys. Rev. B*, **51**, pp 10568, (1995).

113 I. Ho, G.B. Stringfellow, *J. Cryst. Growth*, **178**, 1, (1997).

114 A. Ougazzaden, Y. Le Bellego, E. V. K. Rao, M. Juhel, L. Leprince, and G. Patriarche, *Appl. Phys. Lett.*, **70**, pp 2861, (1997).

115 M. Sopanen, H. P. Xin, and C. W. Tu, *Appl. Phys. Lett.*, **76**, 8, pp 994-996, (2000).

116 J. D. Thomas, H. D. Summers, P. M. Smowton, E. Herrmann, P. Blood and M. Hopkinson, "Temperature Insensitive Quantum Dot Structures for Vertical Cavity Lasers", (http://www.astro.cf.ac.uk/groups/optoelec/cleojdt1.pdf), *Optoelectronics Group, Cardiff University.*